UC Riverside
UC Riverside Electronic Theses and Dissertations

Title
Doping in Zinc Oxide Thin Films

Permalink
https://escholarship.org/uc/item/9sq5q4q3

Author
Yang, Zheng

Publication Date
2009

Peer reviewed|Thesis/dissertation

eScholarship.org Powered by the California Digital Library
University of California

UNIVERSITY OF CALIFORNIA
RIVERSIDE

# Doping in Zinc Oxide Thin Films

A Dissertation submitted in partial satisfaction
of the requirements for the degree of

Doctor of Philosophy

in

Electrical Engineering

by

Zheng Yang

June, 2009

Dissertation Committee:
Dr. Jianlin Liu, Chairperson
Dr. Alexander A. Balandin
Dr. Ward P. Beyermann

Copyright by
Zheng Yang
2009

The Dissertation of Zheng Yang is approved:

__________________________________________

__________________________________________

__________________________________________

Committee Chairperson

University of California, Riverside

**ACKNOWLEDGEMENT**

First of all, I appreciate my supervisor Prof. Jianlin Liu for the more-than-four-years' financial support and the lab facilities including two advanced molecular-beam epitaxy systems, without which I cannot complete my PhD study. Secondly, I'll say thanks to our collaborators: Prof. Ward Beyermann for the usage of PPMS, MPMS equipments, instructive instructions and helpful discussions; Prof. Jing Shi for the instructions on anomalous Hall effect and helpful discussions; Prof. David Look for the instructions on photoluminescence in ZnO and helpful discussions; Prof. Xiaoqing Pan for the electron microscopy studies.

I would also like to thank Prof. Alexander A. Balandin and Prof. Ward P. Beyermann for serving as my final dissertation defence committee members.

Finally, I want to thank my colleagues and labmates who gave me help during my PhD research and study: Mr. Zheng Zuo, Dr. Faxian Xiu, Dr. Leela Mandalapu, Dr. Yong Pu, Ms. Yan Li, Mr. Lin Li, Mr. Sheng Chu, Mr. Mario Olmedo, Ms. Jieying Kong, Dr. Dengtao Zhao, Dr. Yan Zhu, Ms. Bei Li, Mr. Ning Zhan, and Mr. Jingjian Ren.

*This thesis is dedicated to my wife Huimei Zhou.*

ABSTRACT OF THE DISSERTATION

Doping in Zinc Oxide Thin Films

by

Zheng Yang

Doctor of Philosophy, Graduate Program in Electrical Engineering
University of California, Riverside, June 2009
Dr. Jianlin Liu, Chairperson

Doping in zinc oxide (ZnO) thin films is discussed in this dissertation. The optimizations of undoped ZnO thin film growth using molecular-beam epitaxy (MBE) are discussed. The effect of the oxygen ECR plasma power on the growth rate, structural, electrical, and optical properties of the ZnO thin films were studied. It was found that larger ECR power leads to higher growth rate, better crystallinity, lower electron carrier concentration, larger resistivity, and smaller density of non-radiative luminescence centers in the ZnO thin films. Low-temperature photoluminescence (PL) measurements were carried out in undoped and Ga-doped ZnO thin films grown by molecular-beam epitaxy. As the carrier concentration increases from $1.8 \times 10^{18}$ to $1.8 \times 10^{20}$ $cm^{-3}$, the dominant PL line at 9 K changes from $I_1$ (3.368 - 3.371 eV), to $I_{DA}$ (3.317 – 3.321 eV), and finally to $I_8$ (3.359 eV). The dominance of $I_1$, due to *ionized*-donor bound excitons, is unexpected in n-type samples, but is shown to be consistent with the temperature-dependent Hall fitting results. We also show that $I_{DA}$ has characteristics of a donor-

acceptor-pair transition, and use a detailed, quantitative analysis to argue that it arises from $Ga_{Zn}$ donors paired with Zn-vacancy ($V_{Zn}$) acceptors. In this analysis, the $Ga_{Zn}^{0/+}$ energy is well-known from two-electron satellite transitions, and the $V_{Zn}^{0/-}$ energy is taken from a recent theoretical calculation. Typical behaviors of Sb-doped *p*-type ZnO are presented. The Sb doping mechanisms and preference in ZnO are discussed. Diluted magnetic semiconducting ZnO:Co thin films with above room-temperature $T_C$ were prepared. Transmission electron microscopy and x-ray diffraction studies indicate the ZnO:Co thin films are free of secondary phases. The magnetization of the ZnO:Co thin films shows a free electron carrier concentration dependence, which increases dramatically when the free electron carrier concentration exceeds ~$10^{19}$ $cm^{-3}$, indicating a carrier-mediated mechanism for ferromagnetism. The anomalous Hall effect was observed in the ZnO:Co thin films. The anomalous Hall coefficient and its dependence on longitudinal resistivity were analyzed. The presence of a side-jump contribution further supports an intrinsic origin for ferromagnetism in ZnO:Co thin films. These observations together with the magnetic anisotropy and magnetoresistance results, supports an intrinsic carrier-mediated mechanism for ferromagnetic exchange in ZnO:Co diluted magnetic semiconductor materials. Well-above room temperature and electron-concentration dependent ferromagnetism was observed in *n*-type ZnO:Mn films, indicating long-range ferromagnetic order. Magnetic anisotropy was also observed in these ZnO:Mn films, which is another indication for intrinsic ferromagnetism. The electron-mediated ferromagnetism in *n*-type ZnO:Mn contradicts the existing theory that the magnetic exchange in ZnO:Mn materials is mediated by holes. Microstructural studies using

transmission electron microscopy were performed on a ZnO:Mn diluted magnetic semiconductor thin film. The high-resolution imaging and electron diffraction reveal that the ZnO:Mn thin film has a high structual quality and is free of clustering/segregated phases. High-angle annular dark field imaging and x-ray diffraction patterns further support the absence of phase segregation in the film. Magnetotransport was studied on the ZnO:Mn samples, and from these measurements, the temperature dependence of the resistivity and magnetoresistance, electron carrier concentration, and anomalous Hall coefficient of the sample is discussed. The anomalous Hall coefficient depends on the resistivity, and from this relation, the presence of the quadratic dependence term supports the intrinsic spin-obit origin of the anomalous Hall effect in the ZnO:Mn thin film.

## TABLE OF CONTENTS

**ACKNOWLEDGEMENT** iv

**ABSTRACT** vi

**LIST OF FIGURES** xiii

**LIST OF TABLES** xviii

**1. Chapter 1 Introduction 1**

Reference 5

**2. Chapter 2 Optimizations of Undoped Zinc Oxide Growth 7**

2.1 Introduction 7

2.1.1 Different growth techniques in ZnO 7

2.1.2 Growth parameters of ZnO 7

2.2 Experiments 8

2.2.1 Growth procedures 8

2.2.2 Characterizations 9

2.3 Results and discussions 9

2.3.1 Growth rates 9

2.3.2 Structural properties 13

2.3.3 Electrical properties 15

2.3.4 Optical properties 19

2.4 Summary 20

2.5 Acknowledgement 21

Reference 22

**3. Chapter 3 Gallium Doping in Zinc Oxide 26**

3.1 Introduction 26

3.1.1 Current status of photoluminescence studies in ZnO 26

3.1.2 Background of Ga-doping in ZnO 27

3.2 Experiments 27
3.2.1 Sample preparation 28
3.2.2 Characterizations 31
3.3 Results and discussions 32
3.3.1 Structural Properties 32
3.3.2 Low temperature photoluminescence properties 33
3.3.3 Excitation power-dependent photoluminescence 41
3.3.4 Temperatue-dependent photoluminescence 41
3.4 Summary 46
3.5 Acknowledgement 47
Reference 48
**4. Chapter 4 Antimony Doping in Zinc Oxide 53**
4.1 Introduction 53
4.1.1 Background of *p*-type doping in ZnO 53
4.1.2 Review of *p*-type Sb-doping in ZnO and related devices 54
4.2 Experiments 56
4.2.1 Sample preparation 56
4.2.2 Characterizations 57
4.3 Results and discussions 58
4.3.1 Typical characterizations and properties of *p*-type ZnO:Sb 59
4.3.1.1 X-ray diffraction (XRD) 59
4.3.1.2 X-ray photoelectron spectroscopy (XPS) 62
4.3.1.3 Photoluminescence (PL) 64
4.3.1.4 Hall effect measurements 66
4.3.2 Sb doping mechanism and preference in ZnO thin films 67
4.3.2.1 Sb doping mechanism in ZnO 67
4.3.2.2 Sb doping preference in ZnO 69
4.4 Summary 75
4.5 Acknowledgement 76

Reference 77

**5. Chapter 5 Cobalt Doping in Zinc Oxide 79**

5.1 Introduction 79

5.1.1 Diluted magnetic semiconductors 79

5.1.2 ZnO diluted magnetic semiconductors 79

5.2 Experiments 81

5.2.1 Sample preparation 81

5.2.1.1 Epitaxial growth 81

5.2.1.2 Ion implantation 82

5.2.2 Characterizations 85

5.3 Results and discussions 86

5.3.1 Structural properties 86

5.3.2 Magnetic properties 89

5.3.3 Transport properties 94

5.4 Summary 101

5.5 Acknowledgement 102

Reference 103

**6. Chapter 6 Manganese Doping in Zinc Oxide 110**

6.1 Introduction 110

6.1.1 Co-doped ZnO *vs.* Mn-doped study 111

6.1.2 Current status of Mn-doped ZnO study 111

6.2 Experiments 112

6.2.1 Sample preparations 112

6.2.2 Characterizations 113

6.3 Results and discussions 114

6.3.1 Structural properties 114

6.3.2 Magnetic properties 123

6.3.3 Transport properties 128

6.4 Summary 138

6.5 Acknowledgement 139

Reference 140

**7. Chapter 7 Conclusions 145**

**LIST OF FIGURES**

Fig. 2.1. (a) Growth rate as a function of Zn cell temperature. $O_2$ flow rate and ECR power were kept at constants of 15 sccm and 76 W, respectively. (b) Growth rate as a function of the ECR plasma power. $O_2$ flowing rate and Zn cell temperature were kept at constants of 15 sccm and 400 °C, respectively. 11

Fig. 2.2. (a)-(f) RHEED patterns of samples A to F, respectively. Samples A to D were grown with the same $O_2$ flow rate and ECR power but different Zn cell temperature. Samples A and B are under oxygen rich condition while sample D is under zinc rich condition. Sample C was grown with stoichiometric condition, showing the streakiest pattern. Samples D to F were grown with the same Zn cell temperature and oxygen flow rate but different ECR power. Samples D to F show similar RHEED pattern, indicating no evident roughness variation of the films with increased plasma power. 13

Fig. 2.3. XRD spectra of samples D, E, and F. The insets show FWHM of the $(11\bar{2}0)$ ZnO peak, which decreases from 0.31° to 0.21° from sample D to F, indicating better crystallinity. 14

Fig. 2.4. (a) Electron carrier concentration as a function of Zn cell temperature with plasma power at constant. (b) Resistivity as a function of Zn cell temperature with plasma power at constant. Larger electron carrier concentration and lower resistivity were observed in thin film samples grown with higher Zn cell temperature, which was attributed to the larger density of Zn interstitials. 16

Fig. 2.5. (a) Electron carrier concentration as a function of plasma power with Zn cell temperature at constant. (b) Resistivity as a function of plasma power with Zn cell temperature at constant. Smaller electron carrier concentration and higher resistivity were observed in thin film samples grown with larger plasma power, which was attributed to the suppression of Zn interstitial formation with increased plasma power. 17

Fig. 2.6. Room-temperature PL emission spectra of samples D, E, and F around the NBE region. The FWHM of the ZnO NBE emission peaks decreases from 190 to 175 meV with increased plasma power from sample D to F. 19

FIG. 3.1. XRD patterns of (a) undoped ZnO sample A and (b) heavy-Ga-doped ZnO sample G. The insets show the RHEED patterns of samples A and G, which are streaky and spotty, respectively. 32

FIG. 3.2 PL spectra measured at 9 K for samples A to I [(a) to (i)]. 34

FIG. 3.3 Excitation power-dependent PL for samples D, E, and F [(a) to (c)] at 9 K. 40

FIG. 3.4 Temperature-dependent PL for samples D, E, and F [(a) to (c)]. 43

FIG. 3.5 (a) Temperature-dependent PL spectra of sample I. (b) Fit of the temperature dependence of the integrated PL intensity. 45

FIG. 4.1. Room temperature XRD patterns of (a) a typical *p*-type ZnO:Sb thin film sample A grown on Si (100) substrate and (b) a typical *p*-type ZnO:Sb thin film sample B grown on Si (111) substrate in $\theta$-$2\theta$ geometry. Grazing incidence XRD patterns of (c) ZnO:Sb sample A and (d) ZnO:Sb sample B. 60

FIG. 4.2 Room temperature XPS spectra for the (a) ZnO:Sb sample A, (b) ZnO:Sb sample B, and (c) undoped ZnO thin film sample U. The inset in (c) shows the XPS spectra of sample U in a wider scanning range. 62

FIG. 4.3 PL spectra of (a) ZnO:Sb sample A and (b) ZnO:Sb sample B at various temperatures ranging from 8.5 to 300 K. 64

FIG. 4.4 (a) Temperature dependence of the hole concentration of ZnO:Sb sample A. The inset shows the Hall resistance as a function of applied magnetic field at T = 300 K. (b) Temperature dependence of the Hall mobility of ZnO:Sb sample A. The inset shows the temperature dependence of electrical resistivity. 66

FIG. 4.5 Calculated Sb- and O-related defect formation energy in ZnO under O-rich condition. The slope of the curves reflects the charge state of the defects and the solid dots denote the energy positions at which transition from one charge state to another takes place. 67

FIG. 4.6 SEM images of (a) ZnO:Sb thin film sample C grown on Si (100) substrate and (b) ZnO:Sb thin film sample D grown on Si (111). 69

FIG. 4.7 SEM images of (a) ZnO:Sb thin film sample E grown on $SiO_2$ substrate, (b) ZnO:Sb thin film sample F grown on *r*-plane sapphire substrate, and (c) ZnO:Sb thin film sample G grown on *c*-plane sapphire substrate. 70

FIG. 4.8 Time-evolution of the carrier type and concentrations in ZnO:Sb sample G. 72

FIG. 5.1 SIMS spectra for (a) the as-grown ZnO thin film, (b) the ZnO:Co thin film after Co ion implantation, but before annealing, and (c) the ZnO:Co thin film after annealing at 900 ˚C for 5 minutes (sample A). The magnetic measurements were all performed on the annealed samples. 83

FIG. 5.2 (a) Cross-sectional TEM image of a ZnO:Co thin film on a sapphire substrate (sample A). SAED patterns of (b) ZnO:Co thin film and (c) sapphire substrate, taken from the areas indicated by the dotted circles. 86

FIG. 5.3. (a) Cross-sectional HRTEM image of the interface between the ZnO:Co thin film and the sapphire substrate in sample A, showing an atomically sharp interface. (b) HRTEM image of the ZnO:Co thin film (sample A). The film has high crystallinity with no observable secondary phase. 87

FIG. 5.4. XRD spectra of (a) ZnO and (b) ZnO:Co thin films (sample A). Both the ZnO and ZnO:Co thin films show high crystallinity with no impurity phases within the detection limit of the system. 88

FIG. 5.5. (a) The magnetic field dependence of the magnetization for a ZnO:Co thin film (sample A) measured at 300 K and 10 K (inset). (b) The temperature dependence of the saturated magnetization, from 2 to 800 K measured with an applied field of 0.2 T. A high-temperature extrapolation of the data indicates that the Curie temperature is around 950 K. The inst shows the field dependence of the magnetization of this sample measured at 700K. 90

FIG. 5.6. (a) The magnetic field dependence of the magnetization for ZnO:Co thin film samples B, C, and D measured at a temperature of 300 K. (b) The dependence of the saturated magnetization $M_S$ on electron carrier concentration $n$ in ZnO:Co thin film samples. A polynomial fitting to the data is indicated with the dashed line. 92

FIG. 5.7. Magnetic anisotropy of a ZnO:Co thin film (sample E) measured at a temperature of 300 K. The in-plane field dependence of the magnetization (solid circles) are stronger than out-of-plane magnetization (open circles). 94

FIG. 5.8. (a) Transverse magnetoresistance, MR=[R(H)-R(0)]/R(0), of a ZnO:Co thin film (sample E) measured at different temperatures from 2 to 300 K. The applied magnetic field was perpendicular to the plane of the film. (b)-(e) The temperature dependence of the magnetoresistance at different magnetic fields of 8, 5, 2, and 1 T. 95

FIG. 5.9. (a) The Hall resistance as a function of the applied magnetic field for a ZnO:Co thin film (sample E) measured at a temperature of 50 K. The inset shows the AHE data over an expended field range near the origin after the linear OHE contribution was subtracted. (b)-(c) The Hall resistance as a function of the applied magnetic field for the same ZnO:Co thin film sample measured at the temperatures of 10 K and 300 K. 97

FIG. 5.10. Temperature-dependence of the resistivity of a ZnO:Co thin film (sample E). 99

FIG. 5.11. The ratio of the anomalous Hall resistivity $\rho_{AHE}$ to the resistivity $\rho_{xx}$ as a function of the resistivity $\rho_{xx}$. 101

FIG. 6.1 XRD spectra of (a) sample A before Mn implantation and (b) sample A after Mn implantation. The ZnO thin films show good crystallinity both before and after Mn implantation. 115

FIG. 6.2 SIMS spectra of (a) sample A before Mn implantation, (b) sample A after Mn implantation, and (c) Mn-implanted sample A after annealing. The Zn and Ga concentrations are nearly uniform in the ZnO thin film before implantation. After implantation, Mn ions have a Gaussian distribution with the peak near the surface as seen in unannealed Mn-implanted ZnO sample. After annealing, the Mn ions redistribute to a relatively uniform profile throughout the depth of the film. A small percentage of the Mn ions penetrate the ZnO film reaching the sapphire substrates in both unannealed and annealed ZnO:Mn samples. The density of the residual Mn concentration in the substrate is more than one order of magnitude smaller than in the ZnO film layer. 115

FIG. 6.3. (a) Cross-sectional TEM image of a ZnO:Mn thin film on a sapphire substrate. (b) A typical SAED pattern from the ZnO:Mn thin film, and (c) SAED pattern from the sapphire substrate. 117

FIG. 6.4. (a) Cross-sectional HRTEM image of the interface between the ZnO:Mn thin film and the sapphire substrate, showing an atomically sharp interface. (b) HRTEM image of the ZnO:Mn thin film. The film appears to be highly crystalline with no secondary phase. 118

FIG. 6.5. (a)-(b) Two HRTEM images taken from different places on the ZnO:Mn thin film. (c)-(f) The fast Fourier transform patterns corresponding to the square region marked with dotted lines in (a) and (b). 119

FIG. 6.6. (a)-(b) Two HAADF images of the ZnO:Mn thin film. 120

FIG. 6.7. (a) EDS spectrum of the ZnO:Mn thin film, showing Zn and Mn signals. The inset shows the electron microscopy image of the region where the EDS was taken. (b) XRD pattern of the ZnO:Mn thin film. The orientation of the ZnO:Mn thin film is along the $[11\bar{2}0]$ direction. The inset shows that the full-width at half-maximum of the $(11\bar{2}0)$ peak located at 56.7° is ~0.29°. 122

FIG. 6.8 Magnetic field dependence of the magnetization for the Mn-implanted ZnO sample A measured at 300 K. The ferromagnetic hysteresis loop is clearly observed. The upper inset shows the magnetic field dependence of the magnetization on the same sample at 10 K. The bottom inset shows the temperature dependence of the magnetization

measured from 2 to 300 K, indicating that the Curie temperature of this sample is well above 300 K. 124

FIG. 6.9 (a) Magnetic field dependence of the magnetization for the Mn-implanted ZnO samples B, C, and D measured at 300 K. (b) The relation between the saturated magnetization $M_S$ and the electron carrier concentration ($n$). The $M_S$ of the samples show an electron concentration dependent behavior. 126

FIG. 6.10 Anisotropic magnetism for a ZnO:Mn thin film (sample B). The magnetic field dependence of the magnetizations for the out-of-plane (magnetic field perpendicular to the film) and in-plane (magnetic field parallel to the film) geometries are shown with the open and solid circles, respectively. The out-of-plane magnetization shows a smaller saturated magnetization but larger coercivity than in-plane magnetization. The inset shows the *M-H* curve measured over a larger magnetic field range of up to 12000 Oe. 127

FIG. 6.11. (a) Magnetoresistance (MR) of the ZnO:Mn thin film at different temperatures. (b)-(d) The temperature dependence of the MR from the ZnO:Mn thin film with applied magnetic field of 10 T, 6 T, and 2 T. The vertical distance between the two thin lines in every circle symbol represents the error bar for that data point. The magnetic field is perpendicular to the film plane for these measurements. 129

FIG. 6.12. (a) The field dependence of the Hall resistance $R_{\mathrm{Hall}}$ measured at 5K. The lower inset shows the AHE after subtracting the linear background from the OHE. The upper inset shows the method employed to determine $R_0$ an $R_S$. (b)-(e) The field-dependence of the Hall resistance measured at 10 K, 50 K, 100 K, and 300 K on the same ZnO:Mn thin film sample. 131

FIG. 6.13. (a) The temperature dependence of ordinary Hall coefficient $R_0$. The inset shows the temperature dependence of the electron carrier concentration $n$ derived from $R_0$. The vertical distance between the two thin lines in every symbols represents the error bar of the data point. (b) The temperature dependence of anomalous Hall coefficient $R_S$. 135

FIG. 6.14. The temperature dependence of the resistivity $\rho_x$ from 2 K to 350 K. The inset shows the same data with reciprocal temperature along the horizontal axis. 136

FIG. 6.15. The relation between $R_s/\rho_x$ and $\rho_x$. The solid square symbols with error bars are the experimental data. The dashed line shows a linear fit to the data, representing the linear and quadratic dependences of $\rho_x$ on $R_s$. 137

**LIST OF TABLES**

Table 2.1 Growth parameters and growth rates of the ZnO thin films. 10

Table 2.2 Hall effect measurements data of the ZnO thin films. 18

Table 2.3 Full-width at half-maximum (FWHM) of the ZnO ($11\bar{2}0$) XRD and near band edge emission (NBE) PL peaks from the ZnO thin film sample D, E, and F at room temperature. 20

Table 3.1 Growth parameters of the undoped and Ga-doped ZnO thin films. 29

Table 3.2 The electron carrier concentrations of undoped and Ga-doped ZnO thin films at 300 K and 10 K. 30

Table 4.1 The carrier type and concentration of ZnO:Sb samples grown on different substrates. 68

Table 5.1 Electron carrier concentration before and after implantation and the saturated magnetization of ZnO:Co thin film samples. The data were taken at room temperature. 82

Table 5.2 The resistivity $\rho_{xx}$, ordinary Hall coefficient $R_0$, anomalous Hall coefficient $R_S$, electron carrier concentration $n$, and the ratio $\rho_{AHE}/\rho_{xx}$ for ZnO:Co thin film sample E. Data were measured at the temperatures of 10 K, 50 K, and 300 K. 91

Table 6.1 Electron carrier concentrations and the saturated magnetization for four different samples of ZnO thin films after Mn implantation. 125

Table 6.2 Ordinary Hall coefficient $R_0$, anomalous Hall coefficient $R_S$, electron carrier concentration $n$, and resistivity $\rho_x$ at different temperatures. 133

# 1. Chapter 1 Introduction

ZnO materials have attracted a great deal of attention due to their potential applications in optoelectronics and spintronics.[1-4] ZnO has a large exciton binding energy of ~60 meV,[5] which make it superior for applications in light-emitting-diodes (LED) and laser diodes (LD). ZnO has also been both theoretically predicted[6-7] and experimentally proved[8-10] to be a high Curie temperature ($T_C$) diluted magnetic semiconducting (DMS) materials when doped with transition metals. All these fantastic properties of ZnO need to be achieved and demonstrated by *doping*, a kind of technique to "magically manipulate" the behavior of ZnO by adding a small amount of dopant atoms into ZnO. For example, when you want to fabricate a ZnO LED, you need both *n*-type ZnO and *p*-type ZnO to form a *pn* junction. In a complicated LD structure, we need barrier layers to confine the carriers in the active layer. In ZnO, we need Mg or Be to expand its bandgap to be suitable barrier layers. ZnO has a bandgap of 3.37 eV at room-temperature, which corresponds to the near ultra-violet (UV) region. Once we need to extend this near UV application to visible region from ZnO, we also need to do bandgap engineering. Cd is a candidate to shrink the bandgap of ZnO. More straightforwardly, if we need a ZnO DMS material, we have to dope ZnO with metals, generally they are transition metals. *The main and core topic of this dissertation is doping in ZnO thin films.*

In chapter 2 of this dissertation, the optimizations of undoped ZnO thin film

growth using molecular-beam epitaxy (MBE) were discussed. Undoped ZnO is the basis for doping, which is also very important. Besides the general MBE growth parameters such as Zn cell temperature, $O_2$ flowing rate, and substrate temperature, plasma power is also critical for MBE ZnO growth. How the general growth parameters affect the ZnO properties have been widely reported, however, no experimental studies have been reported on the ECR Plasma. In this chapter, the effect of ECR plasma power on the optimization of ZnO growth, such as growth rate, structural, electrical, and optical properties of the ZnO thin films is reported.[11]

In chapter 3 of this dissertation, *n*-type doping in ZnO through Ga is discussed. Although *p*-type doping has attracted more recent attention in ZnO research, *n*-type materials with high crystallinity and controllable electron carrier concentration (*n*) are also indispensable for optoelectronic and spintronic applications. For example, controllable *n* is important for ZnO-based dilute magnetic semiconductor materials, because their magnetic properties can be modulated by *n*.[7-9] Also, group-III-doped ZnO with large *n* is a potential candidate for replacing conventional transparent conducting oxides such as indium tin oxide. Furthermore, in ZnO LEDs and LDs, besides the *p*-ZnO layer, *n*-ZnO layer is also indispensible.[12]

In chapter 4 of this dissertation, *p*-type doping in ZnO through Sb is discussed. Both the materials studies and the device fabrications based on Sb *p*-doping in ZnO have

made extensive progress in the past several years, since the theoretical prediction[13] of Sb could be a *p*-dopant for ZnO by forming a complex acceptor as $Sb_{Zn}$-$2V_{Zn}$ (160 meV above $E_V$). Successful *p*-type ZnO:Sb materials[14-15], hetero-[16] and homo-pn-junctions[17], LEDs[18-20], and LD[21] have been achieved. In this chapter, the typical behaviors of Sb-doped *p*-type ZnO are presented. The Sb doping mechanisms and preference in ZnO are discussed.

In chapter 5 of this dissertation, ZnO DMS through Co magnetically doping is discussed. In this chapter, ZnO:Co DMS thin films with above room-temperature $T_C$ are presented. The structural, magnetic, and electrical transport properties of ZnO:Co thin films were comprehensively characterized. Intrinsic ferromagnetism is confirmed by TEM, XRD, carrier concentration dependent magnetization, magnetic anisotropy, magnetoresistance, and anomalous Hall effect. *This is also the first time that carrier concentration dependent magnetic properties have ever been demonstrated in ZnO DMS materials.*

In chapter 6 of this dissertation, ZnO DMS through Mn magnetically doping is discussed. Previously, it was predicted by theory that the ZnO:Co DMS would be ferromagnetic in *n*-type environment, but ZnO:Mn DMS can only be ferromagnetic in *p*-type environment.[7] However, we not only observed ferromagnetism in *n*-type ZnO:Mn DMS, but also observed electron carrier concentration dependent magnetization in these

*n*-type ZnO:Mn DMS thin films. Motivated by our work together with recent work reporting ferromagnetism in *n*-type ZnO:Mn from several other groups, theorists start re-evaluating their models and calculations. Some new theories are being proposed. In this chapter, ZnO:Mn DMS thin films with above room-temperature $T_C$ were presented. The structural, magnetic, and electrical transport properties of ZnO:Mn thin films were comprehensively characterized. Intrinsic ferromagnetism is confirmed by TEM, XRD, carrier concentration dependent magnetization, magnetic anisotropy, magnetoresistance, and anomalous Hall effect.

Finally, a separate conclusion part is presented in chapter 7, the last chapter of this dissertation.

## References

[1] D. C. Look, Mater. Sci. Eng. B **80**, 383 (2001).

[2] S. J. Pearton, D. P. Norton, K. Ip, Y. W. Heo, and T. Steiner, Superlattices Microstruct. **34**, 3 (2003).

[3] Ü. Özgür, Ya. I. Alivov, C. Liu, A. Teke, M. A. Reshchikov, S. Doğan, V. Avrutin, S.-J. Cho, and H. Morkoç, J. Appl. Phys. **98**, 041301 (2005).

[4] C. Klingshirn, Phys. Stat. Sol. (b) **244**, 3027 (2007).

[5] D. G. Thomas, J. Phys. Chem. Solids **15**, 86 (1960).

[6] T. Dietl, H. Ohno, F. Matsukura, J. Cibert, D. Ferrand, Science **287**, 1019 (2000).

[7] K. Sato and H. Katayama-Yoshida, Semicond. Sci. and Technol. **17**, 367 (2002).

[8] Z. Yang, J. L. Liu, M. Biasini, and W. P. Beyermann, Appl. Phys. Lett. **92**, 042111 (2008).

[9] Z. Yang, M. Biasini, W. P. Beyermann, M. B. Katz, O. K. Ezekoye, X. Q. Pan, Y. Pu, J. Shi, Z. Zuo, and J. L. Liu, J. Appl. Phys. 104, 113712 (2008).

[10] Z. Yang, W. P. Beyermann, M. B. Katz, O. K. Ezekoye, Z. Zuo, Y. Pu, J. Shi, X. Q. Pan, and J. L. Liu, J. Appl. Phys., 105 (2009).

[11] Z. Yang, J. -H. Lim, S. Chu, Z. Zuo, and J. L. Liu, Appl. Surf. Sci. **255**, 3375 (2008).

[12] Z. Yang, D. C. Look, J. L. Liu, Appl. Phys. Lett. **94**, 072101 (2009).

[13] S. Limpijumnong, S. B. Zhang, S. H. Wei, C. H. Park, Phys. Rev. Lett. **92**, 155504

(2004).

[14] F. X. Xiu, Z. Yang, L. J. Mandalapu, D. T. Zhao, J. L. Liu, and W. P. Beyermann, Appl. Phys. Lett. **87**, 152101 (2005).

[15] F. X. Xiu, Z. Yang, L. J. Mandalapu, D. T. Zhao, and J. L. Liu, Appl. Phys. Lett. **87**, 252102 (2005); Y. J. Zeng and Z. Z. Ye, Appl. Phys. Lett. **90**, 116102 (2007); and F. X. Xiu and J. L. Liu, Appl. Phys. Lett. **90**, 116103 (2007).

[16] L. J. Mandalapu, F. X. Xiu, Z. Yang, D. T. Zhao, and J. L. Liu, Appl. Phys. Lett. **88**, 112108 (2006); Y. J. Lin, P. H. Wu, and D. S. Liu, Appl. Phys. Lett. **91**, 136101 (2007); and L. J. Mandalapu and J. L. Liu, Appl. Phys. Lett. **91**, 136102 (2007).

[17] L. J. Mandalapu, Z. Yang, F. X. Xiu, D. T. Zhao, and J. L. Liu, Appl. Phys. Lett. **88**, 092103 (2006).

[18] L. J. Mandalapu, Z. Yang, S. Chu, and J. L. Liu, Appl. Phys. Lett. **92**, 122101 (2008).

[19] S. Chu, J. H. Lim, L. J. Mandalapu, Z. Yang, L. Li, and J. L. Liu, Appl. Phys. Lett. **92**,152103 (2008).

[20] J. Kong, S. Chu, M. Olmedo, L. Li, Z. Yang, and J. L. Liu, Appl. Phys. Lett. **93**, 132113 (2008).

[21] S. Chu, M. Olmedo, Z. Yang, J. Kong, J. L. Liu, Appl. Phys. Lett. **93**, 181106 (2008).

# 2. Chapter 2 Optimizations of Undoped Zinc Oxide Growth

## 2.1 Introduction

Recently, Zinc Oxide (ZnO) has been widely studied for its attractive applications in ultraviolet light-emitting diodes and laser diodes, because it has a direct bandgap of 3.37 eV at room temperature and a large exciton binding energy of 60 meV.[1-3]

### 2.1.1 Different growth techniques of ZnO

Various techniques have been employed to grow ZnO,[3] such as hydrothermal method,[4-5] magnetron sputtering,[6-7] pulse laser deposition,[8-10] metal-organic chemical vapor deposition,[11-14] and molecular-beam epitaxy (MBE).[15-37] Among these growth methods, MBE has some potential advantages, such as precise control of growth parameters and *in situ* characterization techniques. Although some other oxidants such as $NO_2$,[35] $O_3$,[36] and $H_2O_2$[37] were tried, $O_2$ plasma assisted method is the mainstream for ZnO MBE growth. Radio frequency (RF) and electron cyclotron resonance (ECR) are the two main plasma generation approaches. Generally ECR plasma[28-34] can sustain much larger $O_2$ flowing rate than RF plasma[20-27] during ZnO growth. So oxygen rich condition is easier to be achieved by ECR plasma-assisted MBE, which is very critical for *p*-type ZnO because of the suppression of zinc interstitials and oxygen vacancies.[31-32]

### 2.1.2 Growth parameters of ZnO

Besides the general MBE growth parameters such as Zn cell temperature, $O_2$ flowing rate, and substrate temperature, ECR plasma power is also critical for MBE ZnO growth. How the general growth parameters affect the ZnO properties have been widely reported, however, no experimental studies have been reported on the ECR Plasma. In this chapter, the effect of ECR plasma power on the optimization of ZnO growth, such as growth rate, structural, electrical, and optical properties of the ZnO thin films is reported.

## 2.2 Experiments

### 2.2.1 Growth Procedures

ZnO thin films were grown on *r*-plane sapphire substrates using ECR plasma-assisted MBE. A radical effusion cell filled with elemental Zn (6N) metals was used as Zn source. Zn flux is controlled by the effusion cell temperature. An ECR plasma tube supplied with $O_2$ (5N) gas was used as the oxygen source. Oxygen flow rate can be precisely tuned by a mass flow controller. The color of the oxygen plasma looks yellowish-white and white at small (e.g. 76 W) and large (e.g. 228 W) ECR power, respectively. The sapphire substrates were cleaned by the following procedures before growth. Firstly, the substrate was chemically cleaned in the hot (~150 ºC) aqua regia ($HNO_3$: HCl = 1: 3) solutions for 20 minutes; rinsed by de-ionized water; dried by nitrogen gun; and transferred into the MBE chamber. Subsequently, the substrate was

thermally cleaned by annealing it at 800 ºC under vacuum in MBE chamber for 10 minutes. Finally, 10 minutes oxygen plasma exposure treatment was performed and the ZnO growth was immediately followed. The substrate temperature was kept at ~550 ºC. Different growth conditions were employed by tuning the Zn cell temperature, $O_2$ flow rate, and ECR plasma power.

### 2.2.2 Characterizations

*In situ* reflection high-energy electron diffraction (RHEED) measurements were performed on the as grown samples. X-ray diffraction (XRD) measurements were performed using a Bruker D8 Advance x-ray diffractometer. Hall effect measurements were carried out using an Ecopia HMS-3000 Hall effect measurement system at room-temperature. Photoluminescence (PL) study was carried out using a home-built PL system at room temperature. A 325-nm-wavelength He-Cd laser was used as excitation source and a photomultiplier tube was used to detect the PL signals.

## 2.3 Results and discussions

### 2.3.1 Growth rates

Table 2.1 shows the growth parameters and growth rates of the ZnO thin films. Samples A to D were grown with the same $O_2$ flow rate of 15 sccm and ECR plasma

power of 76 W, but with different Zn effusion cell temperatures ranging from 360 to 400 °C. Samples D to F were grown with the same Zn effusion cell temperature at 400 °C and $O_2$ flow rate of 15 sccm, but with different ECR plasma powers, ranging from 76 to 228 W. Sample G was grown for comparison to sample B, which only differs in the oxygen flowing rate.

Table 2.1 Growth parameters and growth rates of the ZnO thin films.

| Sample | Zn cell temperature (°C) | $O_2$ flow rate (sccm) | ECR current (mA) | ECR power (W) | Growth rate (nm/min) |
|---|---|---|---|---|---|
| A | 360 | 15 | 20 | 76 | 0.38 |
| B | 380 | 15 | 20 | 76 | 0.94 |
| C | 390 | 15 | 20 | 76 | 1.11 |
| D | 400 | 15 | 20 | 76 | 1.11 |
| E | 400 | 15 | 40 | 152 | 1.78 |
| F | 400 | 15 | 60 | 228 | 2.07 |
| G | 380 | 20 | 20 | 76 | 0.87 |

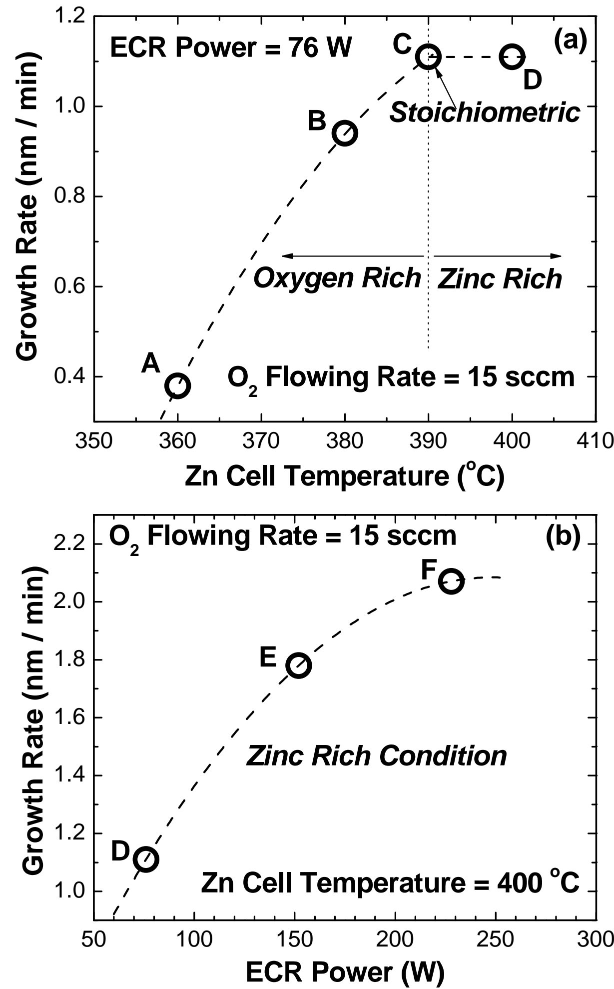


Fig. 2.1. (a) Growth rate as a function of Zn cell temperature. $O_2$ flow rate and ECR power were kept at constants of 15 sccm and 76 W, respectively. (b) Growth rate as a function of the ECR plasma power. $O_2$ flowing rate and Zn cell temperature were kept at constants of 15 sccm and 400 °C, respectively.

Figure 2.1(a) shows the relation between the ZnO thin film growth rate and the Zn effusion cell temperature within samples A to D. The growth rate increases from 0.38 nm/minute in sample A to 1.11 nm/minute in sample C with the increase of the Zn cell

temperature from 360 to 390 °C. However, further increase of the Zn cell temperature from 390 to 400 °C leads to the saturation of the growth rate, which means zinc rich condition has been reached. It is concluded that sample C was grown approximately under stoichiometric condition and oxygen rich condition is reached within the regime of Zn cell temperature between 360 and 390 °C. In the oxygen rich condition region, further increase of $O_2$ flow rate while maintaining the same Zn cell temperature (for example, 15 sccm for sample B vs. 20 sccm for sample G) leads to slightly smaller growth rate (0.87 nm/min for sample G and 0.94 nm/min for sample B). This is attributed to the larger scattering rate from increased gas flow. Figure 2.1(b) shows the relation between the growth rate and the ECR plasma power within sample D to F. The growth rate increases from 1.11 nm/minute in sample D to 2.07 nm/minute in sample F with the increase of the ECR power from 76 to 228 W, indicating that ECR power plays an important role for ZnO thin film growth rate. The increase of the growth rate at the increased plasma power is attributed to the increased atomic oxygen density, because the Zn atoms react with the atomic oxygen instead of molecular oxygen during the ZnO growth. Similar experimental results were also reported in the ECR plasma-assisted MBE nitride growth that larger plasma power leads to increased density of the atomic nitrogen.[38]

### 2.3.2 Structural Properties

Figure 2.2 shows the RHEED patterns of samples A to F. From A to C, the RHEED patterns become more and more streaky, indicating that the surface is smoother. Also, sample C shows a streakier pattern than sample D. No evident RHEED pattern difference was observed among samples D, E, and F, but differences were observed in the XRD spectra.

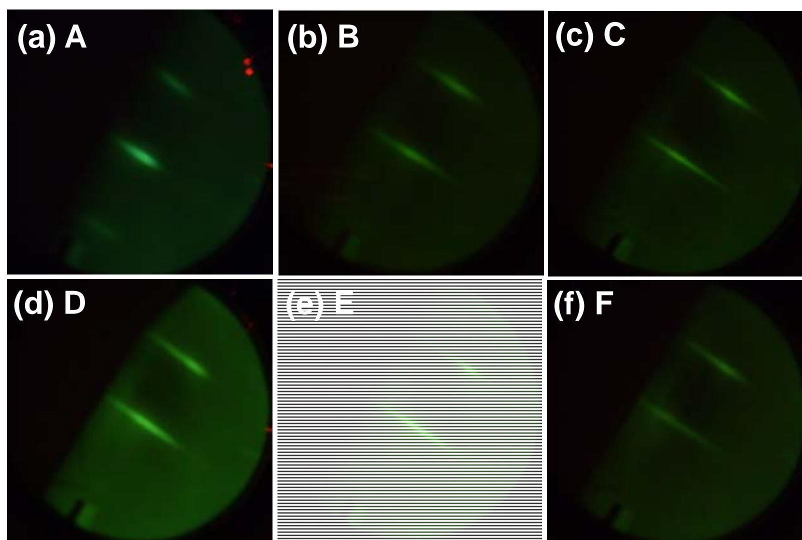


Fig. 2.2. (a)-(f) RHEED patterns of samples A to F, respectively. Samples A to D were grown with the same $O_2$ flow rate and ECR power but different Zn cell temperature. Samples A and B are under oxygen rich condition while sample D is under zinc rich condition. Sample C was grown with stoichiometric condition, showing the streakiest pattern. Samples D to F were grown with the same Zn cell temperature and oxygen flow rate but different ECR power. Samples D to F show similar RHEED pattern, indicating no evident roughness variation of the films with increased plasma power.

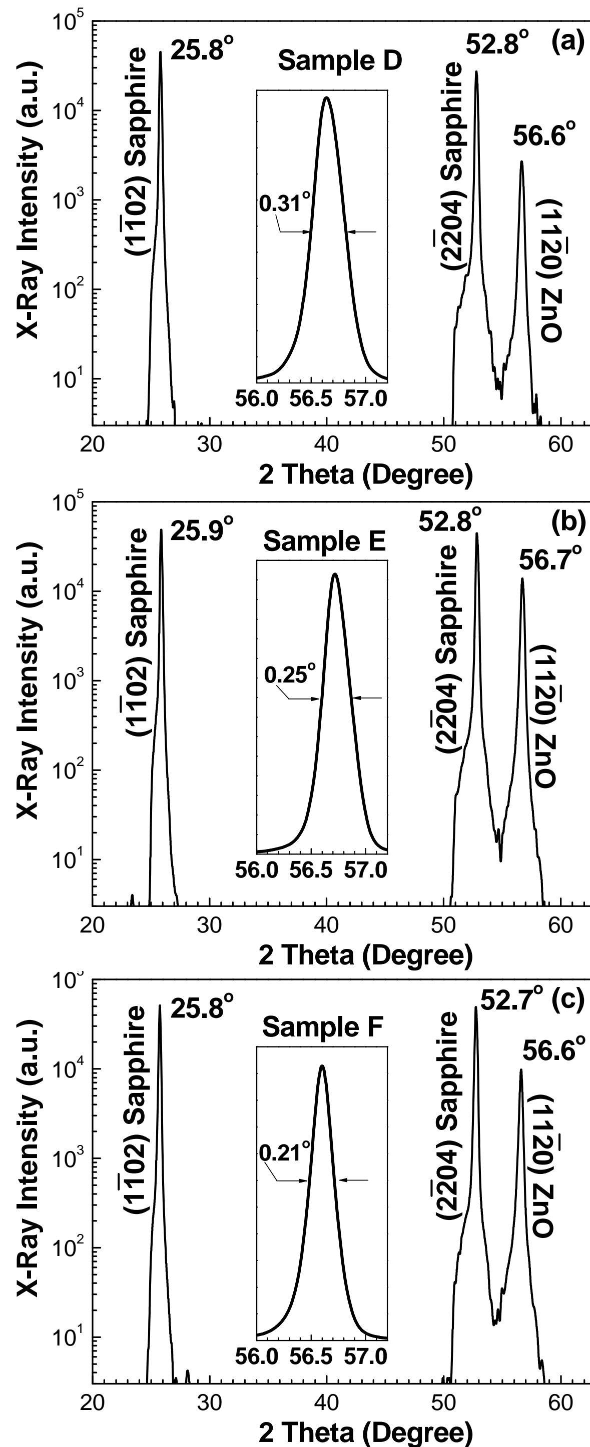


Fig. 2.3. XRD spectra of samples D, E, and F. The insets show FWHM of the $(11\bar{2}0)$ ZnO peak, which decreases from 0.31˚ to 0.21˚ from sample D to F, indicating better crystallinity.

Figure 2.3 shows the XRD spectra of samples D, E, and F. The peaks at 25.8° and 52.8° originate from the $(1\bar{1}02)$ and $(2\bar{2}04)$ planes of *r*-cut sapphire substrates. The peaks located at around 56.7° are from ZnO $(11\bar{2}0)$ plane. The insets show the full width at half maximum (FWHM) of the $(11\bar{2}0)$ ZnO peak, which decreases from 0.31° in sample D to 0.21° in sample F, indicating that larger ECR plasma power leads to better ZnO crystallinity. This is attributed to the decreased ionic oxygen (increased atomic oxygen) density from enhanced plasma power.[38-39] Ionic particles generally degrade thin film quality during the epitaxial growth. The FWHM values are also summarized in Table 2.3.

### 2.3.3 Electrical Properties

Figures 2.4 (a) and (b) show the relations between the electron carrier concentration and resistivity and the Zn cell temperature, respectively. The plasma power was fixed for all samples. Larger electron carrier concentration and lower resistivity were observed in thin film samples grown with higher Zn cell temperature, which was attributed to the larger density of Zn interstitials.

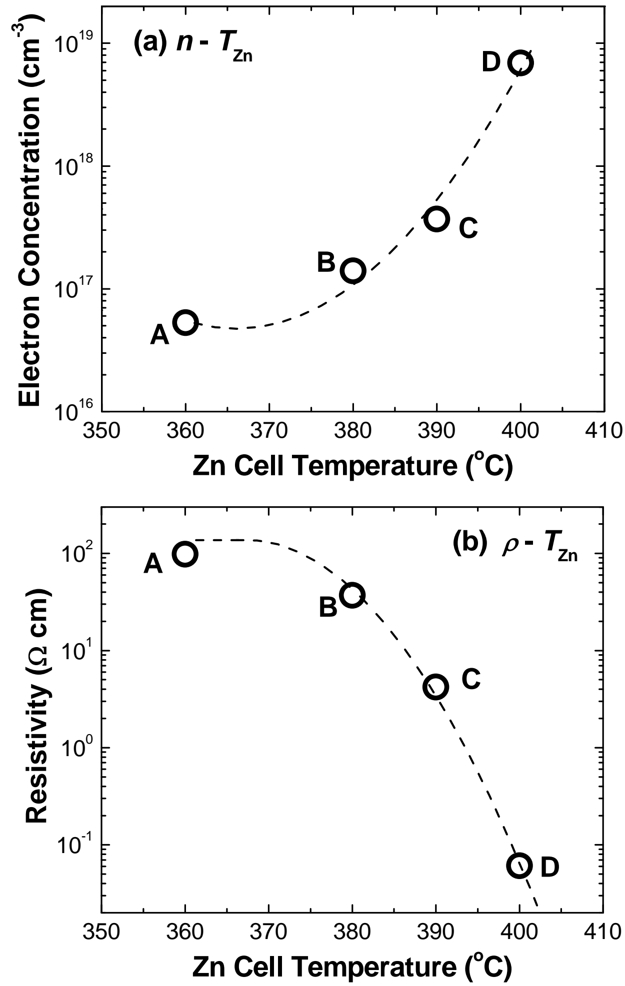


Fig. 2.4. (a) Electron carrier concentration as a function of Zn cell temperature with plasma power at constant. (b) Resistivity as a function of Zn cell temperature with plasma power at constant. Larger electron carrier concentration and lower resistivity were observed in thin film samples grown with higher Zn cell temperature, which was attributed to the larger density of Zn interstitials.

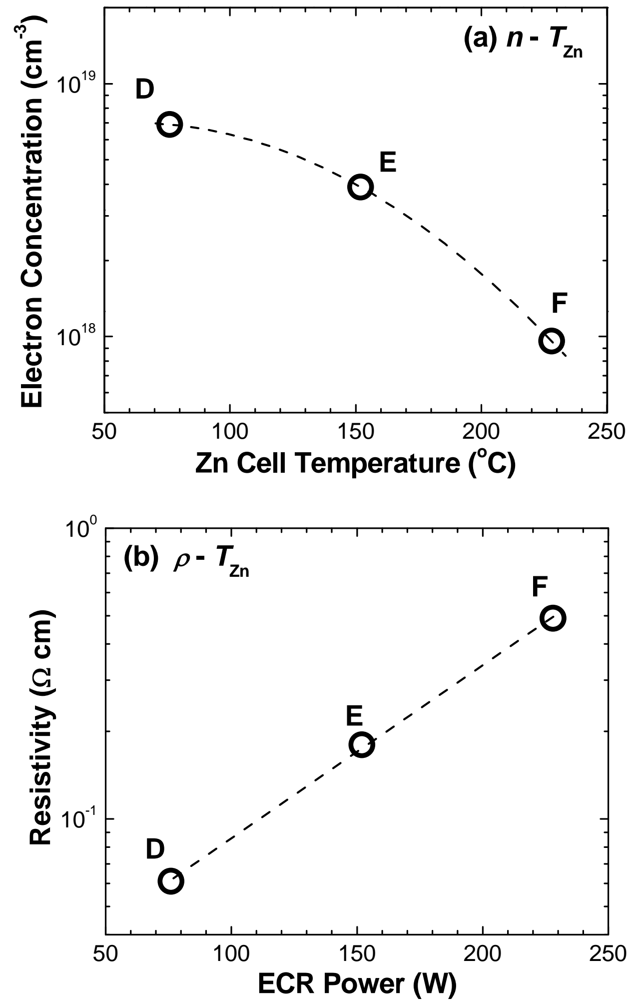


Fig. 2.5. (a) Electron carrier concentration as a function of plasma power with Zn cell temperature at constant. (b) Resistivity as a function of plasma power with Zn cell temperature at constant. Smaller electron carrier concentration and higher resistivity were observed in thin film samples grown with larger plasma power, which was attributed to the suppression of Zn interstitial formation with increased plasma power.

Figures 2.5 (a) and (b) show the relations between the electron carrier

concentration and resistivity and the ECR oxygen plasma power, respectively, with the Zn cell temperature at constant. Smaller electron carrier concentration and higher resistivity were observed in thin film samples grown with larger plasma power, which was attributed to the suppression of Zn interstitial formation with increased plasma power. When the ECR oxygen plasma power increases, although the oxygen flow rate does not increase, the atomic oxygen supply increases. This suggests that during plasma-assisted MBE ZnO growth, oxygen rich condition can be obtained not only by decreasing Zn cell temperature or increasing oxygen flow rate, but also by increasing oxygen plasma power. Hall effect measurements results of the ZnO thin films were also summarized in Table 2.2.

Table 2.2 Hall effect measurements data of the ZnO thin films.

| Sample | Electron carrier concentration ($cm^{-3}$) | Resistivity ($\Omega$ cm) | Hall Mobility ($cm^2/Vs$) |
|---|---|---|---|
| A | $5.3 \times 10^{16}$ | 98 | 1.2 |
| B | $1.4 \times 10^{17}$ | 37 | 1.2 |
| C | $3.7 \times 10^{17}$ | 4.2 | 4.0 |
| D | $6.9 \times 10^{18}$ | 0.061 | 15 |
| E | $3.9 \times 10^{18}$ | 0.18 | 8.8 |
| F | $9.6 \times 10^{17}$ | 0.49 | 13 |

### 2.3.4 Optical properties

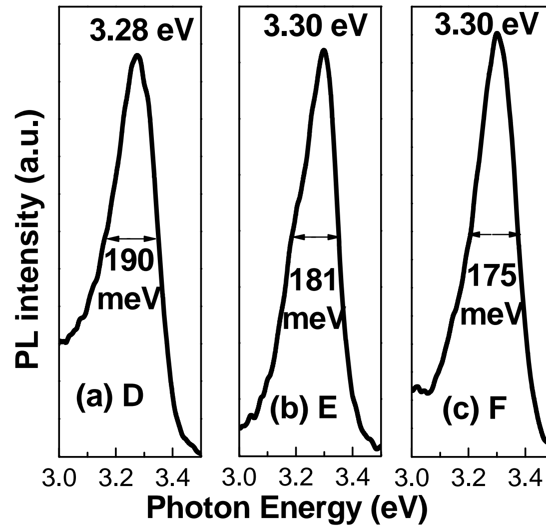


Fig. 2.6. Room-temperature PL emission spectra of samples D, E, and F around the NBE region. The FWHM of the ZnO NBE emission peaks decreases from 190 to 175 meV with increased plasma power from sample D to F.

Figure 2.6 shows room-temperature PL spectra of samples D, E, and F. The peaks around 3.30 eV are from ZnO near band-edge (NBE) emission. FWHM of the ZnO NBE emission peaks decreases from 190 to 175 meV from sample D to F. FWHM values of the PL peaks were also summarized in Table 2.3. Narrow room temperature PL peak width indicates small density of non-radiative centers. So it shows that better optical properties can be achieved with larger ECR oxygen plasma power during ZnO growth. The reason is also attributed to the decreased ionic oxygen density from enhanced plasma

power. The decreased ionic oxygen reduces the crystalline degradation of the ZnO film arising from the ionic oxygen hitting the film surface during growth. The density of the non-radiative centers of epitaxial grown materials is closely related to the crystallinity.

Table 2.3 Full-width at half-maximum (FWHM) of the ZnO $(11\bar{2}0)$ XRD and near band edge emission (NBE) PL peaks from the ZnO thin film sample D, E, and F at room temperature.

| Sample | FWHM of ZnO $(11\bar{2}0)$ XRD peak (°) | FWHM of ZnO NBE PL peak (meV) |
|---|---|---|
| D | 0.31 | 190 |
| E | 0.25 | 181 |
| F | 0.21 | 175 |

## 2.4 Summary

ZnO thin films were grown on *r*-plane sapphire substrates using ECR plasma-assisted MBE. ECR plasma power plays an important role to the growth rate and crystallinity of ZnO thin films. The effect of the oxygen ECR plasma power on the growth rate, structural, electrical, and optical properties of the ZnO thin films were studied. The growth rate increases with the increase of plasma power because of the increased atomic oxygen density. The enhanced plasma power improves ZnO film crystallinity, decreases the density of Zn interstitial defect formation, and improves

optical properties due to smaller density of non-radiative luminescence centers because of decreased ionic oxygen density.

### 2.5 Acknowledgement

Most of the results in this Chapter were published on *Applied Surface Science* 255, 3375 (2008). This work was supported by ONR/DMEA through the Center of Nanomateials and Nanodevice(CNN) under the award No. H94003-08-2-0803.

## References

[1] D. C. Look, Mater. Sci. Eng. B 80 (2001) 383.

[2] S. J. Pearton, D. P. Norton, K. Ip, Y. W. Heo, and T. Steiner, J. Vac. Sci. Technol. B 22 (2004) 932.

[3] Ü. Özgür, Ya. I. Alivov, C. Liu, A. Teke, M. A. Reshchikov, S. Doğan, V. Avrutin, S. -J. Cho, and H. Morkoç, J. Appl. Phys. 98 (2005) 041301.

[4] T. Sekiguchi, S. Miyashita, K. Obara, T. Shishido, N. Sakagami, J. Crystal Growth 214-215 (2000) 72.

[5] E. Ohshima, H. Ogino, I. Niikura, K. Maeda, M. Sato, M. Ito, T. Fukuda, J. Crystal Growth 264 (2004) 166.

[6] Z. C. Jin, I. Hamberg, C. G. Granqvist, J. Appl. Phys. 64 (1988) 5117.

[7] K. B. Sundaram, A. Khan, Thin Solid Films 295 (1997) 87.

[8] X. W. Sun, H. S. Kwok, J. Appl. Phys. 86 (1999) 408.

[9] B. J. Jin, S. H. Bae, S. Y. Lee, S. Im, Mater. Sci. and Technol. B 71 (2000) 301.

[10] B. J. Jin, S. Im, S. Y. Lee, Thin Solid Films 366 (2000) 107.

[11] C. R. Gorla, N. W. Emanetoglu, S. Liang, W. E. Mayo, Y. Lu, M. Wraback, H. Shen, J. Appl. Phys. 85 (1999) 2595.

[12] Y. Liu, C. R. Gorla, S. Liang, N. Emanetoglu, Y. Lu, H. Shen, M. Wraback, J. Electron. Mater. 29 (2000) 69.

[13] J. Ye, S. Gu, S. Zhu, T. Chen, L. Hu, F. Qin, R. Zhang, Y. Shi, Y. Zheng, J. Crystal Growth 243 (2002) 151.

[14] Z. Fu, B. Lin, J. Zu, Thin Solid Films 402 (2002) 302.

[15] M. A. L. Johnson, S. Fujita, W. H. Rowland Jr., W. C. Hughes Jr., J. W. cook, J. F. Schetzina, J. Electron. Mater. 25 (1996) 855.

[16] D. M. Bagnall, Y. F. Chen, Z. Zhu, T. Yao, S. Koyama, M. Y. Shen, T. Goto, Appl. Phys. Lett. 70 (1997) 2230.

[17] P. Zu, Z. K. Tang, G. K. L. Wong, M. Kawasaki, A. Ohtomo, H. Koinuma, Y. Segawa, Solid State Commun. 103 (1997) 459.

[18] Z. K. Tang, G. K. L. Wong, P. Yu, M. Kawasaki, A. Ohtomo, H. Koinuma, Y. Segawa, Appl. Phys. Lett. (1998) 3270.

[19] Y .Chen, D. M. Bagnall, H. Koh, K. Park, K. Hiraga, Z. Zhu, T. Yao, J. Appl. Phys. 84 (1998) 3912.

[20] H. Kato, M. Sano, K. Miyamoto, T. Yao, Jpn. J. Appl. Phys. 42 (2003) 2241.

[21] F. Vigué, P. Vennéguès, S. Vézian, M. Laügt, J. -P. Faurie, Appl. Phys. Lett. 79 (2001) 194.

[22] T. Ohgaki, N. Ohashi, H. Kakemoto, S. Wada, Y. Adachi, H. Haneda, T. Tsurumi, J. Appl. Phys. 93 (2003) 1961.

[23] K. Nakahara, T. Tanabe, H. Takasu, P. Fons, K. Iwata, A. Yamada, K. Matsubara, R.

Hunger, S. Niki, Jpn. J. App. Phys. 40 (2001) 250.

[24] F. X. Xiu, Z. Yang, L. J. Mandalapu, J. L. Liu, W. P. Beyermann, Appl. Phys. Lett. 88 (2006) 052106.

[25] F. X. Xiu, Z. Yang, L. J. Mandalapu, J. L. Liu, W. P. Beyermann, Appl. Phys. Lett. 88 (2006) 152116.

[26] Z. Yang, J. L. Liu, M. Biasini, and W. P. Beyermann, Appl. Phys. Lett. 92 (2008) 042111.

[27] Z. Yang, D. C. Look, and J. L. Liu, Appl. Phys. Lett. 94, (2009) 072101.

[28] T. E. Murphy, D. Y. Chen, E. Cagin, J. D. Phillips, J. Vac. Sci. Technol. B 23 (2005) 1277.

[29] K. Nakamura, T. Shoji, H. -B. Kang, Jpn. J. Appl. Phys. 39 (2000) L534.

[30] I. Sakaguchi, H. Ryoken, S. Hishita, H. Haneda, Thin Solid Films 506-507 (2006) 184.

[31] F. X. Xiu, Z. Yang, L. J. Mandalapu, D. T. Zhao, J. L. Liu, W. P. Beyermann, Appl. Phys. Lett. 87 (2005) 152101.

[32] F. X. Xiu, Z. Yang, L. J. Mandalapu, D. T. Zhao, J. L. Liu, Appl. Phys. Lett. 87 (2005) 252102.

[33] F. Xiu, Z. Yang, D. Zhao, J. Liu, K. A. Alim, A. A. Balandin, M. E. Itkis, R. C. Haddon, J. Crystal Growth 286 (2006) 61.

[34] F. X. Xiu, Z. Yang, D. T. Zhao, J. L. Liu, K. A. Alim, A. A. Balandin, M. E. Itkis, R. C. Haddon, J. Electron. Mater. 35 (2006) 691.

[35] K. Sakurai, D. Iwata, S. Fujita, S. Fujita, Jpn. J. Appl. Phys. 38 (1999) 2606.

[36] M. Fujita, N. Kawamoto, T. Tatsumi, K. Yamagishi, Y. Horikoshi, Jpn. J. Appl. Phys. 42 (2003) 67.

[37] N. Izyumskaya, V. Avrutin, W. Schoch, A. El-Shaer, F. Reuß, Th. Gruber, A. Waag, J. Crystal Growth 269 (2004) 356.

[38] M. Meyyappan, J. Nitride Semiconductor Research 2 (1997) 46.

[39] R. J. Molnar, T. D. Moustakas, J. Appl. Phys. 76 (1994) 4587.

# 3. Chapter 3 Gallium Doping in Zinc Oxide

## 3.1 Introduction

### 3.1.1 Current status of photoluminescence studies in ZnO

Photoluminescence (PL) properties in ZnO materials have been widely studied,[1-3] however, the origins of some characteristic PL lines in ZnO are not well clarified yet. For example, the origin of the PL lines locating at 3.30 – 3.32 eV in ZnO is still very controversial so far. These lines have been attempted to various assignments,[4] such as acceptor-bound excitons, donor-acceptor pairs (DAP), and free electrons to neutral acceptors, but never unambiguously defined. Another example is the $I_1$ PL line in ZnO, which lies above the common neutral donor-bound-exciton lines but below the free A exciton line. The $I_1$ line is widely observed in ZnO but its origin is also still controversial. Recently, we performed systematic PL studies in a series of Ga-doped ZnO thin films with different electron carrier concentrations ($n$),[5] which have applications in optoelectronic devices[6-8] and spintronics[9-11] and transparent conducting oxides.[12] Three dominant donor-related PL lines, which are neutral Ga donor-bound-exciton $I_8$ line (3.359 eV), $I_1$ line (3.368-3.371 eV), and $I_{DA}$ line (3.313-3.321 eV), were observed in these Ga-doped ZnO thin films.[5] The peak energies and strengths of these three dominant PL lines evolve with increasing $n$. We proposed a model to explain these lines and their evolutions by assigning $I_1$ and $I_{DA}$ as *ionized* Ga donor-bound-exciton and DAP lines,

respectively.[5] In this chapter, more comprehensive PL experimental results, including excitation power- and temperature-dependent, are presented.

### 3.1.2 Background of Ga-doping in ZnO

Althougth *p*-type doping has attracted more recent attention in ZnO research, *n*-type materials with high crystallinity and controllable electron carrier concentration (*n*) are also indispensable for optoelectronic and spintronic applications. For example, controllable *n* is important for ZnO-based dilute magnetic semiconductor materials, because their magnetic properties can be modulated by *n*.[9-10] Also, group-III-doped ZnO with large *n* is a potential candidate for replacing conventional transparent conducting oxides such as indium tin oxide. Among Group III elements, Ga is an excellent *n*-type dopant in ZnO with a more compatible covalent bond length (1.92 Å for Ga-O and 1.97 Å for Zn-O) than that of Al or In (2.7 Å for Al-O and 2.1 Å for In-O). Ga-doped ZnO has been widely studied,[13-31] however, among the Ga-related excitonic transitions, only excitons bound to *neutral* $Ga_{Zn}$ donors ($I_8$ in the literature) have been commonly reported.

## 3.2 Experiment

### 3.2.1 Sample preparation

The undoped and Ga-doped ZnO thin films were grown on *r*-plane sapphire

substrates using plasma-assisted molecular-beam epitaxy (MBE). The Zn and Ga sources were provided by radical Zn (6N) and Ga (6N) effusion cells, and the oxygen plasma was generated by a radio frequency plasma source sustained with $O_2$ (5N) gas. The $O_2$ flow rate can be precisely tuned using a mass flow controller. The sapphire substrates were cleaned by a 3-step process: the first step was chemical cleaning in a hot (~150 ºC) aqua regia ($HNO_3$: HCl = 1: 3) solution for 20 min, then rinsing in de-ionized water, and finally drying with a nitrogen gun before being transferred into the MBE chamber. Next, the substrates were thermo-annealed at 800 ˚C under vacuum for 20 min. Finally, oxygen plasma treatments were performed immediately before growth. Both the undoped (sample A) and Ga-doped (samples B-I) ZnO films were grown at 565 ˚C for 180 min. The $O_2$ flow rate was kept at 5 SCCM (standard cubic centimeter per minute) for all the samples, except that 2 SCCM was used for sample I. All samples were annealed *in situ* at 800 ˚C under vacuum for 20 min after growth to activate the Ga dopants and improve the film crystallinity. The electron carrier concentration $n$ of the Ga-doped ZnO thin films was controlled by the amount of Ga incorporation into the film, which in turn is determined by the ratio between Ga and Zn fluxes, controlled by the Ga and Zn effusion-cell temperatures.

Table 3.1 Growth parameters of the undoped and Ga-doped ZnO thin films.

| Sample | Description | Zn cell temperature (˚C) | Ga cell temperature (˚C) | $O_2$ flux (sccm) |
|---|---|---|---|---|
| A | Undoped ZnO | 370 | undoped | 5 |
| B | Ga-doped ZnO | 370 | 500 | 5 |
| D | Ga-doped ZnO | 370 | 525 | 5 |
| E | Ga-doped ZnO | 370 | 550 | 5 |
| F | Ga-doped ZnO | 370 | 575 | 5 |
| G | Ga-doped ZnO | 370 | 600 | 5 |
| H | Ga-doped ZnO | ~355 | 520 | 5 |
| I | Ga-doped ZnO | ~350 | 540 | 2 |
| C | Ga-doped ZnO | ~360 | 500 | 5 |

Firstly, the Zn cell temperature was fixed at 370 ˚C and the Ga cell temperature was tuned from 500 ˚C to 600 ˚C in a step of 25 ˚C. In this series, five Ga-doped ZnO samples, with values of $n$ at room-temperature (RT) ranging from $5.5\times10^{18}$ to $3.6\times10^{19}$ $cm^{-3}$ (samples B and D-G), were achieved. Then two more Ga-doped ZnO samples with larger $n$, up to $1.8\times10^{20}$ $cm^{-3}$ at RT, were grown with decreased Zn cell temperatures (samples H and I). Finally, a Ga-doped ZnO (sample C) with $n = 9.6\times10^{18}$ $cm^{-3}$ at RT,

which is in between that of samples B and D, was grown by precisely tuning the relative ratio between the Zn and Ga fluxes.

Table 3.2 The electron carrier concentrations of undoped and Ga-doped ZnO thin films at 300 K and 10 K.

| Sample | 300 K electron carrier concentration ($cm^{-3}$) | 10 K electron carrier concentration ($cm^{-3}$) |
|---|---|---|
| A | $1.9 \times 10^{18}$ | $1.8 \times 10^{18}$ |
| B | $5.5 \times 10^{18}$ | $3.6 \times 10^{18}$ |
| C | $9.6 \times 10^{18}$ | $8.8 \times 10^{18}$ |
| D | $1.5 \times 10^{19}$ | $1.5 \times 10^{19}$ |
| E | $2.3 \times 10^{19}$ | $2.2 \times 10^{19}$ |
| F | $2.5 \times 10^{19}$ | $2.4 \times 10^{19}$ |
| G | $3.6 \times 10^{19}$ | $3.5 \times 10^{19}$ |
| H | $7.4 \times 10^{19}$ | $7.4 \times 10^{19}$ |
| I | $1.8 \times 10^{20}$ | $1.8 \times 10^{20}$ |

The detailed growth parameters of these nine samples are summarized in Table 3.1. The 300 K and 10 K *n* values of the samples are shown in Table 3.2. The *n* values do

not show strong temperature dependence, since they are basically degenerate. In the following text, we refer to samples B and C as low-Ga-doped, samples D, E, and F as medium-Ga-doped, and samples G, H, and I as heavy-Ga-doped.

### 3.2.2 Characterizations

Reflection high-energy electron diffraction (RHEED) measurements were performed *in situ* on the as-grown samples in the MBE system. Hall-effect measurements were carried out using a Quantum Design physical properties measurement system (PPMS) in Hall bar geometry at 10 K and 300 K with various magnetic fields (1 – 10 T), and a LakeShore 7507 system in Van der Pauw geometry from 15 – 320 K at 1 T. The room-temperature Hall-effect data were further cross-checked using an Ecopia HMS-3000 Hall effect measurement system in Van der Pauw geometry at 1 T magnetic field. X-ray diffraction (XRD) measurements were performed using a Bruker D8 Advance x-ray diffractometer. Photoluminescence measurements were carried out using a home-built PL system. The 325-nm wavelength He-Cd laser was used as an excitation source and a photomultiplier tube was used to detect the PL signals. The resolution of the PL system was 0.15 nm, which is ~1.5 meV in the ultraviolet emission region. The temperature control from 9 K to 300 K in the PL system was achieved using a Janis Cryostat and a He compressor. Various excitation powers were achieved by filtering the

emitting laser.

## 3.3 Results and discussions

### 3.3.1 Structural properties

Figure 3.1 shows the XRD spectra of undoped sample A and heavily Ga-doped sample G. Only the ZnO and GaZnO $(11\bar{2}0)$ peaks are observed in the samples, indicating that both samples are single-crystalline and the heavy Ga doping does not significantly degrade the crystallinity of the film. The insets in Fig. 3.1 show the RHEED patterns of the two samples. Note the change from the streaky pattern of the undoped sample to the spotty pattern of the Ga-doped sample, which indicates that the surface of the film becomes rougher after heavy Ga doping.

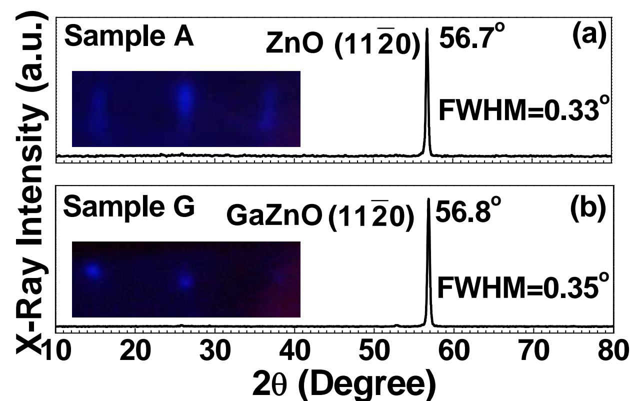


FIG. 3.1. XRD patterns of (a) undoped ZnO sample A and (b) heavy-Ga-doped ZnO sample G. The insets show the RHEED patterns of samples A and G, which are streaky and spotty, respectively.

### 3.3.2 Low temperature photoluminescence properties

Figures 3.2(a)-(i) show the 9K PL spectra of samples A to I. In the nine spectra, three basic PL peaks, designated $I_1$, $I_8$, and $I_{DA}$, are dominant: $I_1$, at 3.368-3.371 eV, is found in samples A to E; $I_8$, at 3.359 eV, in samples F to I; and $I_{DA}$, at 3.313-3.321 eV, in samples B to G. The $I_8$ line is the commonly accepted as the neutral Ga donor-bound-exciton recombination.[2,13-14] The $I_1$ line lies above the common neutral donor-bound-exciton lines, $I_9$(In), $I_8$(Ga), $I_6$(Al), and $I_4$(H), which span the range of 3.357 – 3.363 eV, but below the free A exciton line at 3.377 eV. It has been seen in the past[1-2] but never unambiguously identified. More recently, however, it has been associated with an exciton bound to an *ionized* Ga donor[15-16]. In almost all n-type ZnO samples, the intensity of $I_1$ is much less than that of $I_8$; however, several of our samples show exactly the opposite relationship, and we will give the reasons below.

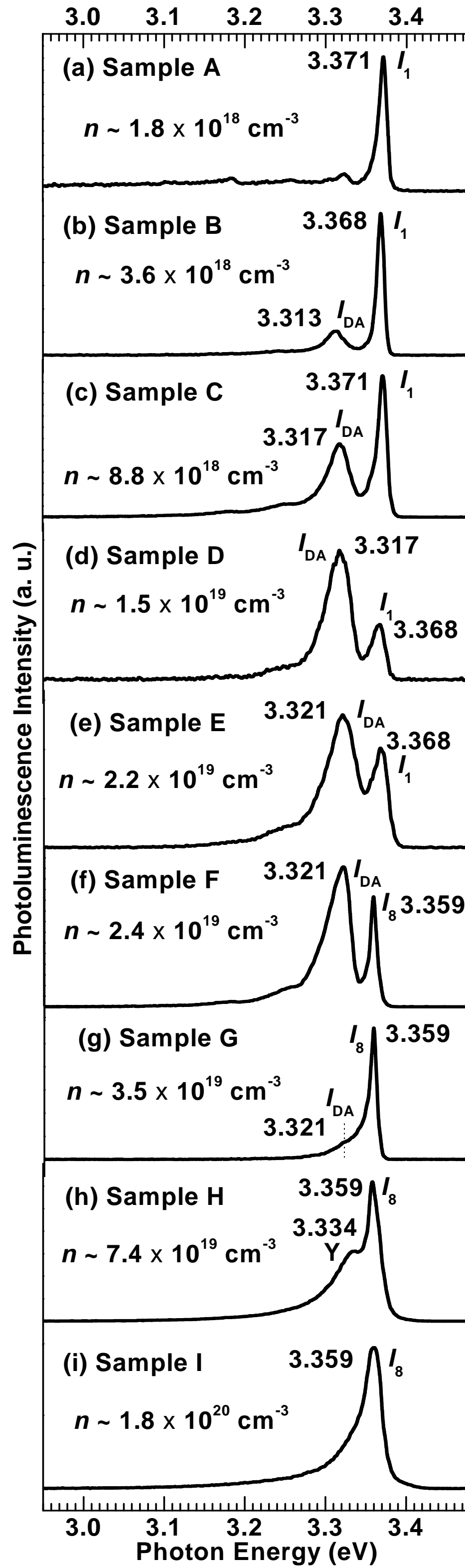


FIG. 3.2 PL spectra measured at 9 K for samples A to I [(a) to (i)].

The PL lines occurring in the region 3.30 – 3.32 eV have been variously assigned in the literature to many different transitions, including those involving acceptor-bound excitons, donor-acceptor pairs (DAPs), and free electrons to neutral acceptors.[4] In fact, more than one mechanism may contribute to luminescence in this region. Here we will argue that DAP transitions best describe line $I_{DA}$ in our case. Immediate support for this assignment arises from a study of the excitation-power dependence of the luminescence in sample E. In this sample, the $I_{DA}$ transition energy clearly blueshifts with excitation power (which is discussed in the subsection 3.3.3), whereas that of $I_1$ does not. This is a strong indication that $I_{DA}$ represents a DAP transition. Further support is presented below.

We propose that $I_{DA}$ consists of transitions between neutral $Ga_{Zn}$ donors and neutral Zn-vacancy ($V_{Zn}$) acceptors, or acceptor complexes. Obviously $Ga_{Zn}$ donors should be abundant in our samples, but $V_{Zn}$ acceptors also have low formation energies and are common in n-type ZnO.[33] In this scenario, the DAP transition would be written as: $Ga_{Zn}^0 + V_{Zn}^0 \rightarrow Ga_{Zn}^+ + V_{Zn}^-$. The photon emitted in this transition should have an energy,

$$E_{DA} = E_g - E_D(\mathrm{Ga}_{\mathrm{Zn}}^{0/+}) - E_A(\mathrm{V}_{\mathrm{Zn}}^{0/-}) + e^2 / 4\pi\varepsilon r_{DA} - E_{vdW} \qquad (3\text{-}1)$$

where $E_D(Ga_{Zn})$ = 55 meV from analysis of two-electron satellite spectra[2,14] and $E_A(V_{Zn})$

is estimated to be about 180 meV, as recently determined from density-functional theory (DFT).[34] The term $E_{coul} = e^2/4\pi\varepsilon r_{DA}$ is the Coulomb energy arising from the proximity between the donor and acceptor, and $E_{vdW}$ is the van der Waals (vdW) polarization energy associated with the dipole-dipole interaction.[35] The vdW term is very small compared to the Coulomb term when $r_{DA}$ is large, and hence is generally neglected. However, when $r_{DA}$ is small (say, < 2 nm), the contribution from the vdW term needs to be considered. The traditional vdW term is in the form of

$$E_{vdW} = \frac{e^2}{4\pi\varepsilon r_{DA}}\left(\frac{b}{r_{DA}}\right)^5 \qquad (3\text{-}2)$$

as proposed by Dean in GaP materials, with *b* a constant for a given donor and acceptor. [35] However, it was later found that this equation gives a very unsatisfactory result in II-VI materials, especially in the region of closer pairs ($r_{D\text{-}A}$ < 3 nm).[36] Instead, an exponential form

$$E_{vdW}[\text{eV}] = 0.06823 \times \exp(-1.312 \times r_{DA}[\text{nm}]) \qquad (3\text{-}3)$$

was employed by Neumark[37] to achieve a good fit. We will use Neumark's formula as a reasonable approximation for our samples, because $E_{vdW}$ is rather small compared to $E_{coul}$ and thus high accuracy in $E_{vdW}$ is not required.

Consider the PL spectrum for sample F in Fig. 3.2. Here $I_8$ is strong and $I_1$ does not appear in the linear plot, which indeed is typical of most ZnO samples that we have examined. To apply Eq. (3-1), we need to know the donor and acceptor concentrations,

$N_D$ and $N_A$, respectively. Measurement of these quantities requires temperature-dependent Hall-effect (T-Hall) measurements, and to analyze the T-Hall data we employ a general two-layer algorithm outlined in Ref. 32. The fitting results are: $N_{D1}$ = 6.3 x $10^{19}$, $N_{D2}$ = 7.0 x $10^{18}$, $N_{A1}$ = 4.0 x $10^{19}$, and $N_{A2}$ = 2.0 x $10^{18}$ $cm^{-3}$; and $d_1$ = 440 and $d_2$ = 20 nm. Here $N_{Di}$, $N_{Ai}$, and $d_i$, are the donor concentration, acceptor concentration, and thickness of layer i, respectively. Layer 2 is probably representative of the surface and/or interface regions, and is not of importance in this study. In the dark, at 10 K, the neutral donor concentration in layer 1 is $N_D^0 \approx N_D - N_A = 2.3 \times 10^{19}$ $cm^{-3}$, and the neutral acceptor concentration is $N^0_A \approx 0$, since almost all of the acceptors will be negatively charged. In the light, photogenerated electrons will create more $D^0$ through the reaction $e + D^+ \rightarrow D^0$, and photogenerated holes will create $A^0$ through the reaction $h + A^- \rightarrow A^0$. Of course, some of the photogenerated electrons and holes will also form free excitons, $h + e \rightarrow X$, and at 10 K most of these excitons will bind to neutral donors, forming $D^0X$. (Note that neutral *acceptors* are rarely seen in ZnO.) If these three reactions are the only ones available (or at least are dominant), then the photogenerated neutral donors and acceptors must be equal: $\Delta D^0 = \Delta A^0$. Since clearly $D^0 + \Delta D^0 > \Delta A^0$, the average distance between neutral donors and acceptors will be determined by the average distance between neutral donors; i.e., $r_{DA} \approx (3/4\pi N_D^0)^{1/3} \approx 2.2$ nm, assuming $N_D^0 >> \Delta N_D^0$. Then, applying Eqns. (3-1) and (3-3), $E_{DA}$ = 3.437 – 0.055 – 0.18 +0.081 –

0.004 = 3.279 eV. If on the other hand, it is assumed that the light neutralizes *all* of the donors, then $E_{DA}$ = 3.307 eV. With this and other uncertainties, including that in the DFT value [$E_A(V_{Zn}^{0/-})$ = 0.18 eV], our range of 3.279 – 3.307 eV is in good agreement with the experimental value, 3.321 eV. This agreement, along with the aforementioned observation of a blue shift with excitation intensity, justifies the assignment of $I_{DA}$ as a DAP transition involving $Ga_{Zn}$ donors and $V_{Zn}$ acceptors.

The other main PL line in Fig. 3.2(f), $I_8$, is almost universally acknowledged to be the $Ga_{Zn}$ $D^0X$ line. The existence of this line is entirely expected from the high concentration of neutral donors available for the reaction $D^0 + X \rightarrow D^0X$. Although the relative strengths of $I_8$ and $I_{DA}$ depend upon many factors, certainly one of these factors is the photogenerated neutral-acceptor concentration $\Delta A^0$. Indeed, as more Ga donors are added to the ZnO (cf. samples G, H, and I in Fig. 3.2), the reaction $e + h + D^0 \rightarrow D^0X$ may become more and more dominant over the reaction $h + A^- \rightarrow A^0$, thus favoring $I_8$ over $I_{DA}$.

Finally, we must explain the dominance of *ionized* donor-bound excitons in low-Ga-doped samples, such as sample A which has only background Ga doping. The occurrence of strong $D^+X$ transitions, represented by $I_8$, is very unusual. To explain this phenomenon, we again turn to the T-Hall fitting,[32] which for sample A [Fig. 3.2(a)] gives: $N_{D1} = 1.33 \times 10^{20}$, $N_{D2} = 6.5 \times 10^{19}$, $N_{A1} = 1.30 \times 10^{20}$, and $N_{A2} = 2.5 \times 10^{19}$ cm$^{-3}$; and $d_1$

= 199 and $d_2$ = 1 nm. Again, only layer 1 is of any importance, and in the dark we get $N_D^0$ = $N_D - N_A \approx 3 \times 10^{18}$ cm$^{-3}$, and $N_D^+ \approx N_A = 1.3 \times 10^{20}$ cm$^{-3}$. (Note that the compensation ratio $N_A/N_D$ is close to one for sample A. However, this is often the case in as-grown ZnO; see, e.g., Table I in Ref. 32.) Thus, $N_D^+ >> N_D^0$, so that in weak light the ionized donor-bound excitons $D^+X$ ($I_1$) might be expected to dominate over the neutral donor-bound excitons $D^0X$ ($I_8$). Even in stronger light, it takes three reactions to make $D^0X$ from $D^+$: (1) $e + h \rightarrow X$; (2) $e + D^+ \rightarrow D^0$; and (3) $X + D^0 \rightarrow D^0X$. The DAP analysis [Eq. (3-1)] for sample A follows that given earlier for sample F, and the results are that $E_{DA} \approx 3.243$ eV if there is almost no *additional* donor neutralization from the photoexcitation, and $E_{DA} \approx 3.334$ eV if all of the donors are neutralized and participate in DAP recombinations. The experimental value $E_{DA} \approx 3.323$ eV falls in this range; however the accuracy of this value may be poor, because the $I_{DA}$ intensity is quite weak and the line may overlap with other PL lines in this region. For example, there is a well-known line at 3.333 eV that often appears in ZnO. Further analysis of the relative line intensities and energies would require more detailed knowledge of the various capture cross sections and other factors.

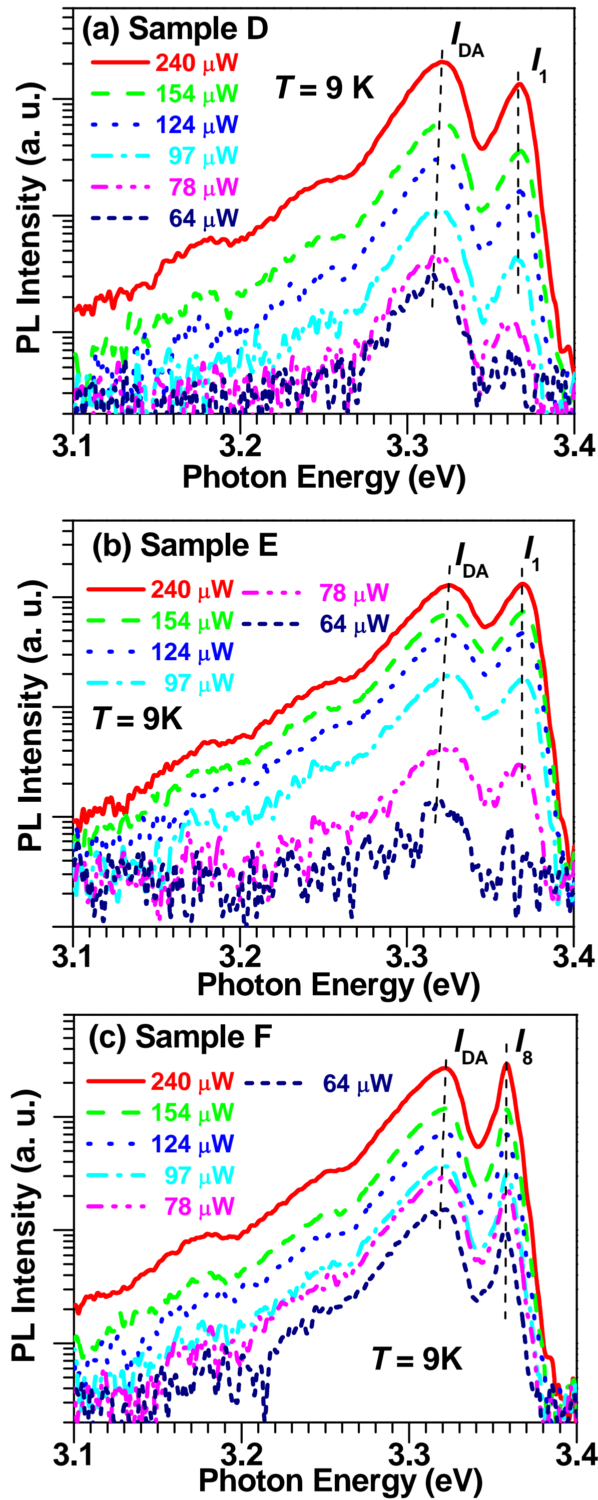


FIG. 3.3 Excitation power-dependent PL for samples D, E, and F [(a) to (c)] at 9 K.

### 3.3.3 Excitation power-dependent photoluminescence

An immediate support for the assignment of $I_{DA}$ line as a DAP transition is the excitation-power dependence of the luminescence. Figure 3.3(a)-(c) show the excitation power-dependent PL performed at 9 K on samples D, E and F. The $I_{DA}$ transition energy clearly blueshifts with increased excitation power, whereas that of $I_1$ does not in all three samples. This is a strong indication that $I_{DA}$ represents a DAP transition. The blue-shifted value is not large (esp. in sample F), which is due to the relatively small variation range of the excitation power (less than 4 times difference from 64 to 240 μW).

### 3.3.4 Temperature-dependent photoluminescence

Figures 3.4 (a)-(c) show temperature-dependent PL spectra of Ga-doped ZnO samples D, E, and F. As temperature increases, a DAP transition energy might be expected to shift in two different ways: (1) a blue shift due to the donor electron first being thermally excited to the conduction band (CB) before its radiative capture by the acceptor; and (2) a red shift due to bandgap shrinkage. At a given temperature, a fraction of the donor electrons in the DAPs will have been thermally excited to the CB before being captured by their paired acceptors, and those electrons will thus recombine with an

energy higher by about 55 meV, the donor energy. The overall blue shift might then be expected to be about 55 meV. On the other hand, the CB itself will have shifted downwards, leading to a red shift. These two effects will partially cancel each other, so the overall effect could be small. As seen in Fig. 3.4, from about 9 – 150 K, the $I_{DA}$ peak energy shows a blue shift ≤ 20 meV with increasing temperature in samples D and E, and an even smaller shift in sample F. Even though quantitative analysis is difficult with such small shifts, still the qualitative behavior of $I_{DA}$ is consistent with a DAP recombination model. We also observed that the $I_{DA}$ intensity decreases much more rapidly after temperature exceeding 50 K than below that, which is also consistent with DAP characteristics.

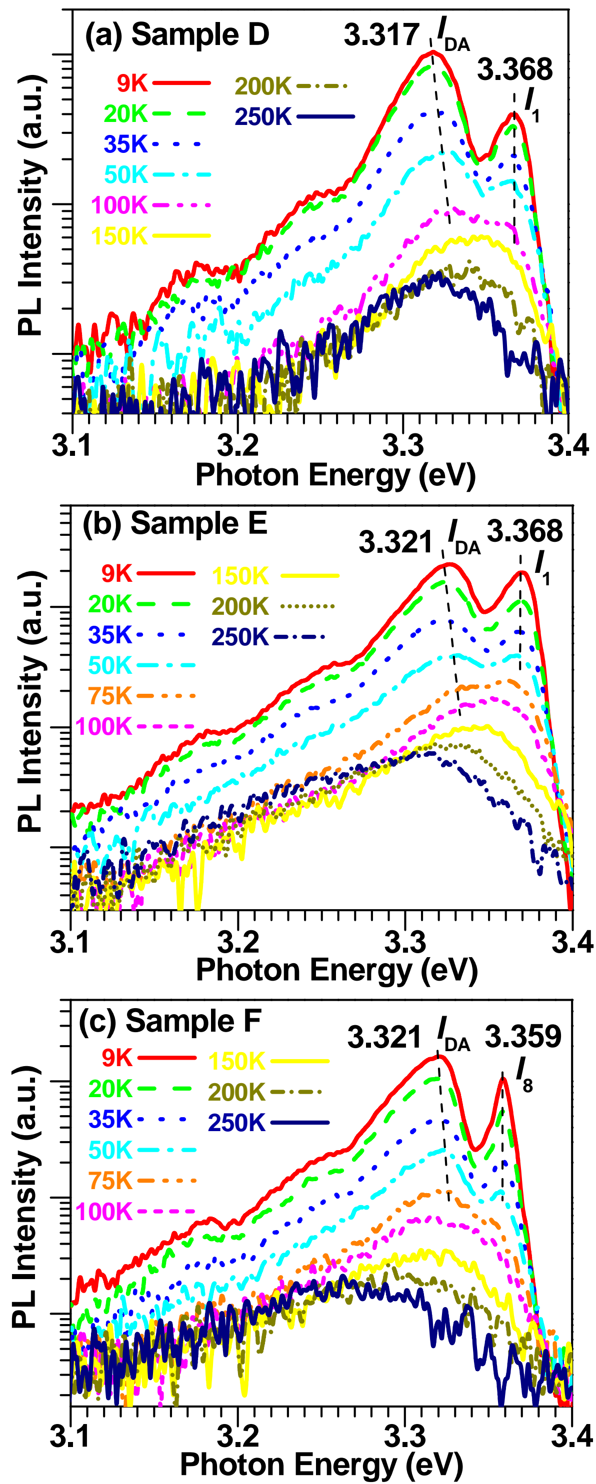


FIG. 3.4 Temperature-dependent PL for samples D, E, and F [(a) to (c)].

A more detailed picture of the $Ga_{Zn}$ donor-bound exciton $I_8$ in sample I is given in Fig. 3.5. The PL spectra as a function of temperature are presented in Fig. 3.5 (a), and their integrated intensities in Fig. 3.5 (b). Here the small contributions from the $I_{DA}$ peak at 3.321 eV are ignored, because their peak intensities are about two orders of magnitude smaller than the $I_8$ peak intensities, in each case. (Note that the data in Fig. 3.5(a) are on a log scale.) The temperature dependence of the integrated intensities was fitted to a common expression:

$$I(T) = \frac{I_0}{1 + \upsilon \cdot \exp(-E_b / k_B T)} \tag{3-4}$$

where $E_b$ is the binding energy of the donor bound exciton, $k_B$ is Boltzmann's constant, and $I_0$ and $\upsilon$ are fitting parameters. Here $I_0$ was approximated by $I_{9K}$. Such an analysis has been widely used in both ZnO [42-46] and other material systems such as GaN[47] and SiGe[48], to estimate physical parameters such as the exciton binding energy[42-47] and the carrier effective mass[48].

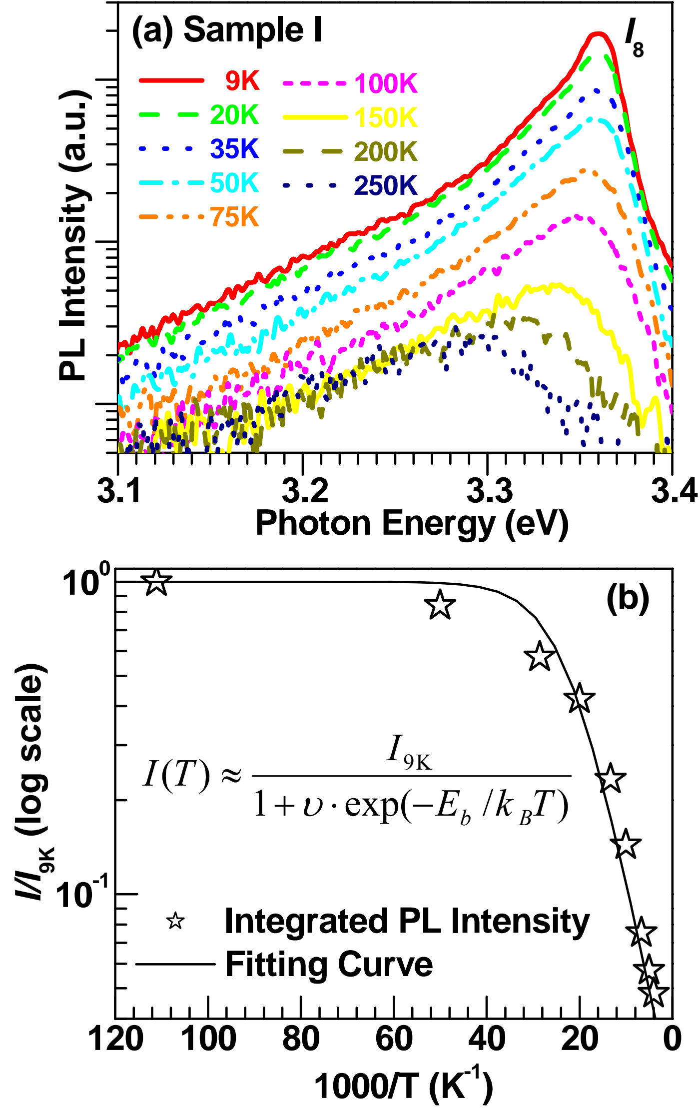


FIG. 3.5 (a) Temperature-dependent PL spectra of sample I. (b) Fit of the temperature dependence of the integrated PL intensity.

From the fitting, we obtain $E_b$ = 15 meV and $\nu$ = 44. If the free-exciton energy is taken to be 3.377 eV at low temperature, then the binding energy of an exciton to a $Ga_{Zn}$

donor should be 3.377 – 3.359 eV = 18 meV. The slight discrepancy between this and the fitting value might arise at least partially from ignoring the integrated line strength of $I_{DA}$ or of the free exciton itself, from the temperature difference between the sensor and the sample in the cryostat, and from fitting accuracy. Since $E_D$(Ga) = 55 meV, determined from an analysis of TES transitions[2,14], either measured value of $E_b$ is consistent with a Haynes factor[49] of 0.3.

### 3.4 Summary

In summary, we have carried out photoluminescence (PL) and Hall-effect measurements for a series of Ga-doped ZnO thin films grown by molecular-beam epitaxy. For high Ga doping, the PL spectra are dominated by the neutral-Ga donor-bound exciton $I_8$ at 3.359 eV, and for low Ga doping, the ionized-Ga donor bound exciton $I_1$ at 3.371 eV. The low-Ga spectra in this study demonstrate one of the first ever observations of higher $I_1$ intensity than that of $I_8$, and this phenomenon is explained by the T-Hall result that $[Ga^+] >> [Ga^0]$ in these low-Ga samples. For intermediate Ga doping, a line that ranges from 3.31 – 3.32 eV, designated as $I_{DA}$, is dominant. We have shown that $I_{DA}$ has characteristics of a donor-acceptor-pair transition, and have used a detailed, quantitative analysis to argue that it arises from $Ga_{Zn}$ donors paired with Zn-vacancy ($V_{Zn}$) acceptors. The success of our analysis depends upon, and lends credence to, a recent theoretical

calculation of the $V_{Zn}^{0/-}$ acceptor transition energy. The excitation power-dependent and temperature-dependent PL results support the DAP assignment well. A Haynes factor of 0.3 is derived based on low-temperature and temperature-dependent PL studies on heavily Ga-doped ZnO samples.

## 3.5 Acknowledgement

Some results in this chapter were published on *Applied Physics Letters* 94, 072101, (2009). This work was supported by ONR/DMEA through the Center of Nanomateials and Nanodevice(CNN) under the grant No. H94003-08-2-0803. ZY would like to thank Prof. W. P. Beyermann for his PPMS equipment and Dr. L. J. Mandalapu for her assistance of evaporation metal contacts on some samples. DCL was supported by AFOSR Grant FA9550-07-1-0013, NSF Grant DMR0513968, DOE Grant DE-FG02-07ER46389, and ARO Grant W911NF-07-D-0001/Task07275.

**References**

[1] D. C. Reynolds, C. W. Litton, and T. C. Collins, Phys. Rev. **140**, A1726 (1965).

[2] B. K. Meyer, H. Alves, D. M. Hofmann, W. Kriegseis, D. Forster, F. Bertram, J. Christen, A. Hoffmann, M. Straßburg, M. Dworzak, U. Haboeck, and A. V. Rodina, Phys. Stat. Sol. (b) **241**, 231 (2004).

[3] Ü. Özgür, Ya. I. Alivov, C. Liu, A. Teke, M. A. Reshchikov, S. Doğan, V. Avrutin, S.-J. Cho, and H. Morkoç, J. Appl. Phys. **98**, 041301 (2005).

[4] For a good review of these mechanisms, see M. Schirra, R. Schneider, A. Reiser, G.M. Prinz, M. Feneberg, J. Biskupek, U. Kaiser, C.E. Krill, K. Thonke, and R. Sauer, Phys. Rev. B **77**, 125215, (2008).

[5] Z. Yang, D. C. Look, and J. L. Liu, Appl. Phys. Lett. 94, 072101 (2009).

[6] L. J. Mandalapu, Z. Yang, F. X. Xiu, D. T. Zhao, and J. L. Liu, Appl. Phys. Lett. 88, 092103 (2006).

[7] S. Chu, J. H. Lim, L. J. Mandalapu, Z. Yang, L. Li, and J. L. Liu, Appl. Phys. Lett. 92, 152103 (2008).

[8] S. Chu, M. Olmedo, Z. Yang, J. Kong, and J. L. Liu, Appl. Phys. Lett. 93, 181106 (2008).

[9] Z. Yang, J. L. Liu, M. Biasini, and W. P. Beyermann, Appl. Phys. Lett. **92**, 042111 (2008).

[10] Z. Yang, M. Biasini, W. P. Beyermann, M. B. Katz, O. K. Ezekoye, X. Q. Pan, Y. Pu, J. Shi, Z. Zuo, and J. L. Liu, J. Appl. Phys. 104, 113712 (2008).

[11] Z. Yang, W. P. Beyermann, M. B. Katz, O. K. Ezekoye, Z. Zuo, Y. Pu, J. Shi, X. Q. Pan, and J. L. Liu, J. Appl. Phys., 105 (2009).

[12] K. Ellmer, A. Klein, and B. Rech edited, Transparent Conductive Zinc Oxide, (Springer Series in Materials Science Vol. 104), Springer, 2007.

[13] H. J. Ko, Y. F. Chen, S. K. Hong, H. Wenisch, T. Yao, and D. C. Look, Appl. Phys. Lett. **77**, 3761 (2000).

[14] D. C. Look, G. C. Farlow, P. Reunchan, S. Limpijumnong, S. B. Zhang, and K. Nordlund, Phys. Rev. Lett. **95**, 225502 (2005).

[15] F. Bertram, J. Christen, A. Dadgar, and A. Krost, Appl. Phys. Lett. **90**, 041917 (2007).

[16] B. K. Meyer, J. Sann, S. Lautenschläger, M. R. Wagner, and A. Hoffmann, Phys. Rev. B **76**, 184120 (2007).

[17] J. Hu and R. G. Gordon, J. Appl. Phys. **72**, 11 (1992).

[18] D. C. Reynolds, D. C. Look, and B. Jogai, J. Appl. Phys. **88**, 5760 (2000).

[19] T. Makino, Y. Segawa, S. Yoshida, A. Tsukazaki, A. Ohtomo, and M. Kawasaki, Appl. Phys. Lett. **85**, 759 (2004).

[20] J. D. Ye, S. L. Gu, S. M. Zhu, S. M. Liu, Y. D. Zheng, R. Zhang, and Y. Shi, Appl.

Phys. Lett. **86**, 192111 (2005).

[21] F. Reuss, S. Frank, C. Kirchner, R. Kling, Th. Gruber, and A. Waag, Appl. Phys. Lett. **87**, 112104 (2005).

[22] T. Makino, Y. Segawa, S. Yoshida, A. Tsukazaki, A. Ohtomo, and M. Kawasaki, J. Appl. Phys. 98, 093520 (2005).

[23] V. Bhosle, A. Tiwari, and J. Narayan, Appl. Phys. Lett. **88**, 032106 (2006).

[24] O. Nakagawara, Y. Kishimoto, H. Seto, Y. Koshido, Y. oshino, and T. Makino, Appl. Phys. Lett. **89**, 091904 (2006).

[25] V. Bhosle, A. Tiwari, and J. Narayan, J. Appl. Phys. **100**, 033713 (2006).

[26] V. Bhosle and J. Narayan, J. Appl. Phys. **100**, 093519, (2006).

[27] J. H. Kim, B. D. Ahn, C. H. Lee, K. A. Jeon, H. S. Kang, and S. Y. Lee, J. Appl. Phys. **100**, 113515 (2006).

[28] T. Yamada, A. Miyake, S. Kishimoto, . Makino, N. Yamamoto, and T. Yamamoto, Appl. Phys. Lett. **91**, 051915 (2007).

[29] M. Snure and A. Tiwari, J. Appl. Phys. **101**, 124912 (2007).

[30] V. Bhosle, J. T. Prater, F. Yang, D. Burk, S. R. Forrest, J. Narayan, J. Appl. Phys. **102**, 023501 (2007).

[31] H. C. Park, D. Byun, B. Angadi, D. H. Park, W. K. Choi, J. W. Choi, and Y. S. Jung, J. Appl. Phys. **102**, 073114 (2007).

[32] D.C. Look, J. Appl. Phys. **104**, 063718 (2008).

[33] F. Tuomisto, V. Ranki, K. Saarinen, and D. C. Look, Phys. Rev. Lett. **91**, 205502 (2003).

[34] A. Janotti and C.G. Van de Walle, Phys. Rev. B 76, 165202 (2007).

[35] P. J. Dean, Prog. Solid-State Chem. **8**, 1 (1973).

[36] K. Shahzad, B. A. Khan, D. J. Olego, and D. A. Cammack, Phys. Rev. B **42**, 11240 (1990).

[37] G. F. Neumark, Phys. Rev. B **29**, 1050 (1984).

[38] G. D. Gilliland, Mater. Sci. and Tech **R18**, 99 (1994).

[39] J. J. Hopfield, D. G. Thomas, M. Gershenzon, Phys. Rev. Lett. **10**, 162 (1963).

[40] G. Lucovsky, A. J. Varga, and R. F. Schwartz, Solid State Commun. **3**, 9 (1965).

[41] E. H. Bogardus and H. Bebb, Phys. Rev. **176**, 993 (1968).

[42] Y. R. Ryu, T. S. Lee, and H. W. White, Appl. Phys. Lett. **83**, 87 (2003).

[43] T. S. Jeong, M. S. Han, C. J. Youn, and Y. S. Park, J. Appl. Phys. **96**, 175 (2004).

[44] F. X. Xiu, Z. Yang, L. J. Mandalapu, D. T. Zhao, and J. L. Liu, Appl. Phys. Lett. **87**, 252102 (2005).

[45] F. X. Xiu, Z. Yang, L. J. Mandalapu, and J. L. Liu, Appl. Phys. Lett. **88**, 152116 (2006).

[46] J. D. Ye, S. L. Gu, F. Li, S. M. Zhu, R. Zhang, Y. Shi, Y. D. Zheng, X. W. Sun, G. Q.

Lo, and D. L. Kwong, Appl. Phys. Lett. **90**, 152108 (2007).

[47] D. G. Chtchekine, G. d. Gilliland, Z. C. Feng, S. J. Chua, D. J. Wolford, S. E. Ralph, M. M. Schurman, and I. Ferguson, MRS J. Nitride Semicond. Res. **4S1**, G6.47 (1999).

[48] Z. Yang, Y. Shi, J. Liu, B. Yan, R. Zhang, Y. Zheng, and K. L. Wang, Mater. Lett. **58**, 3765 (2004).

[49] J. R. Haynes, Phys. Rev. Lett. **4**, 361 (1960).

# 4. Chapter 4 Antimony Doping in Zinc Oxide

## 4.1 Introduction

### 4.1.1 Background of *p*-type doping in ZnO

Undoped zinc oxide (ZnO) is *n*-type because of the "intrinsic" shallow donors such as Zn interstitial ($Zn_i$)[1], $Zn_i$-related complexes[2], hydrogen (H)[3], and H-related complexes[4] inside ZnO. Furthermore, it has been theoretically calculated that the formation energy of the intrinsic donors in ZnO, such as $Zn_i$ and oxygen vacancy ($V_O$), is much lower than that of the intrinsic acceptors in ZnO, such as oxygen interstitial ($O_i$) and Zn vacancy ($V_{Zn}$).[5] So, reliable *p*-type ZnO is difficult to be achieved due to this asymmetrical formation energies between the intrinsic donors and acceptors and the forementioned intrinsic shallow donors in ZnO, although researchers have been putting their efforts on the *p*-type ZnO for many years.[6] Different dopants have been tried to achieve *p*-type ZnO materials, such as group-I elements (Li, Na, Ag, and Cu) and group-V elements (N, P, As, Sb, and Bi). Li and Na could be shallow acceptors in ZnO if they are in substitutional states for Zn sites,[5] however, these elements prefer interstitial states in ZnO due to their relatively small atom sizes, which become donors states. Among all these potential acceptor candidates, N, P, As, and Sb seem to have better chances to achieve *p*-type doping in ZnO and working devices. N has close atom size as O and $N_O$ is a relatively shallow acceptor, however, the solubility of N and compensation from formation of $N_2$ molecules in ZnO is an issue. Successful *p*-type doping[7] and

devices[8] in ZnO through N were previously demonstrated. Since As and Sb have larger atomic size than O, both theoretical calculations and experimental results prove that these atoms prefer to occupy the Zn rather than O sites, and simultaneously two $V_{Zn}$'s might be adjacent to form. The complexes $As_{Zn}$-$2V_{Zn}$ (or $Sb_{Zn}$-$2V_{Zn}$), representing as an acceptor in ZnO. Successful *p*-type doping[9] and devices[10] in ZnO through As were previously demonstrated by Ryu *et al*. Sb-doped ZnO materials and devices are discussed in detail in this chapter. The case of P is in between N and As/Sb, both $P_O$ and $P_{Zn}$-$2V_{Zn}$ states were claimed previously, and amphoteric doping results were reported.[11] However, *p*-type doping[12-13] and devices[14] in ZnO through P were also previously demonstrated to be not reliable.

### 4.1.2 Review of *p*-type Sb-doping in ZnO and related devices

Here, I will briefly review and summarize the previous successful *p*-type doping in ZnO and devices based on Sb-doping. It was commonly accepted that *p*-type doping in ZnO through Sb was firstly predicted by Limpijumnong *et al* based on theoretical calculations,[15] in which it has been proposed that $Sb_{Zn}$-$2V_{Zn}$ complexes, providing a net hole each, will be formed when Sb is doped into ZnO. Actually, before the theoretical predication, some studies have already been attempted on *p*-type doping in ZnO through Sb (e.g. Ref. 16), in which the preparation methods of the ZnO are thermal oxidation of

other Zn compounds and the Sb doping was achieved by excimer laser burning the pre-deposited Sb layer. So these film can hardly be employed for optoelectronic application even *p*-type was indeed achieved due to the poor quality arisen from the growth methods. Furthermore, the hole concentration (~$10^{20}$ $cm^{-3}$) is unbelievably high there, hence, the reliability is questionable. First epitaxial *p*-type Sb-doped ZnO (ZnO:Sb) thin films were obtained by Xiu *et al* using a molecular beam epitaxy (MBE) system on Si substrates.[17-18] Soon later, Sb-doped *p*-type ZnO[19] and MgZnO[20] thin films on sapphire substrates were achieved. Then the Ohmic contacts on Sb-doped *p*-type ZnO thin films have been systematically studied.[21-22] Followed by these results, prototype hetero-[23] and homo-*pn*-junctions[24] based on *p*-type ZnO:Sb have been demonstrated. However, no light comes out on these ZnO:Sb-based junctions, until the first ZnO:Sb light-emitting-diode (LED) was fabricated by Mandalapu *et al* recently.[25] In this ZnO LED device, ZnO:Sb and undoped ZnO were used for *p*- and *n*-layers, respectively. In this LED, the ultraviolet (UV) near-band-edge (NBE) electroluminescence (EL) emissions were observed at low-temperatures and room-temperature, even though the deep level emission dominates in the EL spectra. Subsequently, a Ga-doped ZnO (ZnO:Ga) with larger electron carrier concentration (*n*) was employed replacing the undoped ZnO as the *n*-layer in the device, then a ZnO LED with UV NBE EL emissions dominating in the spectra at low temperatures were demonstrated.[26] After further optimizations of the epitaxial film

growth and device fabrications, room-temperature UV NBE EL emissions dominating ZnO:Sb/ZnO:Ga LED was achieved.[27] Most recently, electrically pumped random lasing effect was observed in a *p*-ZnO:Sb/*n*-ZnO:Ga based diode with two thin MgZnO barrier layers confining the active recombination ZnO layer.[28] These results prove that the Sb doping in ZnO is effective and interesting. In this chapter, we summarize continuing study on ZnO:Sb *p*-doping and further discuss the Sb doping mechanism and preference in ZnO.

## 4.2. Experiment

### 4.2.1 Sample preparation

The Sb-doped ZnO thin films were grown using plasma-assisted MBE. The Zn and Sb sources were provided by radical Zn (6N) and Sb (6N) effusion cells, and the oxygen plasma was generated by an electron-cyclotron-resonance (ECR) or a radio-frequency (RT) plasma source sustained with $O_2$ (5N) gas. The $O_2$ flow rate can be precisely tuned using a mass flow controller. Different substrates, including Si (100), Si (111), $SiO_2$, *r*-plane sapphire, and *c*-plane sapphire were used for the ZnO:Sb thin film epitaxial growth.

All Si substrates were cleaned with a modified Piranha-HF method. First, the substrate was dipped in Piranha solution ($H_2O_2$:$H_2SO_4$ = 3:5) for 1 min and then in an

aqueous HF solution (HF: $H_2O$ = 1:10) for 1 min to hydrogenate the substrate surface. This procedure was repeated three times. Four steps were followed during the growth process. Next, the Si substrate was thermally cleaned at 650 ˚C for 10 min to disassociate hydrogen bonds, leaving a fresh Si surface for subsequent growth. All sapphire substrates were cleaned by a 3-step process: the first step was chemical cleaning in a hot (~150 ºC) aqua regia ($HNO_3$: HCl = 1: 3) solution for 20 min, then rinsing in de-ionized water, and finally drying with a nitrogen gun before being transferred into the MBE chamber. Next, the substrates were thermo-annealed at 800 ˚C under vacuum for 20 min. Finally, oxygen plasma treatments were performed immediately before growth. All as-grown ZnO:Sb thin films were annealed *in situ* under vacuum in MBE chamber to thermally activate the Sb dopants. $SiO_2$ substrates with acetone and alcohol alternately for several times, and then rinsed by de-ionized (DI) water and dried by nitrogen gun.

### 4.2.2 Characterizations

Hall-effect measurements were carried out using a Quantum Design physical properties measurement system (PPMS) in Hall bar and Van der Pauw geometries at different temperatures with various magnetic fields (1 – 10 T). And the room-temperature Hall-effect data were further cross-checked using an Ecopia HMS-3000 Hall effect measurement system in Van der Pauw geometry at 1 T magnetic field. X-ray diffraction

(XRD) measurements were performed using a Brucker advanced D8 X-ray diffractometer with Cu Kα radiation ($\lambda$ = 1.5406 Å). The acceleration voltage and current were 40 kV and 40 mA, respectively. All measurements were performed using a parallel plate detector. $\theta$-$2\theta$ scans were recorded to determine the crystalline orientation of the films. Another mode of grazing incidence (GI) geometry was used for $\theta$-$2\theta$ scans in order to access specific out of plane reflection. X-ray photoelectron spectroscopy (XPS) was carried out by a Thermo VG250 spectrometer fitted with a monochromatic Al Kα X-ray source (1487 eV). Photoluminescence (PL) measurements were carried out using a home-built PL system. The 325-nm wavelength He-Cd laser was used as an excitation source and a photomultiplier tube was used to detect the PL signals. The resolution of the PL system was 0.15 nm, which is ~1.5 meV in the ultraviolet emission region. The temperature control from 9 K to 300 K in the PL system was achieved using a Janis Cryostat and a He compressor. Various excitation powers were achieved by filtering the emitting laser. Scanning electron microscopy (SEM) meausrements were performed using a Leo SUPRA 55 SEM/E-beam lithography system with resolutions from 4nm at 1kV to 1nm at 15kV, and magnification from 12 to 900,000 times, respectively.

### 4.3. Results and discussions

Two parts are presented in this section. In the first part, the characterizations and

properties of typical *p*-type ZnO thin films, such as XRD, XPS, PL, and Hall effect, are shown and discussed. In the second part, the Sb doping mechanism and preference are discussed.

### 4.3.1 Typical characterizations and properties of *p*-type ZnO:Sb thin films

#### 4.3.1.1 X-ray diffraction (XRD)

The crystal structures of ZnO:Sb thin films were studied by XRD measurements in $\theta$-$2\theta$ and GI scans. Fig. 4.1(a) and (b) show the $\theta$-$2\theta$ XRD patterns of a typical ZnO:Sb sample A grown on Si (100) substrate and a typical ZnO:Sb sample B grown on Si (111) substrate, respectively. The growth orientations of ZnO:Sb thin films were identified as *c*-direction. It is found that both films in Figs. 4.1 (a) and (b) show strong (0002) peaks at 34.415° of samples A and 34.558° of sample B, corresponding to a preferential growth orientation along *c*-axis. GI x-ray diffraction was conducted to determine the in plane surface structures. Fig. 4.1(c) and (d) show the GI XRD patterns of ZnO:Sb sample A and ZnO:Sb sample B, respectively. Both \ samples show multi-peaks as shown in Figs. 4.1(c) and (d) including the ZnO ($10\bar{1}0$) and ZnO ($11\bar{2}0$) peaks, which confirms the polygrain along *c* axis growth mode. Based on the XRD and GIXRD peak position, length of lattice constant *c* and *a* can be calculated by Bragg's equation. For samples A and sample B, the lattice constants *c* are 5.210 Å and 5.189 Å, and *a* are 3.239 Å and

3.248 Å, respectively. In comparison to a fully relaxed ZnO film with c=5.2042–5.2075 Å, and a=3.2475-3.2501 Å.[29]

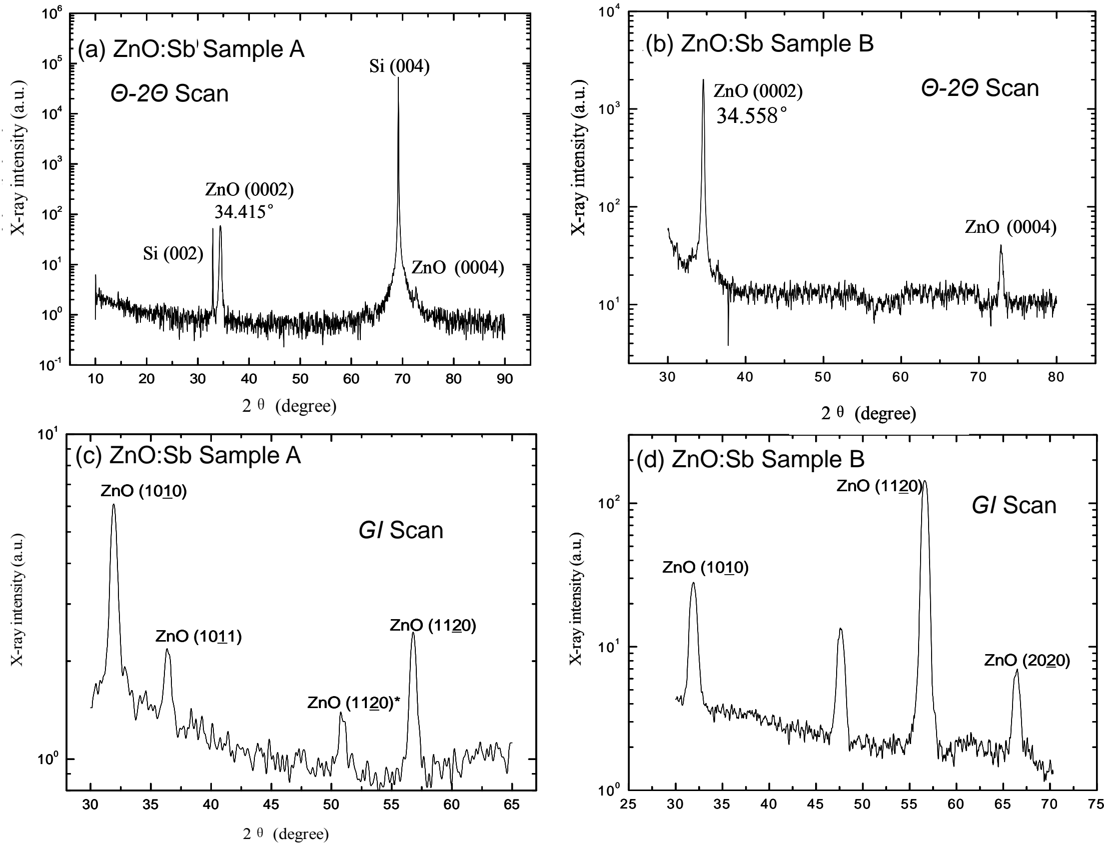


FIG. 4.1. Room temperature XRD patterns of (a) a typical *p*-type ZnO:Sb thin film sample A grown on Si (100) substrate and (b) a typical *p*-type ZnO:Sb thin film sample B grown on Si (111) substrate in $\theta$-$2\theta$ geometry. Grazing incidence XRD patterns of (c) ZnO:Sb sample A and (d) ZnO:Sb sample B. (Courtesy to Sheng Chu.)

However, the GIXRD measurements reflect a thin layer of only several nanometers near surface because of the nature of its small grazing angel, whereas the *c* represents the situation of the whole film. Therefore, sample A has compress stress on the

surface but the sample B is almost relaxed. Yuk *et al* observed an increase of distance between the (0001) planes of ZnO on Si (001),[30] suggesting a nonuniform strain distribution along the growth direction. Under this analysis, we can make the interpretation more clear: the layers near the interface between ZnO and Si are strongly strained by the ultra large lattice mismatch, where the *a* plane is highly compressed and so there is tensile strain along *c* axis. During growth the strain is gradually reduced by the formation of defect, and in sample B on Si (111) thin film is nearly fully relaxed. The surface of sample A on Si (100) could also be partially strained, although there is still compress strain in *a* plane from GIXRD results, indicating sample A has a stronger overall strain compared to sample B. This can be explained by the smaller ratio of lattice mismatch on Si (111) than Si (100) and more favorable with ZnO lattice structure, since the Si (111) surface is hexagonal and with a smaller lattice constant of 3.840 Å compared to cubic Si (100), and larger lattice constant of 5.431 Å.

#### 4.3.1.2 X-ray photoelectron spectroscopy (XPS)

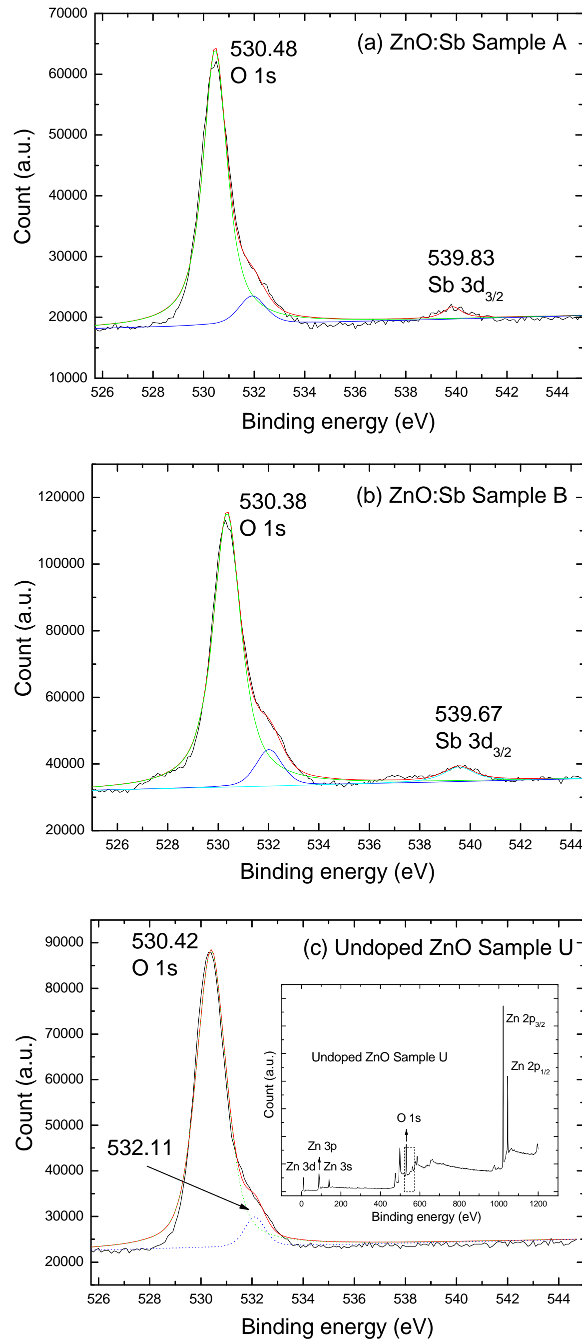


FIG. 4.2 Room temperature XPS spectra for the (a) ZnO:Sb sample A, (b) ZnO:Sb sample B, and (c) undoped ZnO thin film sample U. The inset in (c) shows the XPS spectra of sample U in a wider scanning range. (Courtesy to Sheng Chu.)

XPS measurements were performed on the ZnO:Sb thin films to investigate the chemical bonding of Sb in ZnO. Figs. 4.2(a) and (b) show the XPS spectra ZnO:Sb thin film samples A and B, respectively. Fig. 4.2(c) shows the XPS spectra of an undoped ZnO sample U for comparison with an inset showing a larger scanning range. The peaks around 530.2 eV in both ZnO:Sb and undoped ZnO samples can be assigned to $O^{2-}$ in the Zn-O bonds, and the small peak in the higher energy shoulder is attributed to chemisorbed oxygen.[31] Absent from the XPS spectra of the undoped ZnO [Fig. 4.2(c)], the ZnO:Sb shows Sb-related peaks at 539.8 eV in sample A and 539.6 eV in sample B. The appearance of this peak indicates that Sb dopants were incorporated into the ZnO film. In addition, by integrating the peak intensities, the Sb percentage of about 1.45 at% and 2.74 at% were obtained for sample A and B, respectively.

#### 4.3.1.3 Photoluminescence (PL)

Fig. 4.3(a) and (b) show the temperature-dependent PL spectra of ZnO:Sb sample A and B from 8.5 to 300 K. Sb-related peaks appearing at 3.358-3.359 eV, 3.222-3.223 eV and 3.03-3.07 eV dominate in the 8.5 K PL spectra, which were asigned as acceptor-bound exciton ($A^oX$), donor-acceptor pair (*DAP*), and Zinc vacancy related peak, respectively. In addition, a peak at 3.296 eV assigned as free electron to acceptor

transition (*FA*) was observed in sample A as show in Fig. 4.3(a). With increasing temperature, this peak *FA* merges into the $A^0X$. From our previous studies, Zn vacancy-related emission at ~3.0 eV indicates that Sb doping into ZnO can introduce the formation of Zn vacancies. This peak is important for achieving *p*-type ZnO:Sb.

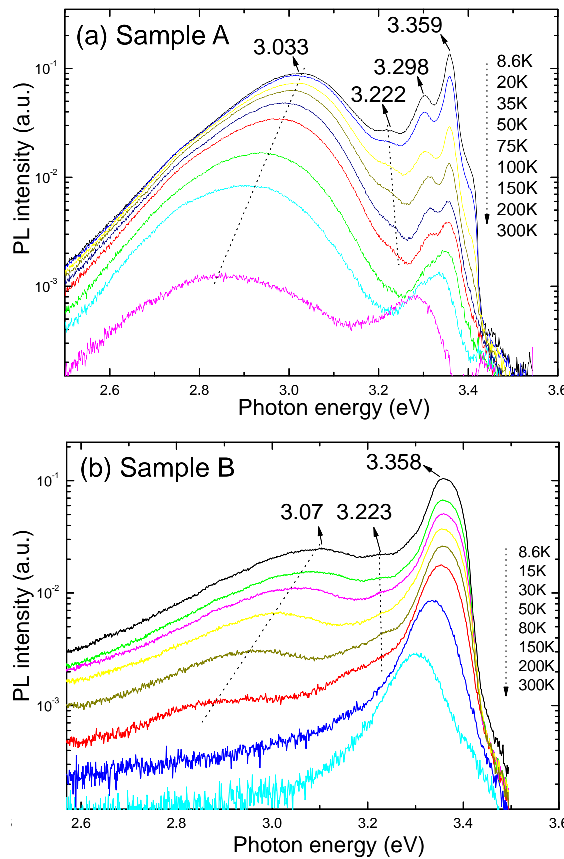


FIG. 4.3 PL spectra of (a) ZnO:Sb sample A and (b) ZnO:Sb sample B at various temperatures ranging from 8.5 to 300 K. (Courtesy to Sheng Chu and Dr. Faxian Xiu.)

The temperature dependence of the PL peaks in the spectra also confirms the

peak assignments. The 3.222 eV emission-lines are observed to blue-shift with the increase of temperature, which is typical behavior for a *DAP* transition. It is interesting to note that at higher temperatures the ~3.0 eV Zn vacancy related emissions show a large red-shift with relatively deeper energy levels, possibly indicating that these isolated Zn vacancies may not contribute to *p*-type conductivity unless they are bound to $Sb_{Zn}$ forming the $Sb_{Zn}$-$2V_{Zn}$ acceptor complex.

#### 4.3.1.4 Hall effect measurements

Fig. 4.4(a) shows the temperature-dependent hole carrier concentration ($p_H$) of *p*-type ZnO:Sb thin film sample A. The inset of Fig. 4.4(a) shows the magnetic field dependent Hall resistance ($R_{Hall}=V_{Hall}/I_x$) at a temperature of 300 K; the positive slope of the Hall coefficient (also the Hall resistance) indicates *p*-type conduction. The temperature range in Fig. 4.4(a) is only the extrinsic region. Fig. 4.4(b) shows the Hall mobility $\mu_H$ as a function of temperature. A value of 20.0 $cm^2/V$ s and 1900.0 $cm^2/V$ s were measured at 300 K and 40 K, respectively. This high mobility value could be relevant to the Si substrate. Over this temperature range, $\mu_H \sim T^{-3/2}$, indicating phonon scattering dominates at these temperatures. The inset of Fig. 4.4(b) shows the electrical resistivity as a function of temperature.

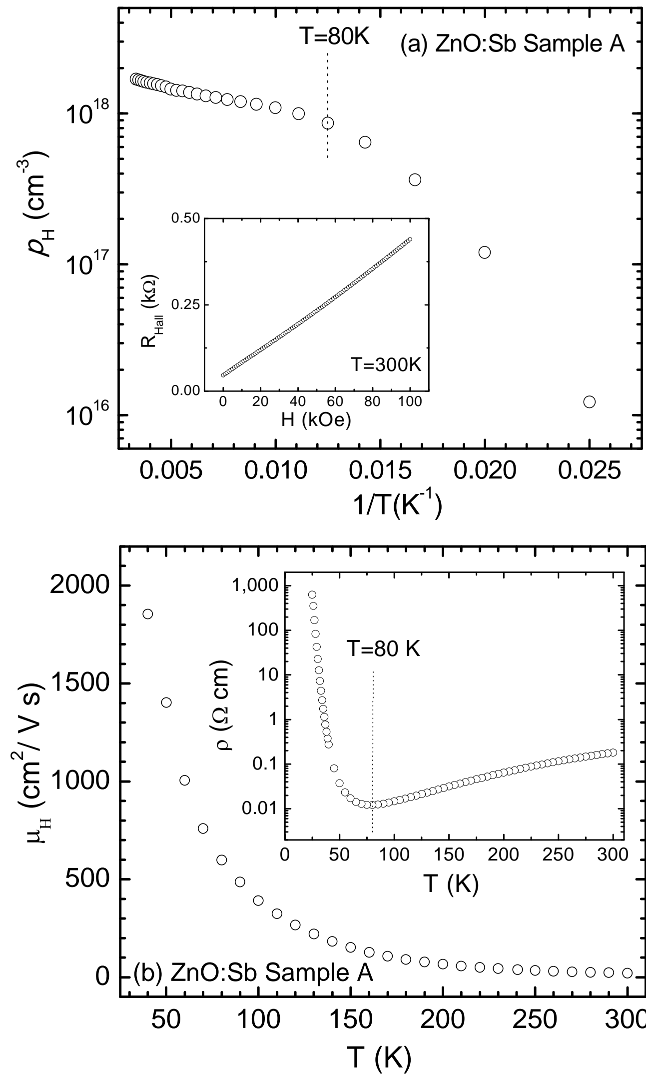


FIG. 4.4 (a) Temperature dependence of the hole concentration of ZnO:Sb sample A. The inset shows the Hall resistance as a function of applied magnetic field at T = 300 K. (b) Temperature dependence of the Hall mobility of ZnO:Sb sample A. The inset shows the temperature dependence of electrical resistivity. (Courtesy to Dr. Faxian Xiu.)

### 4.3.1 Sb doping mechanism and preference in ZnO thin films

#### 4.3.2.1 Sb doping mechanism in ZnO

Figure 4.5 shows the theoretical calculations on the Sb- and O-related defect

formation energy in ZnO under O-rich condition based on density function theory. The slope of the curves reflects the charge state of the defects and the solid dots denote the energy positions at which transition from one charge state to another takes place. The first-principle calculations show that $Sb_O$ have very high acceptor-ionization energies, and it is not possible for $Sb_O$ to efficiently dope ZnO to *p*-type.[15] Instead, Sb goes the Zn and simultaneously induce two Zn vacancies to form a complex ($Sb_{Zn}$–$2V_{Zn}$). This complex has a low acceptor-ionization energy of 160 meV to serve as a shallow acceptor to provide p-type conductivity.[15] Formation energy as the function of Fermi energy of this complex and other native defects calculated under the oxygen-rich limit ($\mu_O = 0$) was shown in Fig. 4.5. The acceptor complex $Sb_{Zn}$–$2V_{Zn}$ has the lowest formation energy $\Delta H_f(q=0)$=2.0 eV among all Sb related complexes.

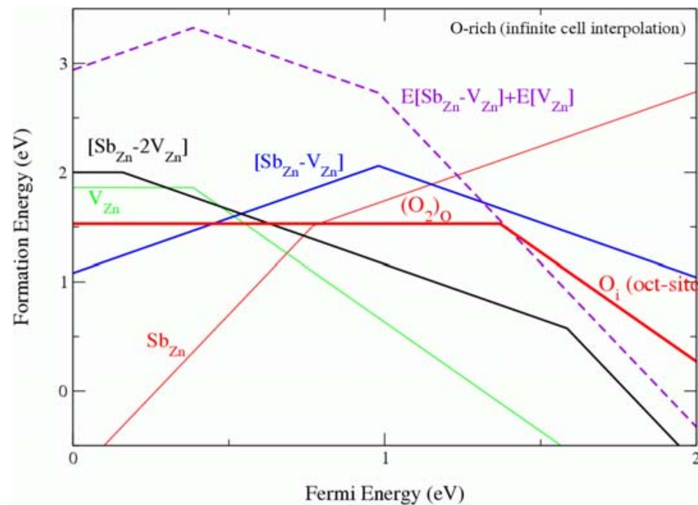


FIG. 4.5 Calculated Sb- and O-related defect formation energy in ZnO under O-rich condition. The slope of the curves reflects the charge state of the defects and the solid dots denote the energy positions at which transition from one charge state to another takes place. (Courtesy to Porf. Sukit Limpijumnong.)

#### 4.3.2.2 Sb doping preference in ZnO

Table 4.1 The Carrier type and concentration of ZnO:Sb samples grown on different substrates.

| Sample | Substrate | Type | Carrier Concentration ($cm^{-3}$) |
|---|---|---|---|
| A | Si (100) | *p* | $1.7 \times 10^{18}$ |
| B | Si (111) | *p* | $7.7 \times 10^{18}$ |
| C | Si (100) | *p* | $1.1 \times 10^{19}$ |
| D | Si (111) | *p* | $1.0 \times 10^{16}$ |
| E | $SiO_2$ | *n* | $1.8 \times 10^{19}$ |
| F | *r*-sapphire | *n* | $1.4 \times 10^{18}$ |
| G | *c*-sapphire | not reliable, changes with time passing by | |

Fig. 4.6 (a)-(b) and Fig. 4.7(a)-(c) show SEM images of ZnO:Sb thin films grown on different substrates. Fig. 4.6 (a)-(b) show the SEM images of ZnO:Sb thin film sample C grown on Si (100) substrate and ZnO:Sb thin film sample D grown on Si (111), respectively. Fig. 4.7(a)-(c) show the SEM images of ZnO:Sb thin film sample E grown on $SiO_2$ substrate, (b) ZnO:Sb thin film sample F grown on *r*-plane sapphire substrate,

and (c) ZnO:Sb thin film sample G grown on *c*-plane sapphire substrate. The substrate, carrier type, and concentration in these ZnO:Sb thin film samples were summarized in Table 4.1. I want to emphasize that a bunch of ZnO:Sb thin films grown on different substrates have been studied and characterized, here only one typical sample from each kind of substrates is shown for discussion.

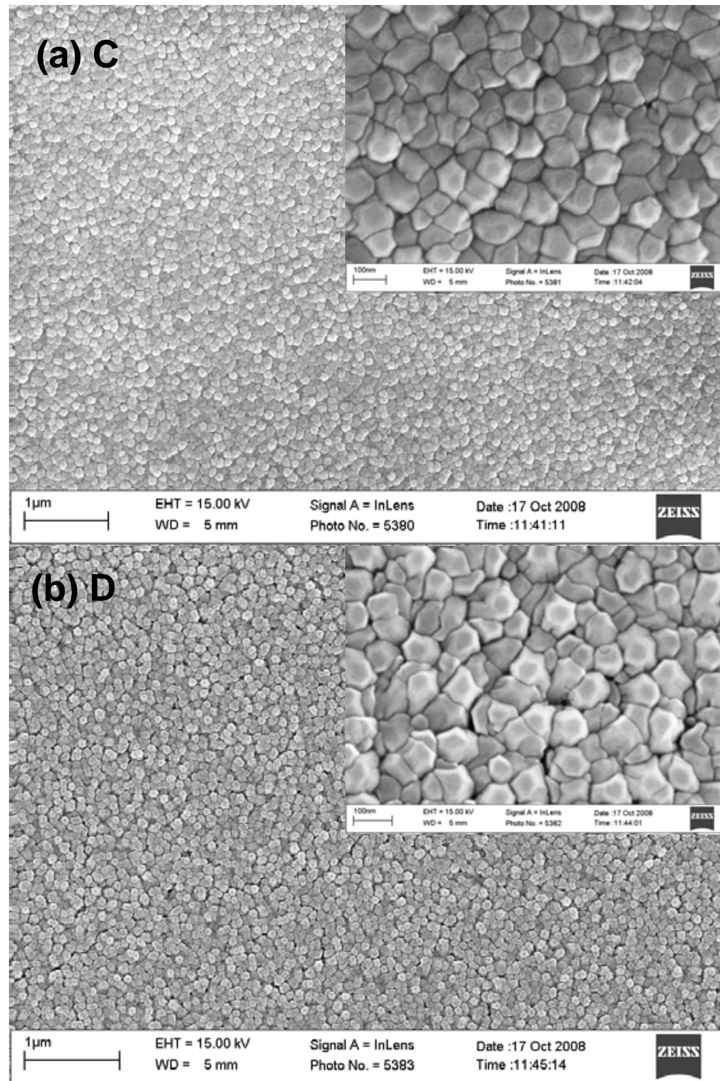


FIG. 4.6 SEM images of (a) ZnO:Sb thin film sample C grown on Si (100) substrate and (b) ZnO:Sb thin film sample D grown on Si (111).

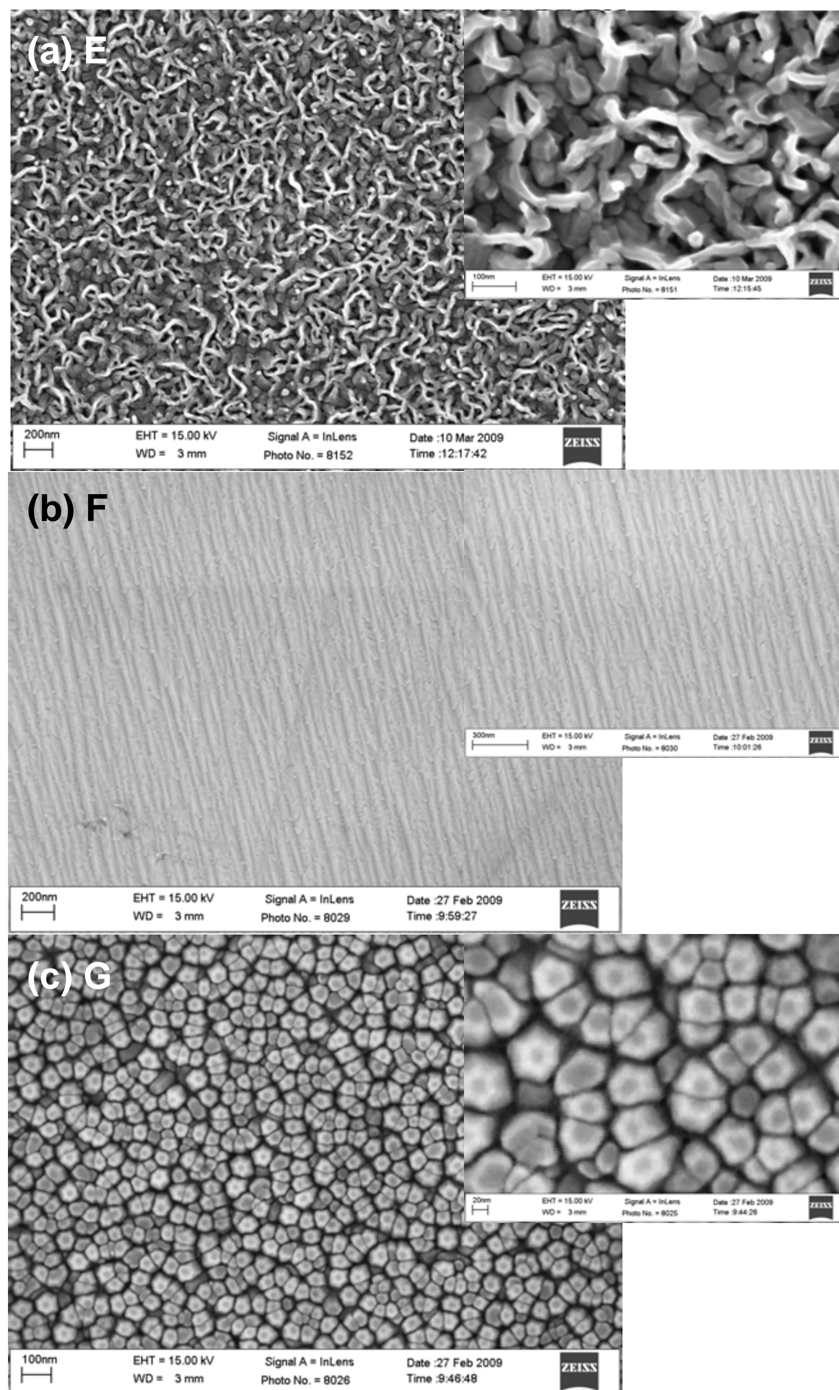


FIG. 4.7 SEM images of (a) ZnO:Sb thin film sample E grown on $SiO_2$ substrate, (b) ZnO:Sb thin film sample F grown on *r*-plane sapphire substrate, and (c) ZnO:Sb thin film

sample G grown on *c*-plane sapphire substrate.

It is observed that the ZnO:Sb thin films grown on either Si (100) or Si (111) substrates show a closely-packed nano-columnar structures [Fig. 4.6(a) and (b)], where reliable *p*-type can be achieved. Furthermore, dominate UV NBE EL emissions[27] and random lasing effect[28] have also been observed in *p*-type ZnO:Sb thin film samples with these closely-packed nano-columnar structures. When ZnO:Sb thin film is grown on $SiO_2$ substrates, the ZnO:Sb thin films shown extremely polycrystalline behavior [Fig. 4.7(a)]. Only *n*-type films can be achieved based on studies of many samples. This is reasonable because the undoped ZnO grown on $SiO_2$ substrate generally shows a background electron carrier concentration above $10^{19}$ $cm^{-3}$, which is too high for any kind of external introduced acceptor to overcome. On the contrary, when ZnO:Sb thin film is grown on *r*-sapphire substrates, relatively smooth continuous films are achieved, but, again no *p*-type films have been achieved based on extensive studies. When the ZnO:Sb thin film is grown on *c*-sapphire, the film morphology is in between Si and *r*-sapphire. Accordingly, the doping behavior is also in between Si and *r*-sapphire. *p*-type behavior was once achieved in the as-grown ZnO:Sb thin films on *c*-sapphire for a short while. However, after some time, this ZnO:Sb thin film converted from *p*-type to *n*-type. Fig. 4.8(a)-(d) shows the time-evolution of the carrier type and concentration in ZnO:Sb thin film sample G grown on *c*-plane. Initially, it was *p*-type with a hole concentration of 1.5 ×

$10^{17}$ $cm^{-3}$[Fig. 4.8(a)]. After one month passed, it changed to *n*-type with an electron concentration of 5.8 × $10^{16}$ $cm^{-3}$ [Fig. 4.8(b)]. With time passing by, the electron concentration kept increasing as shown in Fig. 4.8(c) and (d), until it reached near saturation.

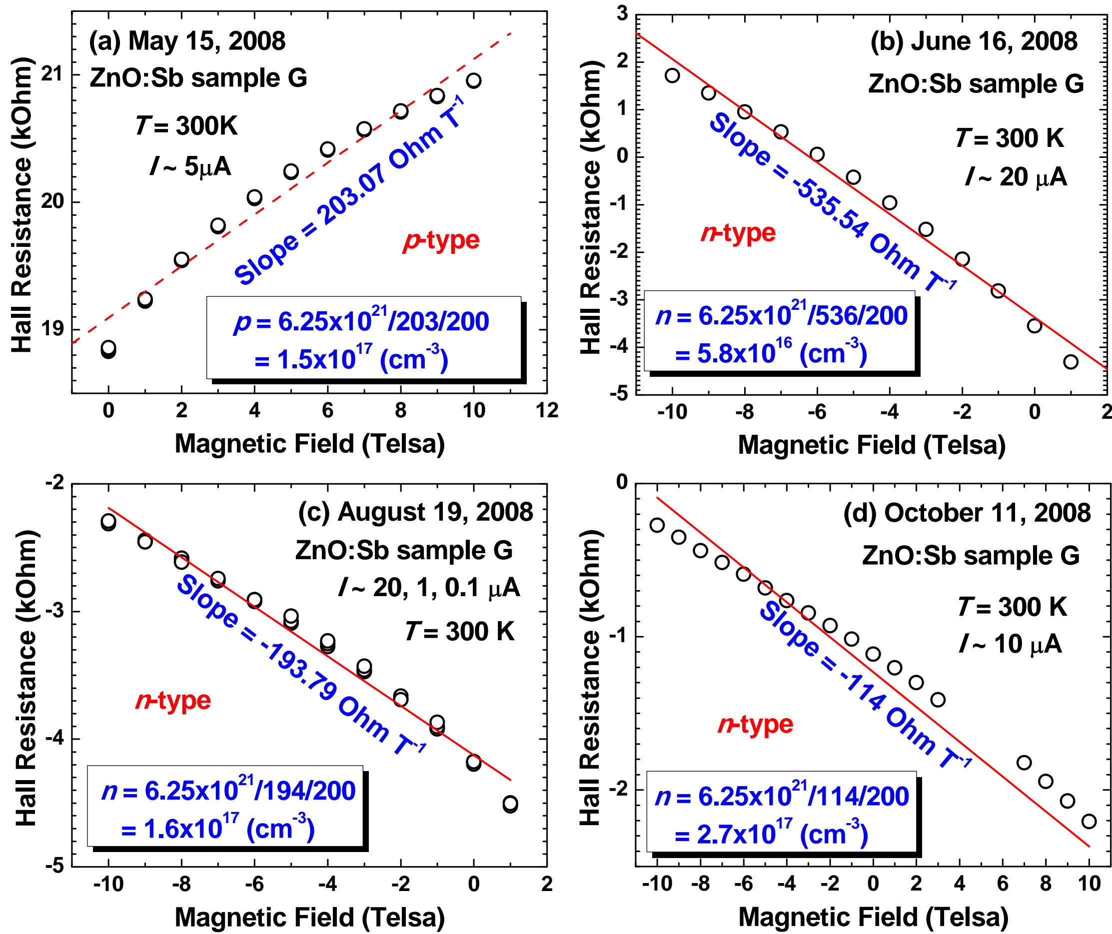


FIG. 4.8 Time-evolution of the carrier type and concentrations in ZnO:Sb sample G.

Based on the above presented experiment results and a huge amount of other un-presented results, it is found that p-type is more easily achieved in ZnO:Sb with grains

(such as closed-packed nano-columns morphology for ZnO:Sb grown on Si), than ZnO:Sb films This is possibly because $V_{Zn}$-related acceptor complex is more easily interfacially forming at grain boundaries (such as the side walls of the nano-columns) in ZnO.[32] The morphology with large surface areas from grain boundaries facilitate the p-type doping in ZnO samples. It is hard for strictly two-dimensional film to provide enough grain boundary surfaces to form interfacial $V_{Zn}$-related acceptor complex. ZnO:Sb materials with closely-packed nanocolumns morphology is promising for p-type. This is not only supported by materials studies (e. g. Hall effect measurements), but also by the recently demonstrated room-temperature UV-emission-dominated LED[27] and random lasing devices[28], which have the closely-packed nano-columnar ZnO:Sb layers as incorporated.

### 4.4 Summary

Structural, optical properties, and doping mechanism of Sb doped *p*-type ZnO on Si (100) and Si (111) were comprehensively studied. Crystallinity and strain in both *c* and *a* plane were studied by XRD $\theta$-$2\theta$ scan and in-plane GI XRD. XPS measurements show that Sb dopants were incorporated into the *p*-type ZnO films with a positive charge, implying that Sb substitutes for Zn and bonds with O. Various-temperature PL measurements reveal that heavy Sb doping can trigger the formation of Zn vacancies,

raising a broad emission around ~3.0 eV. Combing with the theoretical calculation, which suggest that the $Sb_{Zn}$-$2V_{Zn}$ is a shallow acceptor and with low formation energy under oxygen rich condition, although $Sb_{Zn}$ itself is a donor in ZnO, the formation of a $Sb_{Zn}$ and $V_{Zn}$ complex is believed to be the origin of shallow acceptors in this system. It is found that the possibility of achieving *p*-type ZnO:Sb is also closely related to the thin film morphology. ZnO:Sb grown on Si substrates with closely-packed nano-columnar structures facilitates the achievement of reliable *p*-type doing, because $V_{Zn}$-related acceptor complex is more easily forming interfacially at grain boundaries in ZnO and the morphology with large grain boundary surface areas, such as the side walls of the nano-columns, facilitates the p-type doping in ZnO samples.

## 4.5 Acknowledgement

This work was supported by ONR/DMEA through the Center of Nanomateials and Nanodevice(CNN) under the grant No. H94003-08-2-0803. ZY would like to thank Prof. W. P. Beyermann for his PPMS equipment and Prof. S. Limpijumnong's contributions on Fig. 4.5.

## References


[1] D. C. Look, J. W. Hemsky, and J. R. Sizelove, Phys. Rev. Lett. **82**, 2552 (1999).

[2] D. C. Look, G. C. Farlow, P. Reunchan, S. Limpijumnong, S. B. Zhang, and K. Nordlund, Phys. Rev. Lett. **95**, 225502 (2005).

[3] C. G. Van de Walle, Phys. Rev. Lett. **85**, 1012 (2000).

[4] S. Zh. Karazhanov, E. S. Marstein, and A. Holt, J. Appl. Phys. **105**, 033712 (2009).

[5] S. B. Zhang, S. –H. Wei, and A. Zunger, Phys. Rev. B **63**, 075205 (2001).

[6] D. C. Look and B. Claflin, Phys. Stat. Sol. (b) **241**, 624 (2004).

[7] D. C. Look, D. C. Reynolds, C. W. Litton, R. L. Jones, D. B. Eason, G. Cantwell, Appl. Phys. Lett. **81**, 1830 (2002).

[8] A. Tsukazaki, A. Ohtomo, T. Onuma, M. Ohtani, T. Makino, M. Sumiya, K. Ohtani, S. F. Chichibu, S. Fuke, Y. Segawa, H. Ohno, H. Koinuma, and M. Kawasaki, Nat. Mater. 4, 42 (2005).

[9] Y. R. Ryu, S. Zhu, D. C. Look, J. M. Wrobel, H. M. Jeong, and H. W. White, J. Crystal Growth **216**, 330 (2000).

[10] Y. R. Ryu, T. S. Lee, J. A. Lubguban, H. W. White, B. J. Kim, Y. S. Park, C. J. Youn, Appl. Phys. Lett. **88**, 241108 (2006).

[11] F. X. Xiu, Z. Yang, L. J. Mandalapu, and J. L. Liu, Appl. Phys. Lett. **88**, 152116 (2006).

[12] F. X. Xiu, Z. Yang, L. J. Mandalapu, J. L. Liu, and W. P. Beyermann, Appl. Phys. Lett. **88**, 052106 (2006).

[13] K. K. Kim, H. S. Kim, D. K. Hwang, J. H. Lim, and S. J. Park, Appl. Phys. Lett. 83, 63 (2003).

[14] J. H. Lim, C. K. Kang, K. K. Kim, I. K. Park, D. K. Hwang, and S. J. Park, Adv. Mater. **18**, 2720 (2006).

[15] S. Limpijumnong, S. B. Zhang, S. H. Wei, C. H. Park, Phys. Rev. Lett. **92**, 155504 (2004).

[16] T. Aoki, Y. Shimizu, A. Miyake, A. Nakamura, Y. Nakanishi, and Y. Hatanaka, Phys. Stat. Sol. (b) **229**, 911 (2002).

[17] F. X. Xiu, Z. Yang, L. J. Mandalapu, D. T. Zhao, J. L. Liu, and W. P. Beyermann, Appl. Phys. Lett. **87**, 152101 (2005).

[18] F. X. Xiu, Z. Yang, L. J. Mandalapu, D. T. Zhao, and J. L. Liu, Appl. Phys. Lett. **87**, 252102 (2005); Y. J. Zeng and Z. Z. Ye, Appl. Phys. Lett. **90**, 116102 (2007); and F. X. Xiu and J. L. Liu, Appl. Phys. Lett. **90**, 116103 (2007).

[19] W. Guo, A. Allenic, Y. B. Chen, X. Q. Pan, Y. Che, Z. D. Hu, and B. Liu, Appl. Phys. Lett. **90**, 242108 (2007).

[20] P. Wang, N. Chen, Z. Yin, R. Dai, and Y. Bai, Appl. Phys. Lett. **89**, 202102 (2006).

[21] L. J. Mandalapu, F. X. Xiu, Z. Yang, J. L. Liu, J. Appl. Phys. **102**, 023716 (2007).

[22] L. J. Mandalapu, Z. Yang, and J. L. Liu, Appl. Phys. Lett. **90**, 252103 (2007); and L. J. Mandalapu, Z. Yang, and J. L. Liu, Appl. Phys. Lett. **91**, 149903 (2007).

[23] L. J. Mandalapu, F. X. Xiu, Z. Yang, D. T. Zhao, and J. L. Liu, Appl. Phys. Lett. **88**, 112108 (2006); Y. J. Lin, P. H. Wu, and D. S. Liu, Appl. Phys. Lett. **91**, 136101 (2007); and L. J. Mandalapu and J. L. Liu, Appl. Phys. Lett. **91**, 136102 (2007).

[24] L. J. Mandalapu, Z. Yang, F. X. Xiu, D. T. Zhao, and J. L. Liu, Appl. Phys. Lett. **88**, 092103 (2006).

[25] L. J. Mandalapu, Z. Yang, S. Chu, and J. L. Liu, Appl. Phys. Lett. **92**, 122101 (2008).

[26] S. Chu, J. H. Lim, L. J. Mandalapu, Z. Yang, L. Li, and J. L. Liu, Appl. Phys. Lett. **92**,152103 (2008).

[27] J. Kong, S. Chu, M. Olmedo, L. Li, Z. Yang, and J. L. Liu, Appl. Phys. Lett. **93**, 132113 (2008).

[28] S. Chu, M. Olmedo, Z. Yang, J. Kong, J. L. Liu, Appl. Phys. Lett. **93**, 181106 (2008).

[29] Ü. Özgür, Ya. I. Alivov, C. Liu, A. Teke, M. A. Reshchikov, S. Doğan, V. Avrutin, S.-J. Cho, and H. Morkoç, J. Appl. Phys. **98**, 041301 (2005).

[30] J. M. Yuk, J. Y. Lee, J. H. Jung, T. W. Kim, D. I. Son, and W. K. Choi, Appl. Phys. Lett. 90 031907 (2007)

[31] M. N. Islam, T. B. Ghosh, K.L. Chopra, H. N. Acharya, Thin Solid Films **280**, 20 (1996).

[32] J. M. Carlsson, H. S. Dormingos, P. D. Bristowe, and B. Hellsing, Phys. Rev. Lett. **91**, 165506 (2003).

# 5. Chapter 5 Cobalt Doping in Zinc Oxide

## 5.1 Introduction

### 5.1.1 Diluted magnetic semiconductors

Diluted magnetic semiconductor (DMS)[1] materials have been widely studied because of their potential applications in spintronics.[2-7] In the last two decades, rapid and outstanding progress was achieved in several group II-VI and III-V DMS materials, such as Mn-doped ZnSe,[1, 3] GaAs,[2, 4] and InAs.[5-6] The origin and mechanism of ferromagnetism in these DMS materials have been well studied and are believed to be free-carrier mediated exchange between magnetic ions. However, the Curie temperatures ($T_c$) of these DMS materials are all far below the room temperature, which hinders their applications in commercial products.

### 5.1.2 Zinc oxide diluted magnetic semiconductors

In recent years, magnetically doped ZnO has emerged as a possible DMS material,[8-9] because theoretical calculations have predicted an above room-temperature $T_c$.[10-11] However, experimental results on ZnO-based materials are still controversial.[8, 12-25] In addition to ferromagnetism,[12-20] non-ferromagnetic states,[21-25] such as spin-glass,[21] antiferromagnetism,[22] and paramagnetism,[23] have also been reported. Furthermore, the origin of the ferromagnetism in ZnO-based DMS materials is still controversial, unlike

the DMS materials mentioned above such as GaAs:Mn. Some researchers reported clustering or secondary phase formation as the origin of the ferromagnetism (i.e. an extrinsic mechanism),[26-28] while others concluded that an intrinsic carrier-mediated mechanism was responsible for the ferromagnetism.[29-31] In order to experimentally investigate and prove the presence of intrinsic carrier- mediated ferromagnetism in ZnO, some advanced experiments have been recently designed. For example, studies on ZnO codoped with a transition metal and either a donor or acceptor dopant, such as Zn interstitials,[32-35] Al,[36-39] and Ga[40] for *n*-type conduction and N,[41-44] P,[45-46] and As[47-48] for *p*-type conduction, have been pursued to check the role of the free carriers in the ferromagnetism in ZnO-based DMS materials. Furthermore, electrical transport and optical probes beyond the more common techniques for studying magnetism (e.g., bulk magnetization), such as anomalous Hall effect (AHE)[49-53] and magnetic circular dichroism,[7] were performed on ZnO-based DMS materials to help distinguish between intrinsic and extrinsic mechanisms of ferromagnetism. In this chaper, we report results on the free electron carrier concentration dependence of the magnetization, AHE, magnetoresistance, magnetic anisotropy, and transmission electron microscopy (TEM) studies on ZnO:Co thin films. These experimental data provide strong evidence in support of intrinsic carrier-mediated ferromagnetism in ZnO DMS materials.

## 5.2 Experiment

### 5.2.1 Sample preparation

#### 5.2.1.1 Epitaxy growth

The ZnO and ZnO:Ga thin films were grown on *r*-cut sapphire substrates using plasma-assisted molecular-beam epitaxy (MBE). Regular effusion cells filled with elemental Zn (6N) and Ga (6N) were used as zinc and gallium sources. Radiofrequency plasma supplied with $O_2$ (5N) was used as the oxygen source. The electron carrier concentration of the ZnO:Ga thin films was tuned by the amount of Ga incorporation, which was controlled by the Ga effusion cell temperature. The substrate temperature was kept at 565 ˚C during the growth. After growth, the samples were annealed *in situ* in vacuum at 800 ˚C for 20 min to activate the Ga dopants and improve crystallinity. The electron carrier concentration values of these ZnO and ZnO:Ga samples are shown in Table 5.1 as "before implantation" carrier concentration $n_0$. More detailed growth procedures can be found elsewhere.[54]

Table 5.1 Electron carrier concentration before and after implantation and the saturated magnetization of ZnO:Co thin film samples. The data were taken at room temperature.

| Sample No. | Electron concentration before implantation $n_0$ ($cm^{-3}$) | Electron concentration after implantation $n$ ($10^{19}$ $cm^{-3}$) | Saturated Magnetization $M_S$ ($\mu_B$ per Co ion) |
|---|---|---|---|
| A | $1.2 \times 10^{20}$ | $8.3 \times 10^{19}$ | 4.6 |
| B | $3.4 \times 10^{19}$ | $3.6 \times 10^{19}$ | 4.1 |
| C | $8.4 \times 10^{18}$ | $4.0 \times 10^{18}$ | 1.4 |
| D | $3.5 \times 10^{18}$ | $1.3 \times 10^{18}$ | 0.3 |
| E | $4.7 \times 10^{19}$ | $2.8 \times 10^{19}$ | 4.1 |

Note: $\mu_B$ stands for the Bohr magneton.

#### 5.2.1.2 Ion implantation

The Co ions were implanted into as-grown ZnO and ZnO:Ga thin films with a dose of $3\times10^{16}$ $cm^{-2}$ and an implantation energy of 50 keV. The total amount of Co ions implanted in each ZnO film was calculated by the dose and area of the sample. All Co-implanted ZnO samples were annealed at 900 ˚C for 5 min in nitrogen after implantation to activate the implanted Co ions and recover the crystallinity. (In the context of this chapter, both ZnO and ZnO:Ga thin films are referred to ZnO samples for

convenience, since Ga doping is only used to tune the electron carrier concentration of the ZnO thin films, and ZnO: Co represent samples implanted with Co ions and annealed using the above mentioned procedure. All the experiments, such as magnetic and transport properties measurements, were performed on the annealed samples.) The electron carrier concentrations of the ZnO:Co samples were shown in Table 5.1 as “after implantation” carrier concentration *n*.

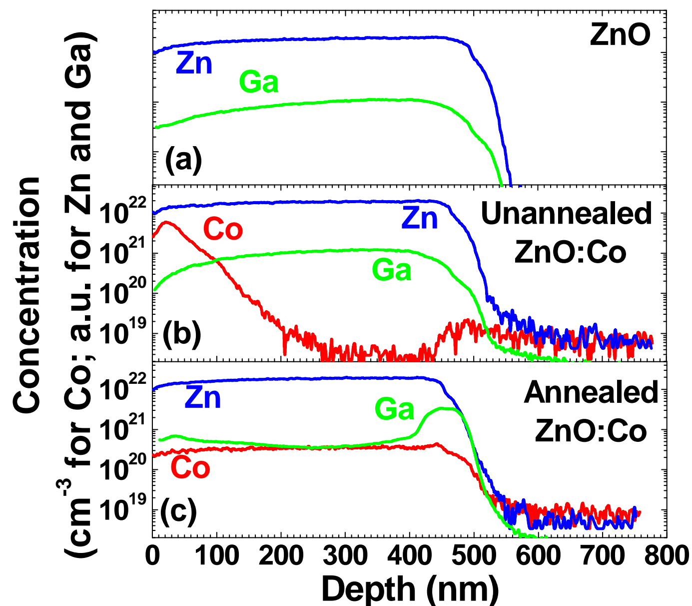


FIG. 5.1 SIMS spectra for (a) the as-grown ZnO thin film, (b) the ZnO:Co thin film after Co ion implantation, but before annealing, and (c) the ZnO:Co thin film after annealing at 900 ˚C for 5 minutes (sample A). The magnetic measurements were all performed on the annealed samples.

Figure 5.1 shows secondary ion mass spectroscopy (SIMS) spectra of (a) the ZnO

thin film before Co ion implantation, (b) the ZnO:Co thin film immediately after the implantation but before annealing, and (c) the ZnO:Co thin film after implantation and annealing at 900 ˚C for 5 min. As shown in Fig. 5.1(a), the Zn and Ga distributions are fairly uniform throughout the depth of the ZnO film. After Co implantation, the implanted Co ion concentration follows a Gaussian distribution with a peak near the surface of the ZnO:Co thin film as shown in Fig. 5.1(b). The fact that the Gaussian peak is near the surface is an intentional result of a low implantation energy intended to prevent a significant amount of Co ions from reaching the sapphire substrate. After annealing at 900 ˚C for 5 min, the Co ions redistribute to a relatively uniform profile along the depth of the ZnO:Co film as shown in Fig. 5.1(c). Ga atoms are piling near the ZnO/sapphire interface shown in Fig.1(c), which is possibly due to the migration of the Ga atoms after high temperature annealing. Although most of the Co ions are in the ZnO film layer, a tiny amount of residual Co ions may have reached the sapphire substrate region for both unannealed and annealed samples; however, their concentrations are more than one order of magnitude smaller than the Co ion concentrations in the ZnO films. Any magnetic contribution from the substrates was removed from the magnetization data with the following procedure. We first measured the ZnO:Co thin film on the sapphire substrate. Then we completely etched away the ZnO:Co layer using diluted hydrochloric acid and measured just the sapphire substrate. The magnetic response of the ZnO:Co thin

films was obtained by subtracting the two data sets. The magnetization data of the ZnO:Co thin films discussed in this paper were all followed this procedure.

### 5.2.2 Characterizations

TEM studies were carried out on a JEOL JEM 3011 high resolution electron microscope operated at 300 kV, with a point-to-point resolution of 0.17 nm. Cross-sectional TEM specimens were prepared via mechanical grinding, polishing, and dimpling, followed by argon ion milling in a Gatan Model 691 Precision Ion Polishing System at incident angles between 4 and 5.5° to electron transparency. X-ray diffraction (XRD) measurements were performed using a Bruker D8 Advance x-ray diffractometer. Magnetic properties were measured with a Quantum Design MPMS-XL superconducting quantum interference device (SQUID) magnetometer using an in-plane geometry (magnetic field parallel to the film) on all samples unless specified differently. Magnetoresistance and field-dependent Hall effect measurements were performed with Hall bar geometry using a Quantum Design PPMS equipment. The magnetic field was perpendicular to the film plane of the samples in the magnetoresistance measurements. In addition to field-dependent Hall effect measurements, the ordinary Hall effect measurements were also carried out separately with Van der Pauw geometry using an Ecopia HMS-3000 room-temperature Hall effect system at constant magnetic field of 1 T

to get the electron carrier concentration of the samples. SIMS measurements were performed using a PHI ADEPT-1010 Dynamic SIMS system.

## 5.3 Results and discussions

### 5.3.1 Structural properties

Figure 5.2(a) shows a cross-sectional TEM image of a typical ZnO:Co thin film on an *r*-cut sapphire substrate (sample A). The TEM image shows a relatively low dislocation density, indicating a high quality film.

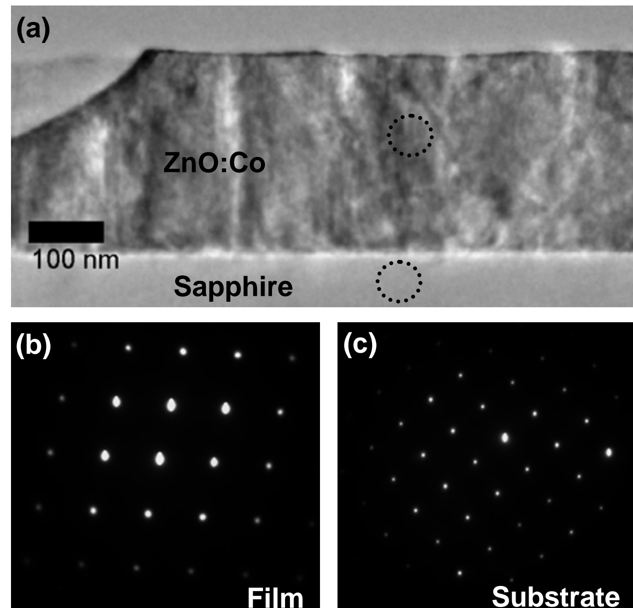


FIG. 5.2 (a) Cross-sectional TEM image of a ZnO:Co thin film on a sapphire substrate (sample A). SAED patterns of (b) ZnO:Co thin film and (c) sapphire substrate, taken from the areas indicated by the dotted circles.

Selected area electron diffraction (SAED) patterns from the areas indicated by the dotted circles in Fig. 5.2(a) are shown in Fig. 5.2(b) for the ZnO:Co thin film and in Fig. 5.2(c) for the sapphire substrate. Similar SAED patterns were observed from various different positions along the film. These diffraction patterns are symmetric and uniform, indicating the absence of clustering and secondary phase formation.

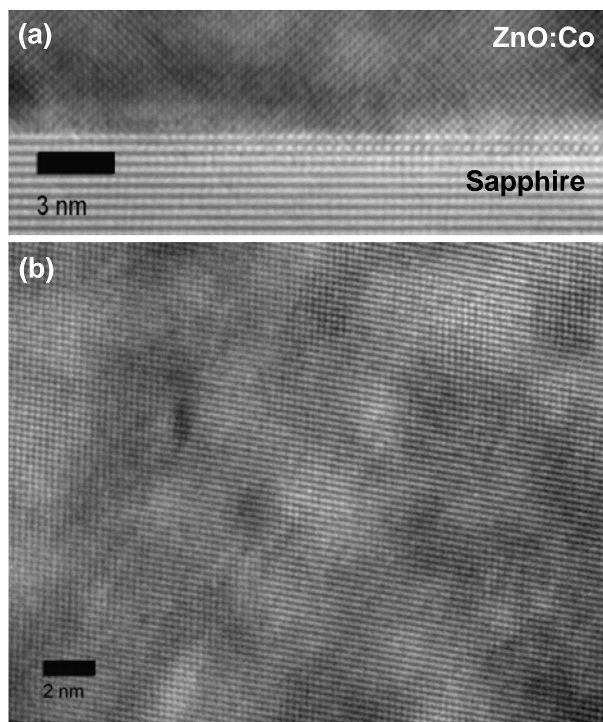


FIG. 5.3. (a) Cross-sectional HRTEM image of the interface between the ZnO:Co thin film and the sapphire substrate in sample A, showing an atomically sharp interface. (b) HRTEM image of the ZnO:Co thin film (sample A). The film has high crystallinity with no observable secondary phase.

Figures 5.3(a) and 5.3(b) show typical high resolution TEM (HRTEM) images of the film/substrate interface and the film itself, respectively. The zone axes of the film and the substrate is approximately 3˚ apart from each other, indicating a slight twist between the film and the substrate. The crystallographic alignment of the ZnO:Co layer with the sapphire substrate at the interface is good. HRTEM studies indicate that the film is of high crystallinity, and no clustering or secondary phases were observed; however, a small number of stacking faults were observed.

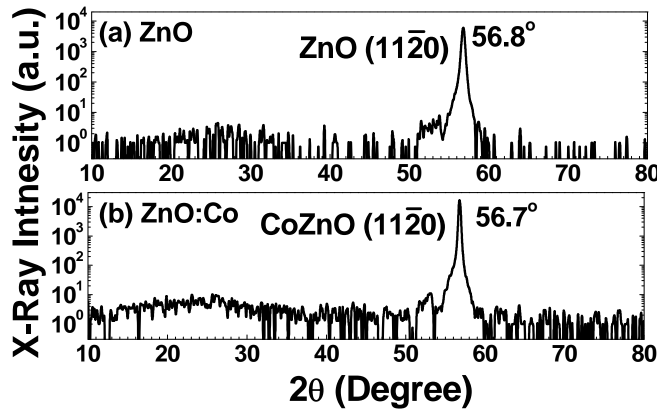


FIG. 5.4. XRD spectra of (a) ZnO and (b) ZnO:Co thin films (sample A). Both the ZnO and ZnO:Co thin films show high crystallinity with no impurity phases within the detection limit of the system.

Figures 5.4(a) and 5.4(b) show XRD patterns of typical ZnO and ZnO:Co thin films (sample A). The only ZnO $(11\bar{2}0)$ peak, which was observed at approximately 56.8˚, did not show any significant change after Co-implantation, indicating the

Co-implantation did not significantly degrade the sample's crystallinity. Furthermore, no Co-related impurity phase or compound peaks were detected in the XRD pattern in Fig. 5.4(b) within the detection limit of the system.

### 5.3.2 Magnetic properties

Figure 5.5(a) shows the magnetic field dependence of the magnetization (*M-H*) of a ZnO:Co thin film (sample A) at a temperature of 300 K. The *M-H* curve measured at 10 K is shown in the inset. The saturated magnetization $M_S$ value is approximately 4.6 $\mu_B$ per Co ion, which is larger than most of previously reported values, [31-32, 37, 39, 41, 55-57] but it is smaller than the giant magnetic moments observed in ZnO:Co (6.1 and 18.9 $\mu_B$ per Co)[58-59] and $SnO_2$:Co thin films (7.5±0.5 $\mu_B$ per Co).[60] For metallic Co, the saturated magnetization is around 1.7 $\mu_B$ per Co, a consequence of band ferromagnetism. The value we measured for this ZnO:Co thin film is midway between that calculated for isolated divalent Co ions with full angular momentum (i.e., $gJ=6\mu_B$) and that calculated with the orbital angular momentum quenched (i.e., $2S=3\mu_B$), suggesting that the ferromagnetism of the samples is not from the metallic Co clusters. This is consistent with the HRTEM analyses and XRD data.

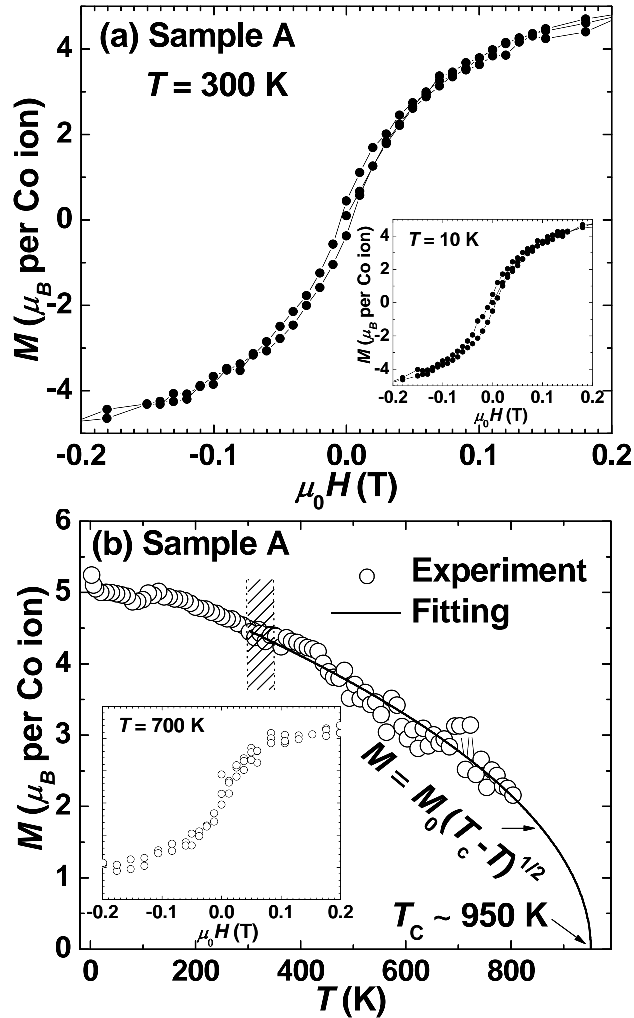


FIG. 5.5. (a) The magnetic field dependence of the magnetization for a ZnO:Co thin film (sample A) measured at 300 K and 10 K (inset). (b) The temperature dependence of the saturated magnetization, from 2 to 800 K measured with an applied field of 0.2 T. A high-temperature extrapolation of the data indicates that the Curie temperature is around 950 K. The inst shows the field dependence of the magnetization of this sample measured at 700K.

The temperature dependence of the magnetization, measured with a magnetic field of 0.2 T, of the ZnO:Co thin film (sample A) is shown in Fig. 5.5(b). The standard

sample insert was used to measure the magnetization from 2 K to 350 K, while an oven insert with a brass sample holder was used for the measurements from 300 K to 800 K. A more restricted sample enclosure resulted in noisier data at high temperature. The Curie temperature is above the upper-temperature limit of the system (800 K). Using the approximate relation $M = M_0(T_C - T)^{1/2}$, the data were extrapolated to obtain an estimate for the Curie temperature of ~950 K. The field dependence of the magnetization of this sample measured at 700 K is shown in the inset of Fig. 5.5(b).

Table 5.2 The resistivity $\rho_{xx}$, ordinary Hall coefficient $R_0$, anomalous Hall coefficient $R_S$, electron carrier concentration $n$, and the ratio $\rho_{AHE}/\rho_{xx}$ for ZnO:Co thin film sample E. Data were measured at the temperatures of 10 K, 50 K, and 300 K.

| $T$ (K) | $\rho_{xx}$ ($10^{-3}$ Ω cm) | $R_0$ ($10^{-5}$ Ω cm $T^{-1}$) | $R_S$ ($10^{-4}$ Ω cm $T^{-1}$) | $n$ ($10^{19}$ $cm^{-3}$) | $\rho_{AHE}/\rho_{xx}$ ($10^{-5}$) |
|---|---|---|---|---|---|
| 10 | 8.62 | -2.40 | 6.3 ± 0.6 | 2.6 | 17 ± 2 |
| 50 | 8.49 | -2.35 | 3.4 ± 0.1 | 2.7 | 9.2 ± 0.2 |
| 300 | 8.33 | -2.26 | 1.5 ± 0.1 | 2.8 | 4.1 ± 0.2 |

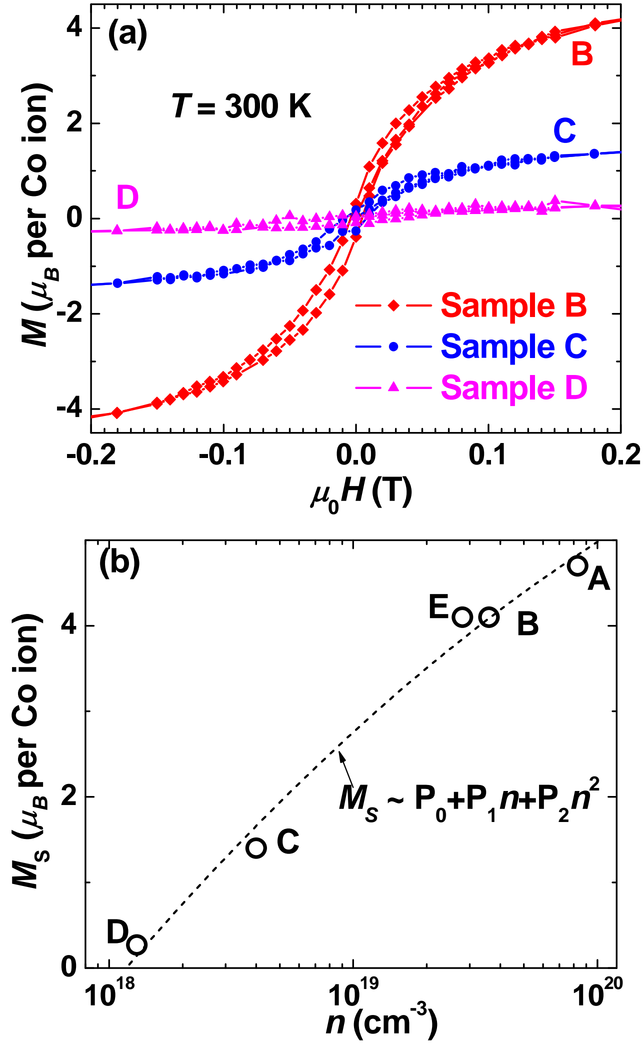


FIG. 5.6. (a) The magnetic field dependence of the magnetization for ZnO:Co thin film samples B, C, and D measured at a temperature of 300 K. (b) The dependence of the saturated magnetization $M_S$ on electron carrier concentration $n$ in ZnO:Co thin film samples. A polynomial fitting to the data is indicated with the dashed line.

ZnO:Co thin film samples with different electron carrier concentrations, ranging from $1.3\times10^{18}$ to $8.3\times10^{19}$ $cm^{-3}$, were prepared to investigate the carrier concentration

dependence of magnetization. Figure 5.6(a) shows the ferromagnetic hysteresis loops for ZnO:Co thin films B, C, and D measured at 300 K. The saturated magnetization of sample B (4.1 $\mu_B$ per Co) is slightly smaller than sample A (4.6 $\mu_B$ per Co) in Figure 5.5(a). However, when the electron carrier concentration decreases below ~$10^{19}$ cm$^{-3}$ as in samples C and D, the saturated magnetizations drop dramatically to 1.4 and 0.3 $\mu_B$ per Co, respectively. The carrier concentrations, measured both before and after Co ion implantation, and the saturated magnetization are listed in Table 5.1 for these ZnO:Co thin film samples. Figure 5.6(b) shows the experimental relation between the saturated magnetization ($M_S$) and the free electron carrier concentration ($n$) measured after Co ion implantation in samples A-E. A polynomial fit (dashed line) to the experimental data (open circles) provides a guide to the eye, although the physical meaning behind this trend needs further clarification.

Figure 5.7 shows the anisotropic magnetization for ZnO:Co thin film sample E. The out-of-plane (magnetic field perpendicular to the film plane) and in-plane (magnetic field parallel to the film plane) field dependences of the magnetization are shown with open and solid circles in Fig. 5.7, respectively. The out-of-plane curve shows a weaker magnetization before saturation than the in-plane geometry. The ZnO thin films were epitaxially grown on *r*-cut sapphire substrates with the growth direction along the $[11\bar{2}0]$ direction as indicated by the XRD pattern (Fig. 5.4b). This result indicates that the easy

magnetization axis is in the plane of the film, which is consistent with similar magnetic anisotropy experiments on ZnO:Co thin films reported by other groups.[57] Magnetic anisotropy is further evidence for an intrinsic nature of the ferromagnetism in ZnO:Co DMS thin films[56-57] since the cluster-related ferromagnetism is generally isotropic.

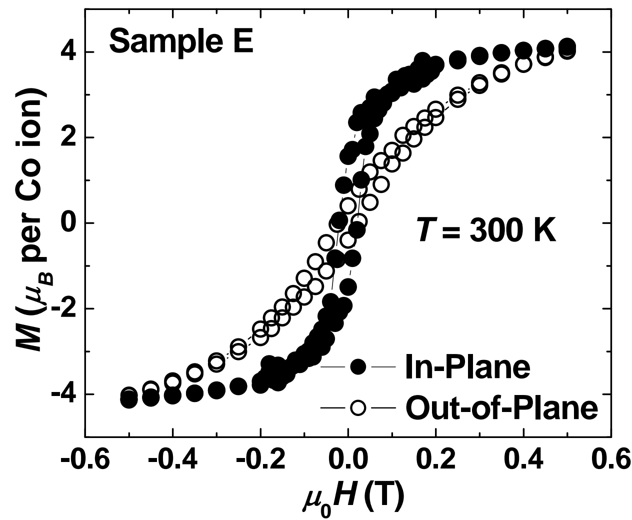


FIG. 5.7. Magnetic anisotropy of a ZnO:Co thin film (sample E) measured at a temperature of 300 K. The in-plane field dependence of the magnetization (solid circles) are stronger than out-of-plane magnetization (open circles).

### 5.3.3 Transport properties

Figure 5.8(a) shows the transverse magnetoresistance, MR=[$R(H)$-$R(0)$]/$R(0)$, for ZnO:Co thin film sample E measured at the temperatures of 2, 5, 8, 10, 20, 50, and 300 K. The magnetoresistance, which measured up to 10 T, in our ZnO:Co thin film is strongly

temperature dependent with a positive magnitude from 2 to 5 K and a negative magnitude above 20 K. Between 5 K and 20 K, the MR starts out negative and eventually swings positive at higher fields, reflecting competing contributions.

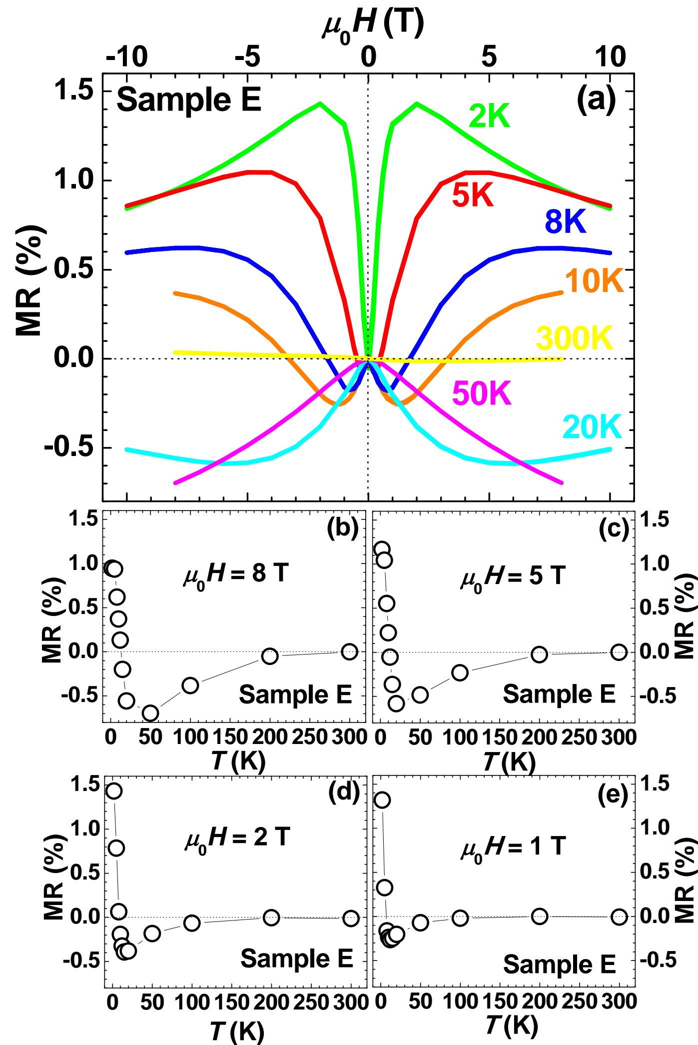


FIG. 5.8. (a) Transverse magnetoresistance, MR=[R(H)-R(0)]/R(0), of a ZnO:Co thin film (sample E) measured at different temperatures from 2 to 300 K. The applied magnetic field was perpendicular to the plane of the film. (b)-(e) The temperature dependence of the magnetoresistance at different magnetic fields of 8, 5, 2, and 1 T.

A positive MR is attributed to a giant spin splitting of band states caused by a *sp-d* exchange interaction in DMSs.[61-63] A negative MR is from the third-order *sp-d* exchange Hamiltonian of the spin scattering,[64-66] because the second-order theory breaks down at large magnetic fields.[66] Figure 5.8(b)-(e) show the temperature dependence of the magnetoresistance at different magnetic fields of 8, 5, 2, and 1 T, respectively. Furthermore, the MR properties of our ZnO:Co thin films also show carrier-concentration-dependent behavior, in addition to a temperature dependence.[67] We believe the temperature and free carrier concentration dependences of the magnetoresistance are also a sign of intrinsic carrier mediated ferromagnetism.

Figure 5.9(a) shows the Hall resistance $R_{\mathrm{Hall}}$ as a function of magnetic field for ZnO:Co thin film sample E, measured at a temperature of 50 K. The Hall effect data, measured at 10 K and 300 K, are shown in Fig. 5.9(b) and 5.9(c). The Hall resistance is the sum of two contributions: the ordinary Hall effect (OHE) from the classical Lorenz force and the anomalous Hall effect (AHE) due to an asymmetric scattering in the presence of a magnetization. This is expressed by the equation,

$$R_{\mathrm{Hall}} = \frac{R_0}{d}(\mu_0 H) + \frac{R_{\mathrm{S}}}{d}(\mu_0 M) \equiv R_{\mathrm{OHE}} + R_{\mathrm{AHE}} \qquad (5\text{-}1)$$

where the $R_{\mathrm{OHE}}$ and $R_0$ are the ordinary Hall resistance and coefficient, $R_{\mathrm{AHE}}$ and $R_{\mathrm{S}}$ are the anomalous Hall resistance and coefficient, and $d$ is the film thickness. $H$ and $M$ are

the magnetic field and the magnetization perpendicular to the film plane, and $\mu_0$ is the free space permeability, respectively.

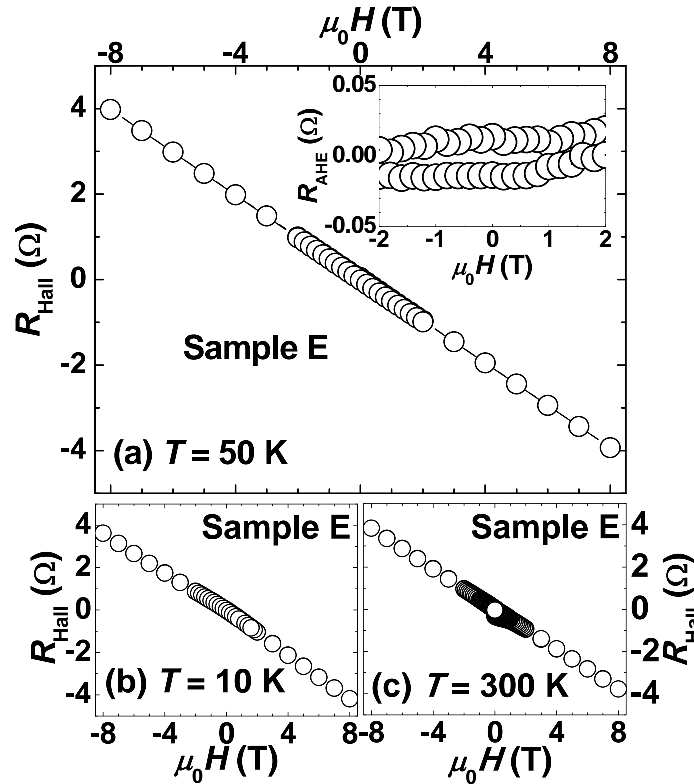


FIG. 5.9. (a) The Hall resistance as a function of the applied magnetic field for a ZnO:Co thin film (sample E) measured at a temperature of 50 K. The inset shows the AHE data over an expended field range near the origin after the linear OHE contribution was subtracted. (b)-(c) The Hall resistance as a function of the applied magnetic field for the same ZnO:Co thin film sample measured at the temperatures of 10 K and 300 K.

In Fig. 5.9, the Hall resistance data are dominated by a linear contribution with a negative slope from the OHE. The sign and magnitude of the slope provide information

on the carrier type and concentration, respectively. The non-linear component of the Hall resistance is from the AHE. After subtracting the linear background from OHE, the AHE component is shown in the inset in Fig. 5.9(a). A small amount of hysteresis is observed from the field dependence of $M$, though the size of the hysteresis loop seems to be larger than that found with magnetization measurements. So far very few AHE results have been reported in ZnO DMS materials, [49-53] and for all these reports, the AHE contributions in ZnO DMS are very small compared to other DMS materials, such as GaAs:Mn[2] and GaAs:In.[5-6] Most researcher consider the AHE to be a useful tool for demonstrating the intrinsic nature of ferromagnetic order.[49,52]

The first term in Equation (5-1) dominates, but it is possible to determine $R_S$ by extrapolating high-field (>3T) $R_{Hall}$ data, where $M$ is saturated, back to the origin. The data for $R_{Hall}$, at positive and negative high fields, were each fit to straight lines. The slopes of these lines correspond to $R_0/d$. The distance between the two intercepts on the vertical axis is $2R_S\mu_0M/d$. The ordinary Hall coefficient $R_0$ and anomalous Hall coefficient $R_S$, determined with this procedure, at 10 K, 50 K, and 300 K are listed in Table 5.2. The electron carrier concentration $n$ of this sample at 10 K, 50 K, and 300 K were also listed in the table, which were derived from the Hall coefficient $R_0$ and the relation $n = -1/(eR_0)$. The error bars on $R_S$ come primarily from the high-field extrapolation of data with some experimental noise. The error bars on $R_0$ are orders of

magnitude smaller than the $R_0$ values. So no error bar for $R_0$ or $n$ was included in Table 5.2. To our knowledge, we are the first to report $R_S$ for ZnO-based DMS materials. Even though the AHE contribution to the Hall resistance is much smaller than the OHE contribution. $R_S$ for ZnO:Co is large in comparison to values for transition metal ferromagnets.[68] The AHE is difficult to observe in ZnO:Co because the OHE contribution is increased by a small carrier concentration (comparing to metals and III-As:Mn DMS) and the AHE contribution is reduced from a small magnetization per unit volume.

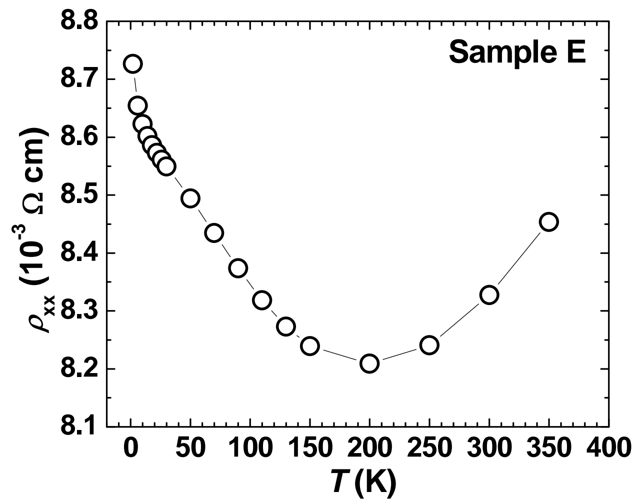


FIG. 5.10. Temperature-dependence of the resistivity of a ZnO:Co thin film (sample E).

Figure 5.10 shows the temperature dependence of the resistivity $\rho_{xx}$ of ZnO:Co thin film sample E measured from 2 to 350 K. The $\rho_{xx}$ does not show strong temperature

dependence (with orders of magnitude) over the temperature range, because the ZnO:Co thin film is a degenerate semiconductor with this electron carrier concentration. The resistivity values of sample E at 10 K, 50 K, and 300 K are also listed in Table 5.2. In general, the anomalous Hall resistivity $\rho_{\mathrm{AHE}}$ has both a linear and quadratic dependence on the film resistivity $\rho_{\mathrm{xx}}$ as

$$\rho_{\mathrm{AHE}} = \phi_{\mathrm{sk}} \rho_{\mathrm{xx}} + b_{\mathrm{sj}} \rho_{\mathrm{xx}}^2 \qquad (5\text{-}2)$$

The linear term is from skew scattering and the quadratic term originates from a side jump mechanism related to a material's intrinsic properties. The anomalous Hall resistivity $\rho_{\mathrm{AHE}}$ is defined as $\rho_{\mathrm{AHE}} = (\mu_0 M) R_{\mathrm{S}}$ from $\rho_{\mathrm{Hall}} = R_{\mathrm{Hall}} \cdot d = (\mu_0 H) R_0 + (\mu_0 M) R_{\mathrm{S}} \equiv \rho_{\mathrm{OHE}} + \rho_{\mathrm{AHE}}$, an equivalent equation as Equation (5-1), where $\rho_{\mathrm{Hall}}$ and $\rho_{\mathrm{OHE}}$ are Hall resistivity and ordinary Hall resistivity, respectively.

Figure 5.11 shows $\rho_{\mathrm{AHE}}/\rho_{\mathrm{xx}}$ versus $\rho_{\mathrm{xx}}$, measured at three temperatures. From a linear fit to the data, $\phi_{\mathrm{sk}} = -3.2 \times 10^{-3}$ and $b_{\mathrm{sj}} = 0.39\ \Omega^{-1}\mathrm{cm}^{-1}$. The physical meaning of $\phi_{\mathrm{sk}}$ is the skew scattering angle of a material in radian unit. The negative sign and milliradian magnitude of $\phi_{\mathrm{sk}}$ are common for intrinsic ferromagnetic materials, such as most of the transition metal ferromagnets.[69] The presence of a side-jump contribution further support an intrinsic origin for the ferromagnetism in ZnO:Co thin films.

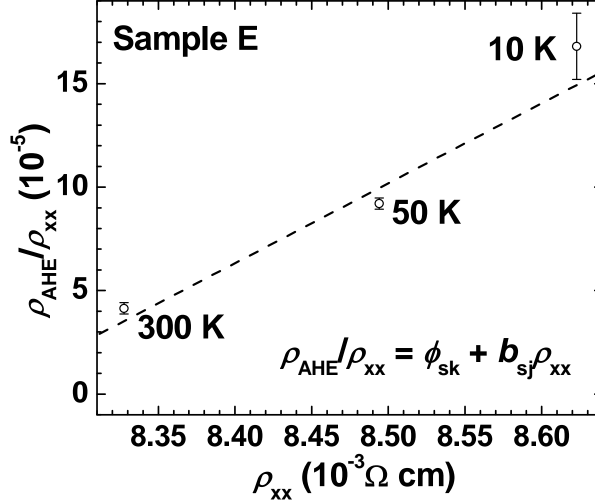


FIG. 5.11. The ratio of the anomalous Hall resistivity $\rho_{AHE}$ to the resistivity $\rho_{xx}$ as a function of the resistivity $\rho_{xx}$.

## 5.4 Summary

In summary, diluted magnetic semiconducting ZnO:Co thin films with above room-temperature $T_C$ were prepared. The structural, magnetic, and electrical transport properties of ZnO:Co thin films were comprehensively characterized. No secondary phases were observed by TEM and XRD. Ferromagnetism was observed in ZnO:Co thin films with a Curie temperature far above room-temperature. The saturated magnetization of the ZnO:Co thin films increases dramatically when the free electron carrier concentration exceeds ~$10^{19}$ $cm^{-3}$, indicating a carrier-mediated mechanism for ferromagnetism. The ZnO:Co thin films show magnetic anisotropy with the easy

magnetization axis parallel to the film plane. A strong temperature dependence and competition between positive and negative contributions were observed in magnetoresistance of the ZnO:Co thin films. Finally, an anomalous Hall effect was observed and analyzed in the ZnO:Co thin films, consistent with long-range ferromagnetism. The anomalous Hall coefficient and its dependence on longitudinal resistivity were analyzed. The presence of a side-jump contribution further supports an intrinsic origin for ferromagnetism in ZnO:Co thin films. These observations together with the magnetic anisotropy and magnetoresistance results, lend supports to an intrinsic carrier-mediated mechanism for the ferromagnetic exchange in ZnO:Co DMS materials.

## 5.5 Acknowledgement

Most of the results in this chapter were published on *Journal of Applied Physics* 104, 113712 (2008). This work was supported by ONR/DMEA through the Center of Nanomaterials and Nanodevices (CNN) under the award No. H94003-08-2-0803. The electron microscopy studies were performed at the Electron Microbeam Analysis Laboratory at the University of Michigan, which was supported by the National Science Foundation under grant No. DMR-0315633.

## References

[1] J. K. Furdyna, J Appl. Phys. **64**, R29 (1988).

[2] H. Ohno, Science **281**, 951 (1998).

[3] R. Flederling, M. Keim, G. Reuscher, W. Ossau, G. Schmidt, A. Waag, L. W. Molenkamp, Nature **402**, 787 (1999).

[4] Y. Ohno, D. K. Young, B. Beschoten, F. Matusukura, H. Ohno, D. D. Awschalom, Nature **402**, 790 (1999).

[5] H. Ohno, D. Chiba, F. Matsukura, T. Omiya, E. Abe, T. Dietl, Y. Ohno, K. Ohtani, Nature **408**, 944 (2000).

[6] D. Chiba, M. Yamanouchi, F. Matsukura, H. Ohno, Science **301**, 943 (2003).

[7] K. Ando, Science **312**, 1883 (2006).

[8] C. Liu, F. Yun, H. Morkoç, J. Mater. Sci: Mater. Electron. **16**, 555 (2005).

[9] S. J. Pearton, W. H. Heo, M. Ivill, D. P. Norton, T. Steiner, Semicond. Sci. Technol. **19**, R59 (2004).

[10] T. Dietl, H. Ohno, F. Matsukura, J. Cibert, D. Ferrand, Science **287**, 1019 (2000).

[11] K. Sato, H. Katayama-Yoshida, Semicond. Sci. Technol. **17**, 367 (2002).

[12] Z. Jin, T. Fukumura, M. Kawasaki, K. Ando, H. Saito, T. Sekiguchi, Y. Z. Yoo, M. Murakami, Y. Matsumoto, T. Hasegawa, H. Koinuma, Appl. Phys. Lett. **78**, 3824 (2001).

[13] K. Ueda, H. Tabata, T. Kawai, Appl. Phys. Lett. **79**, 988 (2001).

[14] W. Jung, S.-J. An, G.-C. Yi, C. U. Jung, S.-I. Lee, and S. Cho, Appl. Phys. Lett. **80**, 4561 (2002).

[15] P. Sharma, A. Gupta, K. V. Rao, Frank J. Owens, R. Sharma, R. Ahuja, J. M. Osorio Guillen, B. Johansson, and G. A. Gehring, Nat. Mater. **2**, 673 (2003).

[16] D. P. Norton, S. J. Pearton, A. F. Hebard, N. Theodoropoulou, L. A. Boatner, and R. G. Wilson, Appl. Phys. Lett. **82**, 239 (2003).

[17] S. Ramachandran, A. Tiwari, and J. Narayan, Appl. Phys. Lett. **84**, 5255 (2004).

[18] J. M. Baik, J. -L. Lee, Adv. Mater. **17**, 2745 (2005).

[19] O. D. Jayakumar, I. K. Gopalakrishnan, S. K. Kulshreshtha, Adv. Mater. **18**, 1857 (2006).

[20] X. Wang, J. Xu, B. Zhang, H. Yu, J. Wang, X. Zhang, J. Yu, Q. Li, Adv. Mater. **18**, 2476 (2006).

[21] T. Fukumura, Z. Jin, M. Kawasaki, T. Shono, T. Hasegawa, S. Koshihara, and H. Koinuma, Appl. Phys. Lett. **78**, 958 (2001).

[22] S. W. Yoon, S. -B.Cho, S. C. We, S. Yoon, B. J. Suh, H. K. Song, Y. J. Shin, J Appl. Phys. **93**, 7879 (2003).

[23] S. S. Kim, J. H. Moon, B. -T. Lee, O. S. Song, J. H. Je, J Appl. Phys. **95**, 454 (2004).

[24] S. Kolesnik, B. Dabrowski, J. Mais, J Appl. Phys. **95**, 2582 (2004).

[25] M. Bouloudenine, N. Viart, S. Colis, J. Kortus, and a. Dinia, Appl. Phys. Lett. **87**, 052501 (2005).

[26] J. H. Kim, H. Kim, D. Kim, Y. E. Ihm, W. K. Choo, J Appl. Phys. **92**, 6066 (2002).

[27] D. P. Norton, M. E. Overberg, S. J. Pearton, K. Pruessner, J. D. Budai, L. A. Boatner, M. F. Chisholm, J. S. Lee, Z. G. Khim, Y. D. Park, R. G. Wilson, Appl. Phys. Lett. **83**, 5488 (2003).

[28] J. H. Park, M. G. Kim, H. M. Jang, S. Ryu, Y. M. Kim, Appl. Phys. Lett. **84**, 1388 (2004).

[29] K. Ando, H. Saito, Z. Jin, T. Fukumura, M. Kawasaki, Y. Matsumoto, H. Koinuma, J Appl. Phys. **89**, 7284 (2001).

[30] H. J. Lee, S. Y. Jeong, C. R. Cho, C. H. Park, Appl. Phys. Lett. **81**, 4020 (2002).

[31] K. Rode, A. Anane, R. Mattana, J. -P. Contour, O. Durand, R. Lebourgeois, J Appl. Phys. **93**, 7676 (2003).

[32] D. A. Schwartz and D. R. Gamelin, Adv. Mater. **16**, 2115 (2004).

[33] N. Khare, M. J. Kappers, M. Wei, M. G. Blamire, J. L. MacManus-Driscoll, Adv. Mater. **18**, 1449 (2006).

[34] M. H. F. Sluiter, Y. Kawazoe, P. Sharma, A. Inoue, A. R. Raju, C. Rout, and U. V. Waghmare, Phys. Rev. Lett. **94**, 187204 (2005).

[35] K. R. Kittilstved, D. A. Schwartz, A. C. Tuan, S. M. Heald, S. A. Chambers, and D. R.

Gamelin, Phys. Rev. Lett. **97**, 037203 (2006).

[36] J. Alaria, H. Bieber, S. Colis, G. Schmerber, and A. Dinia, Appl. Phys. Lett. **88**, 112503 (2006).

[37] X. C. Liu, E. W. Shi, Z. Z. Chen, H. W. Zhang, B. Xiao, and L. X. Song, Appl. Phys. Lett. **88**, 252503 (2006).

[38] T. Zhang, L. X. Song, Z. Z. Chen, E. W. Shi, L. X. Chao, and H. W. Zhang, Appl. Phys. Lett. **89**, 172502 (2006).

[39] M. Venkatesan, P. Stamenov, L. S. Dorneles, R. D. Gunning, B. Bernoux, and J. M. D. Coey, Appl. Phys. Lett. **90**, 242508 (2007).

[40] Z. Yang, J. L. Liu, M. Biasini, and W. P. Beyermann, Appl. Phys. Lett. **92**, 042111 (2008).

[41] K. R. Kittilstved, N. S. Norberg, and D. R. Gamelin, Phys. Rev. Lett. **94**, 147209 (2005).

[42] Z. B. Gu, M. H. Lu, J. Wang, D. Wu, S. T. Zhang, X. K. Meng, Y. Y. Zhu, S. N. Zhu, Y. F. Chen, and X. Q. Pan, Appl. Phys. Lett. **88**, 082111 (2006).

[43] H. Y. Xu, Y. C. Liu, C. S. Xu, Y. X. Liu, C. L. Shao, and R. Mu, Appl. Phys. Lett. **88**, 242502 (2006).

[44] W. Yan, Z. Sun, Q. Liu, Z. Li, T. Shi, F. Wang, Z. Qi, G. Zhang, S. Wei, H. Zhang, and Z. Chen, Appl. Phys. Lett. **90**, 242509 (2007).

[45] Q. Wan, Appl. Phys. Lett. **89**, 082515 (2006).

[46] M. Ivill, S. J. Pearton, Y. W. Heo, J. Kelly, A. F. Hebard, and D. P. Norton, J. Appl. Phys. **101**, 123909 (2007).

[47] K. Lord, T. M. Williams, D. Hunter, K. Zhang, J. Dadson, and A. K. Pradhan, Appl. Phys. Lett. **88**, 262105 (2006).

[48] S. Lee, D. Y. Kim, Y. Shon, and C. S. Yoon, Appl. Phys. Lett. **89**, 022120 (2006).

[49] Y. Z. Peng, T. Liew, T. C. Chong, C. W. An, W. D. Song, Appl. Phys. Lett. **88**, 192110 (2006).

[50] Q. Xu, L. Hartmann, H. Schmidt, H. Hochmuth, M. Lorenz, R. Schmidt-Grund, C. Sturm, D. Spemann, M. Grundmann, Phys. Rev. B **73**, 205342 (2006).

[51] Q. Xu, L. Hartmann, H. Schmidt, H. Hochmuth, M. Lorenz, R. Schmidt-Grund, C. Sturm, D. Spemann, M. Grundmann, Y. Liu, J. Appl. Phys. **101**, 063918 (2007).

[52] W. Shim, K. Lee, W. Lee, K. A. Jeon, S. Y. Lee, M. H. Jung, J. Appl. Phys. **101**, 123908 (2007).

[53] H. Pan, J. B. Yi, L. Shen, R. Q. Wu, J. H. Yang, J. Y. Lin, Y. P. Feng, J. Ding, L. H. Van, J. H. Yin, Phys. Rev. Lett. **99**, 127201 (2007).

[54] Z. Yang, D. C. Look, J. L. Liu, Appl. Phys. Lett. **94**, 072101 (2009).

[55] J. M. D. Coey, M. Venkatesan, and C. B. Fitzgerald, Nat. Mater. **4**, 173 (2005).

[56] P. Sati, R. Hayn, R. Kuzian, S. Régnier, S. Schäfer, A. Stepanov, C. Morhain, C.

Deparis, M. Laügt, M. Goiran, and Z. Golacki, Phys. Rev. Lett. **96**, 017203 (2006).

[57] M. Venkatesan, C. B. Fitzgerald, J. G. Lunnery, and J. M. D. Coey, Phys. Rev. Lett. **93**, 177206 (2004).

[58] C. Song, K. W. Geng, F. Zeng, X. B. Wang, Y. X. Sheng, F. Pan, Y. N. Xie, T. Liu, T. T. Zhou, and Z. Fan, Phys. Rev. B **73**, 024405 (2006).

[59] A. Zukova, A. Teiserskis, S. Van Dijken, Y. K. Gun'Ko, V. Kazlauskiene, Appl. Phys. Lett. **89**, 232503 (2006).

[60] S. B. Ogale, R. J. Choudhary, J. P. Buban, s. E. Lofland, S. R. Shinde, S. N. Kale, V. N. Kulkarni, J. Higins, C. Lanci, J. R. Simpson, N. D. Browning, S. Das Sarma, H. D. Drew, R. L. Greene, T. Venkatesan, Phys. Rev. Lett. **91**, 077205 (2003).

[61] T. Andrearczyk, J. Jaroszyński, G. Grabeki, T. Dietl, T. Fukumura, M. Kawasaki, Phys. Rev. B **72**, 121309R (2005).

[62] J. Wang, Z. Gu, M. Lu, D. Wu, C. Yuan, S. Zhang, Y. Chen, S. Zhu, Y. Zhu, Appl. Phys. Lett. **88**, 252110 (2006).

[63] Q. Xu, L. Hartmann, H. Schmidt, H. Hochmuth, M. Lorenz, R. Schmidt-Grund, d. Spemann, M. Grundmann, J. Appl. Phys. **100**, 013904 (2006).

[64] M. Gacic, G. Jakob, C. Herbort, H. Adrian, Phys. Rev. B **75**, 205206 (2007).

[65] F. Reuss, S. Frank, C. Kirchner, R. Kling, Th. Gruber, A. Waag, Appl. Phys. Lett. **87**, 112104 (2005).

[66] R. P. Khosla, J. R. Fischer, Phys. Rev. B **2**, 4084 (1970).

[67] Z. Yang, Z. Zuo, Y. Pu, W. P. Beyermann, J. Shi, J. L. Liu, (unpublished).

[68] R. C. O'Handley, Modern Magnetic Materials, John Wiley & Sons, 2000, p.570-573.

[69] E. P. Wohlfarth, Ferromagnetic Materials Vol. 3, Ch. 9, Transport Properties of Ferromagnets (by I. A. Campbell and A. Fert), North Holland Publishing Company, 1982, p.766-800.

# 6. Chapter 6 Manganese Doping in Zinc Oxide

## 6.1 Introduction

In recent years, ZnO-based diluted magnetic semiconductor (DMS) materials have been widely studied.[1-19] Compared to other DMS materials, the ZnO-based DMS has a potential advantage for future device applications, which is its above-room-temperature Curie temperature ($T_C$), according to Dietl's calculations.[20] However, unlike GaAs:Mn[21] and InAs:Mn[22] DMSs, the mechanism and origin of the ferromagnetism in ZnO-based DMSs are still controversial and needs further clarification. Very recently, the focus of ZnO DMS research has shifted from achieving room-temperature ferromagnetism in ZnO to understanding the mechanism of ferromagnetism and whether it originates from intrinsic carrier mediation or extrinsic clustering/phase segregation. Recently, Yang *et al* observed ferromagnetism in *n*-type ZnO:Mn thin films with a $T_C$ above room-temperature, and the magnetization shows a monotonic dependence on the electron carrier concentration ($n$).[19] These results are surprising because Mn-doped ZnO was theoretically predicted to be ferromagnetic only in a hole-rich environment.[20,23] So additional characterizations and analyses, such as systematic microstructure and magnetotransport studies, were performed on ZnO:Mn DMS thin films, to further investigate and clarify the origin of the ferromagnetism. In this paper, results from transmission electron microscopy (TEM) studies, magnetoresistance,

and Hall effect on ZnO:Mn thin film samples are comprehensively discussed.

### 6.1.1 Co-doped ZnO *vs*. Mn-doped ZnO

The free carriers play an important role in DMS materials.[20, 23-24] Based on the first principle calculations, the Co-doped ZnO will be ferromagnetic in an *electron* rich environment while the Mn-doped ZnO will be ferromagnetic in a *hole* rich environment.[23] In the previous chapter, the properties of Co-doped ZnO have already been discussed. In this and next chapters, we report our recent results on the properties of *n*-type Mn-doped ZnO.

### 6.1.2 Current status of Mn-doped ZnO study

Many experimental studies have already been performed on the ZnO based DMS materials in recent years, including ZnO:Mn materials. However, the results are still very controversial, showing both ferromagnetism and non-ferromagnetic states in ZnO:Mn. Some researchers claimed that the observed ferromagnetism in ZnO:Mn is due to the incorporation of Zn into Mn oxides. Most recently, different groups reported hole-mediated ferromagnetism in *p*-type ZnO:Mn, by codoping Mn with an acceptor dopant, such as N, P, and As. This seems to be consistent with the theoretical predictions. However, ferromagnetism has also been observed in *n*-type ZnO:Mn. So the

circumstances under which ZnO:Mn can be ferromagnetic is still debatable. In this chapter, we report our experimental results on *n*-type ZnO:Mn thin films, showing strong evidence for electron concentration dependent magnetization, supporting an electron-mediated ferromagnetic exchange mechanism in ZnO:Mn.

## 6.2 Experiment

### 6.2.1 Sample preparations

The ZnO:Ga thin films were grown on *r*-cut sapphire substrates using plasma-assisted molecular-beam epitaxy (MBE). Regular Knudsen effusion cells filled with elemental Zn (6N) and Ga (6N) were used as zinc and gallium sources. A radiofrequency plasma supplied with $O_2$ (5N) was used as the oxygen source. The purpose of Ga incorporation is to tune the electron carrier concentration in ZnO.[24] The substrate temperature was held constant at 565 °C during the growth. After the growth, the samples were annealed *in situ* in vacuum at 800 °C for 20 minutes to activate the Ga dopants and improve crystallinity. The Mn ions were implanted into MBE-grown ZnO thin films with electron carrier concentrations ranging from $3.5\times10^{18}$ to $1.2\times10^{20}$ $cm^{-3}$ (as shown in Table 6.1) with a dose of $3\times10^{16}$ $cm^{-2}$ using an implantation energy of 50 keV. All the Mn-implanted ZnO samples were annealed at 900 °C for 5 min in nitrogen after implantation. Typical Mn-implanted ZnO:Ga thin film samples (these samples are

referred to as ZnO:Mn in the paper) were used in the microstructure and transport studies in this paper.

### 7.1.1 Characterizations

Room-temperature Hall effect measurements were carried out before and after implantation using an ECOPIA HMS-3000 Hall effect measurement system. It showed negligible changes in the electron carrier concentration after Mn implantation. X-ray diffraction (XRD) measurements were performed to check the crystallinity of the ZnO thin films using a Bruker D8 Advance x-ray diffractometer. Secondary ion mass spectroscopy (SIMS) measurements were performed to characterize the Mn ion profile along the depth of the ZnO films using a PHI ADEPT-1010 Dynamic SIMS system. The magnetic properties were measured with a Quantum Design MPMS-XL SQUID magnetometer using an in-plane geometry (magnetic field parallel to the film) on all samples, unless specified differently.

Transmission electron microscope analysis, including selected area electron diffraction (SAED), high-angle annular dark field (HAADF) (Z-contrast) images, and x-ray energy dispersive spectroscopy (EDS) were performed using a JEOL 2010F analytical electron microscope equipped with a field emission gun. Further TEM studies, including SAED and EDS, as well as high-resolution TEM (HRTEM) studies, were also

carried out using a JEOL JEM-3011 high resolution electron microscope operated at 300 kV, with a 0.17 nm point-to-point resolution. Cross-sectional TEM specimens were prepared by mechanical grinding, polishing, and dimpling, followed by argon ion milling in a Gatan Model 691 Precision Ion Polishing System at incident angles between 4.0° and 5.5° to electron transparency. Magnetoresistance and field-dependent Hall effect measurements were performed in a Quantum Design PPMS with magnetic fields up to 10 T. The direction of the magnetic field was perpendicular to the film plane during the magnetoresistance measurements.

## 6.3 Results and discussions

### 6.3.1 Structural properties

Figure 6.1 shows the XRD spectra for sample A before and after Mn implantation. Both the ZnO and the ZnO:Mn thin films show high crystallinity. Only the $(11\bar{2}0)$ peaks associated with the ZnO wurtzite structure were observed at 56.8º and 56.7º in the ZnO and ZnO:Mn thin films, respectively.

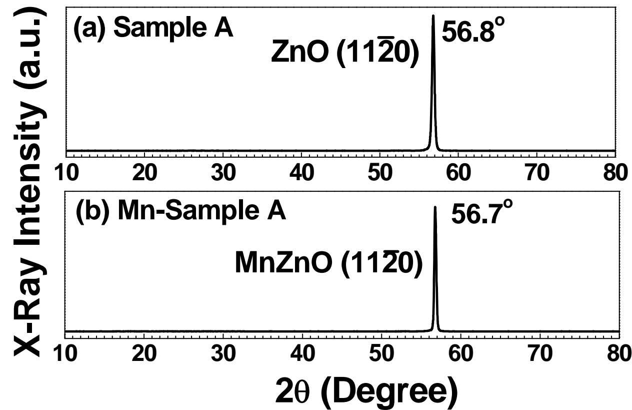


FIG. 6.1 XRD spectra of (a) sample A before Mn implantation and (b) sample A after Mn implantation. The ZnO thin films show good crystallinity both before and after Mn implantation.

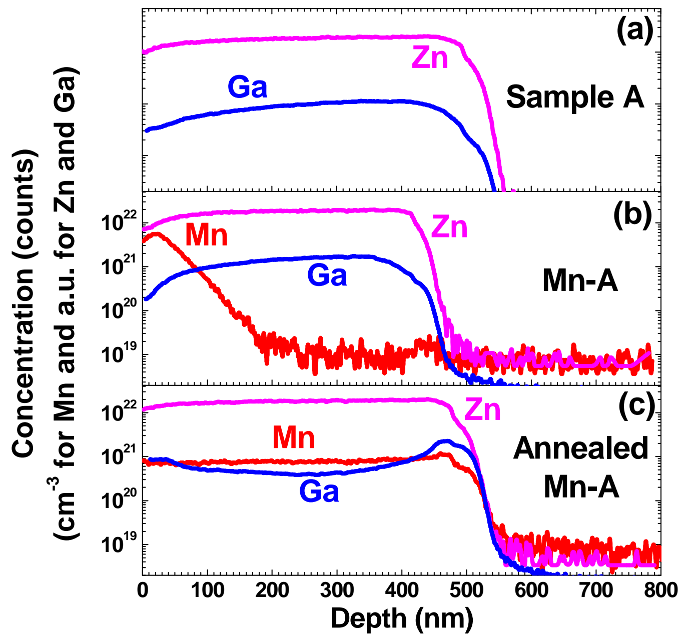


FIG. 6.2 SIMS spectra of (a) sample A before Mn implantation, (b) sample A after Mn implantation, and (c) Mn-implanted sample A after annealing. The Zn and Ga concentrations are nearly uniform in the ZnO thin film before implantation. After implantation, Mn ions have a Gaussian distribution with the peak near the surface as seen in unannealed Mn-implanted ZnO sample. After annealing, the Mn ions redistribute to a relatively uniform profile throughout the depth of the film. A small percentage of the Mn ions penetrate the ZnO film reaching the sapphire substrates in both unannealed and annealed ZnO:Mn samples. The density of the residual Mn concentration in the substrate is more than one order of magnitude smaller than in the ZnO film layer.

Figure 6.2 shows the SIMS data for (a) the ZnO sample A, (b) the Mn-implanted ZnO sample A, and (c) the Mn-implanted ZnO sample A after annealing. As shown in Fig. 6.2(a), nearly uniform Zn and Ga concentrations are observed in the ZnO thin film before implantation. In the Mn-implanted sample in Fig. 6.2(b), the profile of the Mn concentration follows an approximate Gaussian distribution, which is a common implantation profile. The Gaussian peak is near the surface, which was intentionally designed using a relatively small implantation energy to prevent a large amount of Mn ions from reaching the sapphire substrate. The Mn ions redistribute to a comparatively uniform profile along the depth of the film after annealing at 900 ˚C for 5 minutes as shown in Fig. 6.2(c). While a small amount of the Mn ions may reach the sapphire substrate, the density of residual Mn in the substrate is more than one order of magnitude smaller than the Mn in the ZnO film layer. To remove any possible contributions from the substrates to the magnetic measurements, we began by measuring the ZnO:Mn film on the sapphire substrate. Then we completely etched away the ZnO:Mn layer and measured just the sapphire substrate. The magnetic response of the ZnO:Mn films was obtained by subtracting the two data sets.

Figure 6.3(a) shows a typical cross-sectional TEM image of the ZnO:Mn thin film. The image reveals a relatively low dislocation density, indicating a high-quality film. To investigate the crystalline quality and uniformity of the ZnO:Mn thin film, SAED patterns were taken.

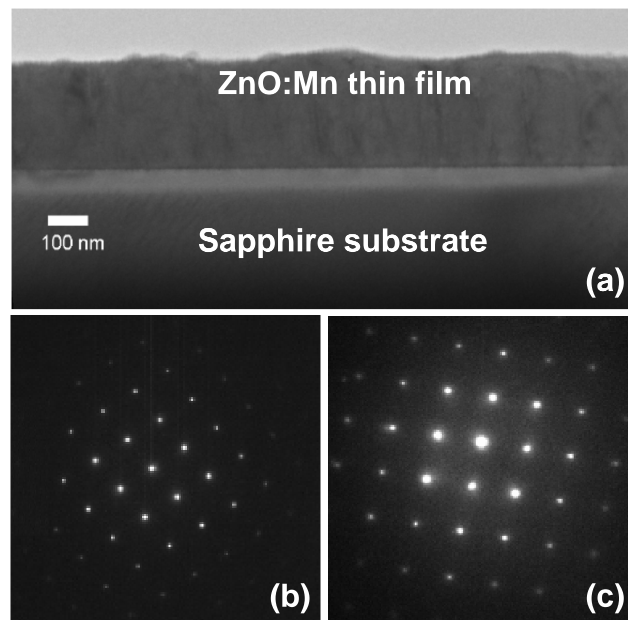


FIG. 6.3. (a) Cross-sectional TEM image of a ZnO:Mn thin film on a sapphire substrate. (b) A typical SAED pattern from the ZnO:Mn thin film, and (c) SAED pattern from the sapphire substrate.

Figure 6.3(b) shows a typical SAED pattern of the ZnO:Mn thin film. SAED patterns were also taken at more different locations throughout the ZnO:Mn thin film (not shown here). All the SAED patterns are very similar to each other and lack of any unexpected diffraction spots, indicating a high degree of uniformity and no secondary

phases in the ZnO:Mn film. The SAED pattern of the sapphire substrate is shown in Fig. 6.3(c) for comparison.

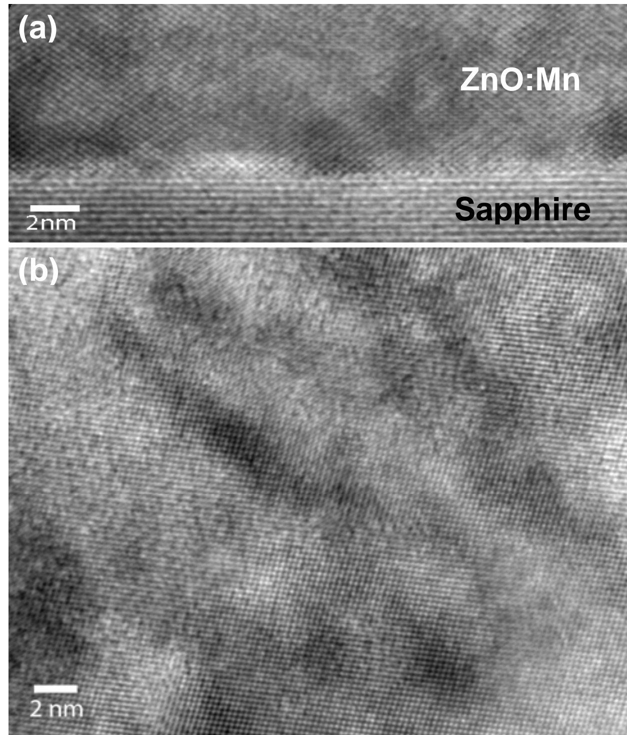


FIG. 6.4. (a) Cross-sectional HRTEM image of the interface between the ZnO:Mn thin film and the sapphire substrate, showing an atomically sharp interface. (b) HRTEM image of the ZnO:Mn thin film. The film appears to be highly crystalline with no secondary phase.

HRTEM was performed throughout a wide area of the ZnO:Mn thin film and the film/substrate interface. Typical HRTEM images are shown in Fig. 6.4(a), Fig. 6.4(b), Fig. 6.5(a), and Fig. 6.5(b), respectively. The zone axes of the film and the substrate are

approximately 4° apart from each other, indicating a slight twist between the film and the substrate, but otherwise crystallographic alignment of the ZnO:Mn layer and the sapphire substrate at the interface is good. HRTEM studies indicate also that the film is of high crystallinity and no clustering or secondary phase was observed, however, there are a small number of stacking faults visible.

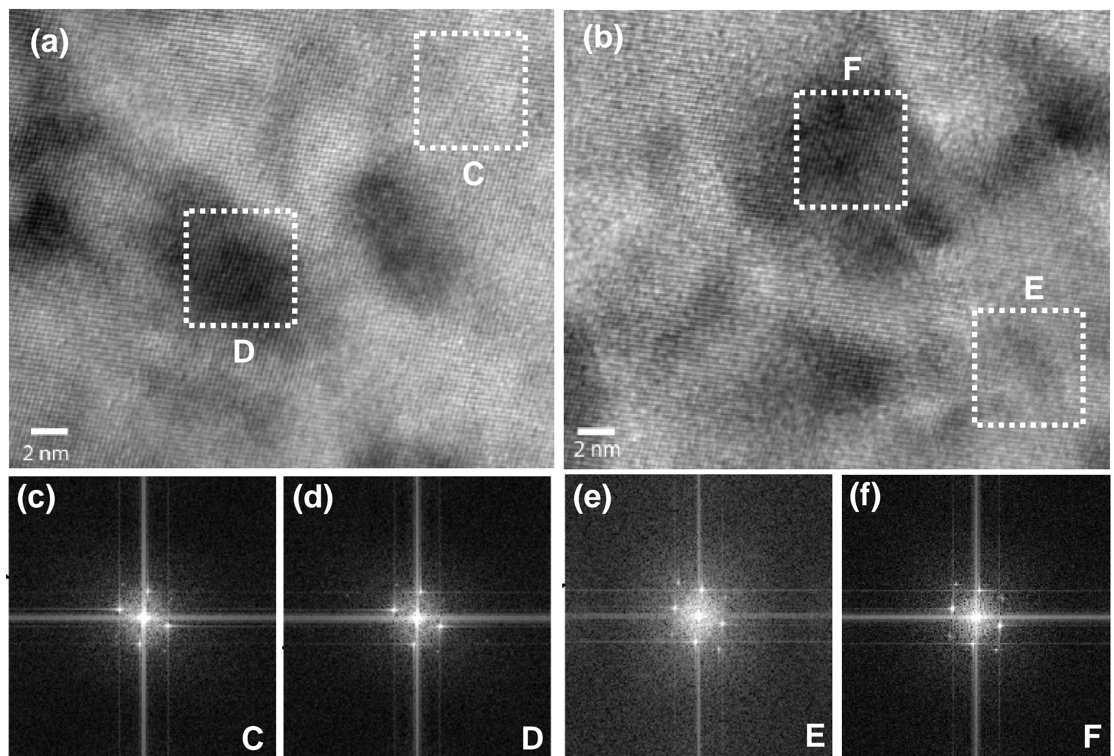


FIG. 6.5. (a)-(b) Two HRTEM images taken from different places on the ZnO:Mn thin film. (c)-(f) The fast Fourier transform patterns corresponding to the square region marked with dotted lines in (a) and (b).

Figures 6.5(a) and (b) show the HRTEM images from two different areas of the ZnO:Mn thin film. Fast Fourier transform (FFT) patterns were taken on the dark and light areas to examine the uniformity of the film. Figures 6.5(c)-(f) show the FFT patterns from the areas indicated in Figs. 6.5(a)-(b). These four FFT patterns are nominally identical, corroborating the evidence from the SAED patterns in indicating that the same crystal structure is present in these areas and that the dark region are simply contrast variations arising from the stacking faults or the slight variations in specimen thickness.

Conventional HRTEM is a very powerful technique for detecting any possible secondary phases. It is, however, limited by the relatively small region of material that is examined, compared to other techniques. Therefore, HAADF Z-contrast imaging was performed to further confirm our conclusion.

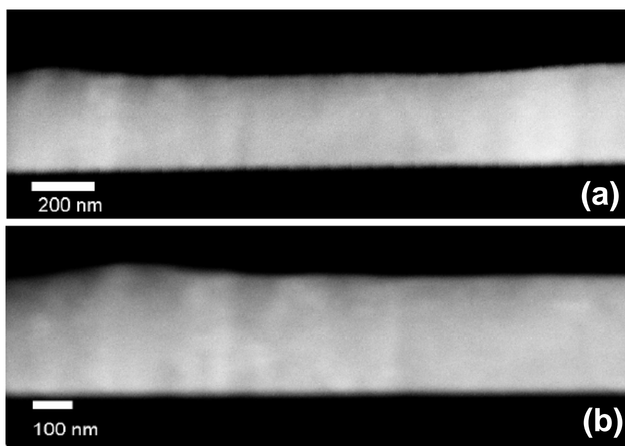


FIG. 6.6. (a)-(b) Two HAADF images of the ZnO:Mn thin film.

Figures 6.6(a) and (b) show typical HAADF Z-contrast images of the ZnO:Mn thin film. Because in HAADF Z-contrast imaging, contrast arises from the atomic number of the elements being probed, it is a powerful and popular technique for detecting and studying embedded nanoparticles or metal ion clusters in films,[25-26] and little contrast arises from sample thickness variation.[25] Larger atomic number element-related phases contribute to brighter contrast.[26] The HAADF Z-contrast imaging also shows a much larger region than the HRTEM is able to. No Mn-related segregated phases are detected in all the HAADF images of the ZnO:Mn thin film. The previous conclusion that the film is free of clustering/phase segregation is confirmed by the HAADF Z-contrast studies. Dietl *et al* proposed a model[27] to explain the origin of the ferromagnetism in transition-metal (TM) doped ZnO recently, which assigns the spontaneous magnetization of ZnO:TM to the uncompensated spins at the surface of antiferromagnetic TM-rich wurtzite (wz) ZnO:TM nanocrystals. These TM-rich wz ZnO:TM nanocrystals are immersed in a TM-poor paramagnetic ZnO:TM matrix. Since the nanocrystals are coherent with identical crystallographic structure and lattice constant to the surrounding ZnO:TM, they escape from the detection of standard HRXRD or HRTEM. HAADF Z-contrast images shown here are a good supplementary experimental proof, since it brings a better sensitivity and a larger possibility to detect the embedded "coherent" TM-rich ZnO:TM nanocrystals than HRTEM. Within the Z-contrast detection limit, no

evident signs of Mn-rich ZnO:Mn nanocrystals or Mn spinodal decomposition[28] were observed in the ZnO:Mn film.

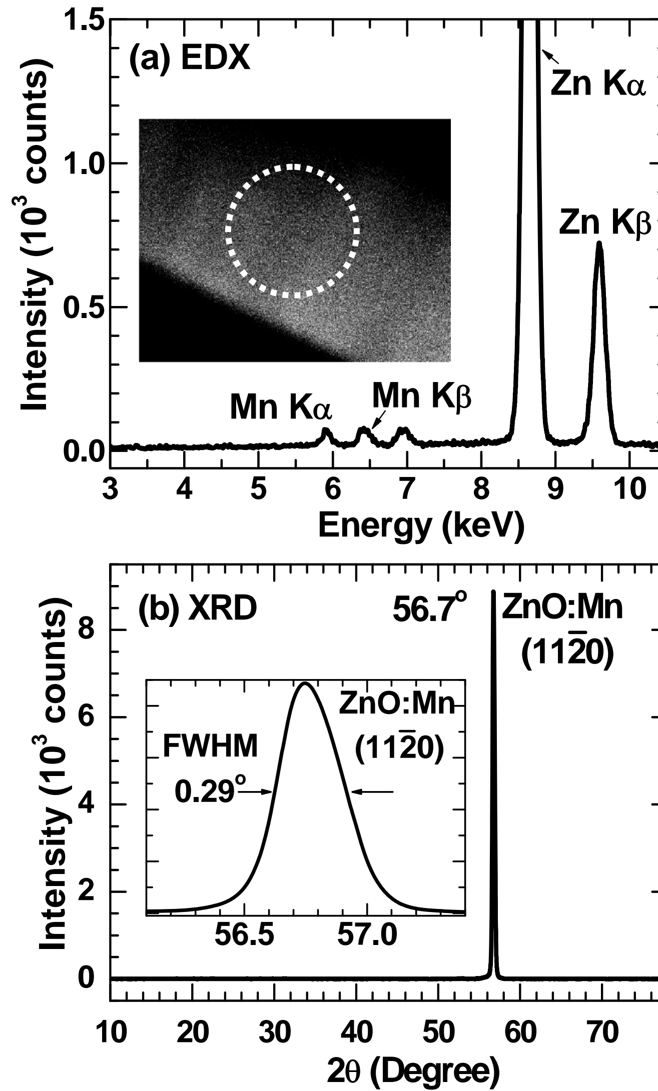


FIG. 6.7. (a) EDS spectrum of the ZnO:Mn thin film, showing Zn and Mn signals. The inset shows the electron microscopy image of the region where the EDS was taken. (b) XRD pattern of the ZnO:Mn thin film. The orientation of the ZnO:Mn thin film is along the $[11\bar{2}0]$ direction. The inset shows that the full-width at half-maximum of the $(11\bar{2}0)$ peak located at 56.7° is ~0.29°.

Figure 6.7 (a) shows an EDS spectrum from the ZnO:Mn thin film sample. The two strong peaks located at 8.65 and 9.59 keV are the signals from the Zn $K_\alpha$ and $K_\beta$ shells, respectively. Mn signals are observed at 5.89 and 6.42 keV, which are attributed to Mn $K_\alpha$ and $K_\beta$ shells, respectively. The inset in Fig. 6.7(a) shows the electron microscopy image of the region where the EDS measurements were performed. Figure 6.7(b) shows an XRD pattern for the ZnO:Mn thin film sample. The ZnO:Mn Wurtzite $(11\bar{2}0)$ peak was observed at 56.7˚, indicating that the growth direction (i. e. the out-of-plane direction) of the ZnO:Mn thin film is along the $[11\bar{2}0]$ direction. The inset shows the ZnO:Mn $(11\bar{2}0)$ peak has a full-width at half-maximum (FWHM) of ~0.29˚.

### 6.3.2 Magnetic properties

Figure 6.8 shows the magnetization as a function of the applied magnetic field at 300 K for ZnO:Mn (sample A), indicating ferromagnetic hysteresis. The saturated magnetization value is ~5.0 $\mu_B$ per Mn ion, which greatly exceeds the previously reported values for ZnO:Mn DMS materials, but it is smaller than the giant magnetic moment (~6.1$\mu_B$ per Co) observed for $Zn_{0.96}Co_{0.04}O$. The upper inset shows the magnetic field dependence of the magnetization on the same sample at 10 K with a slightly larger coercivity than that at 300 K. The bottom inset shows the temperature dependence of the

magnetization measured from 2 to 300 K. The magnetization is almost temperature-independent up to 300 K, indicating that the Curie temperature is well above room temperature. As we know, neither Mn metal nor any oxide of Mn is ferromagnetic (such as MnO, $MnO_2$, and $Mn_2O_3$), except for $Mn_3O_4$, which has a Curie temperature around 45 K. Since the ZnO:Mn thin film has a much higher Curie temperature than 45 K, the possibility of ferromagnetism in our ZnO:Mn films originating from the segregated Mn, or Mn related oxides is excluded.

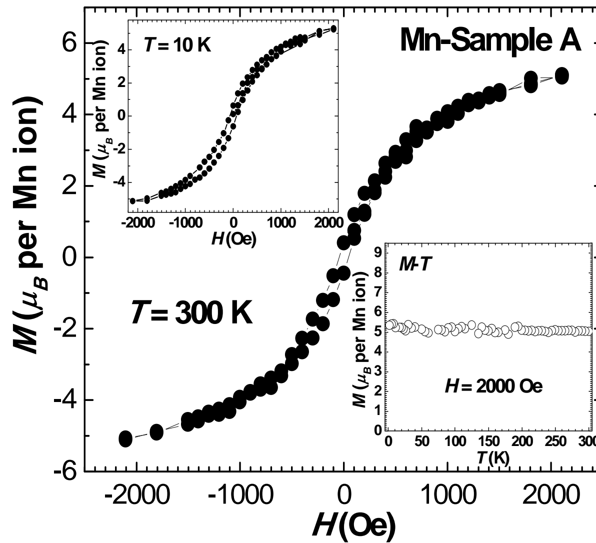


FIG. 6.8 Magnetic field dependence of the magnetization for the Mn-implanted ZnO sample A measured at 300 K. The ferromagnetic hysteresis loop is clearly observed. The upper inset shows the magnetic field dependence of the magnetization on the same sample at 10 K. The bottom inset shows the temperature dependence of the magnetization measured from 2 to 300 K, indicating that the Curie temperature of this sample is well above 300 K.

Figure 6.9(a) shows ferromagnetic hysteresis loops for ZnO:Mn thin films with different electron concentrations, and in Fig. 6.9(b) the relationship between the saturated magnetization ($M_S$) and the free electron carrier concentration ($n$) is plotted. ZnO:Mn samples A, B, C, and D with electron concentrations of $1.2\times10^{20}$, $4.7\times10^{19}$, $8.4\times10^{18}$, and $3.5\times10^{18}$ cm$^{-3}$, show 5.0, 4.5, 2.1, and 1.4 $\mu_B$ per Mn ion magnetization, respectively. These data are also summarized in Table 6.1, and they reveal a strong reduction of $M_S$ as the electron concentration decreases. Based on the theoretical calculations,[23] the Mn-doped ZnO should be ferromagnetic with an excess of hole, however, all of our ZnO:Mn thin films are strongly $n$-type. We conclude that the ferromagnetic exchange inside these ZnO:Mn thin films is mediated by electrons from shallow donor impurities.

Table 6.1 Electron carrier concentrations and the saturated magnetization for four different samples of ZnO thin films after Mn implantation.

| Sample | Electron Carrier Concentration (cm$^{-3}$) | Saturated Magnetization ($\mu_B$ per Mn) |
|---|---|---|
| A | $1.2 \times 10^{20}$ | 5.0 |
| B | $4.7 \times 10^{19}$ | 4.5 |
| C | $8.4 \times 10^{18}$ | 2.1 |
| D | $3.5 \times 10^{18}$ | 1.4 |

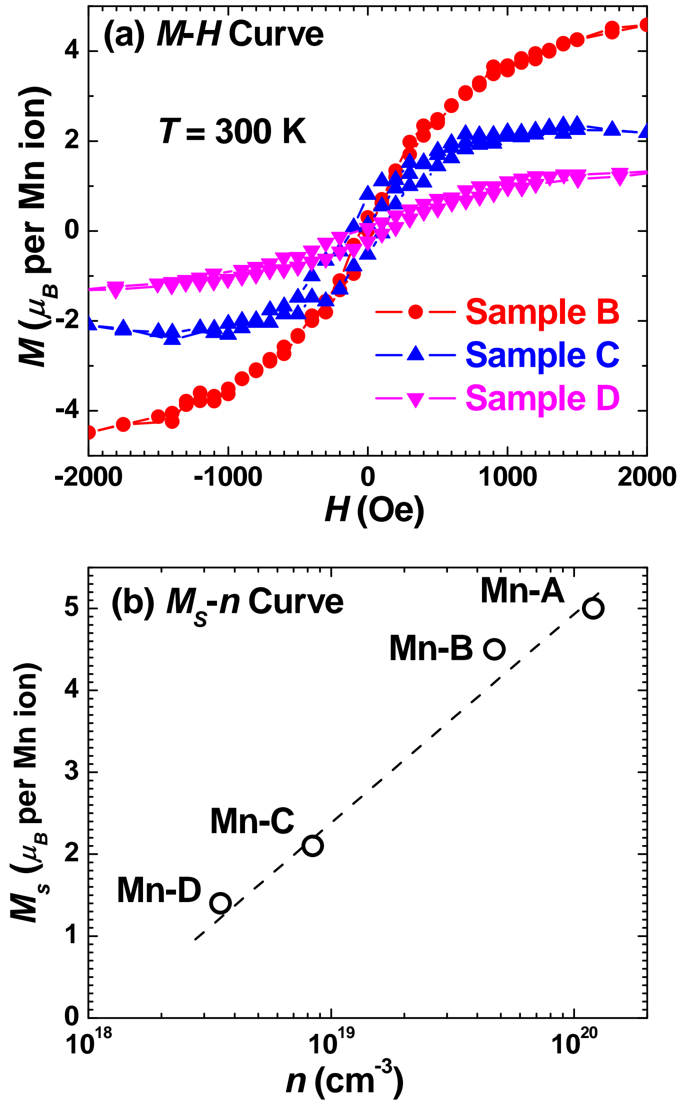


FIG. 6.9. (a) Magnetic field dependence of the magnetization for the Mn-implanted ZnO samples B, C, and D measured at 300 K. (b) The relation between the saturated magnetization $M_S$ and the electron carrier concentration ($n$). The $M_S$ of the samples show an electron concentration dependent behavior.

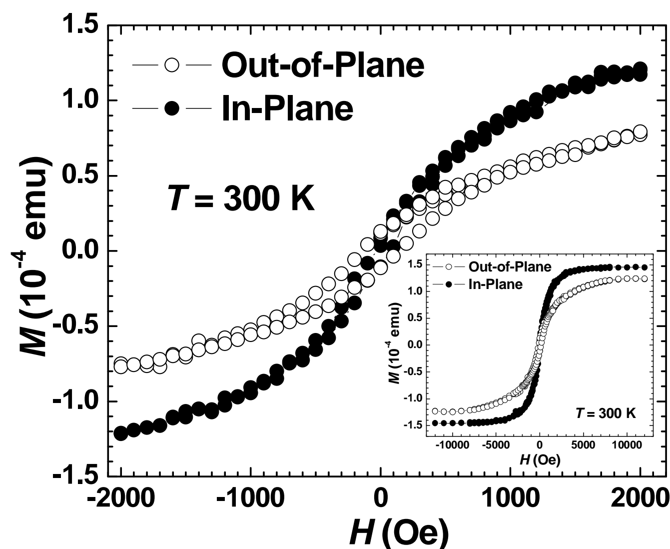


FIG. 6.10. Anisotropic magnetism for a ZnO:Mn thin film (sample B). The magnetic field dependence of the magnetizations for the out-of-plane (magnetic field perpendicular to the film) and in-plane (magnetic field parallel to the film) geometries are shown with the open and solid circles, respectively. The out-of-plane magnetization shows a smaller saturated magnetization but larger coercivity than in-plane magnetization. The inset shows the *M*-*H* curve measured over a larger magnetic field range of up to 12000 Oe.

Figure 6.10 shows the out-of-plane (open circules) and in-plane (solid circules) magnetic field dependence for a ZnO:Mn thin film (sample B). The out-of-plane magnetization shows a smaller saturated magnetization but larger coercivity than in-plane magnetization. The inset shows the *M*-*H* curve measured over a larger magnetic field range. The magnetic anisotropy is a further proof of the intrinsic nature of the ferromagnetism in ZnO DMS materials, since cluster-related ferromagnetism is generally isotropic. The ZnO thin films were epitaxially grown on *r*-plane sapphire with the growth

direction along the $a$-direction $[(11\bar{2}0)]$ as shown in the XRD spectra. The easy axis of the magnetization is in the plane while the hard axis of magnetization is parallel to the $a$-axis. Similar anisotropic results were also observed in ZnO:Co DMS materials.

### 6.3.3 Transport properties

Figure 6.11(a) shows the magnetoresistance (MR) spectra of the ZnO:Mn thin film sample at 5, 8, 10, 15, 20, 25, 30, 40, 50, and 100 K with magnetic fields up to 10 T. The magnetoresistance (MR) is defined as MR=$[R(H)-R(0)]/R(0)$. Figures 6.11(b)-(d) show the temperature dependence of the MR measured with a magnetic field of 10, 6, and 2 T. The vertical distance between the two thin lines in every circle symbol represents the error bar for that data point. (The uncertainty is as small as can be comparable to the size of the symbols.)

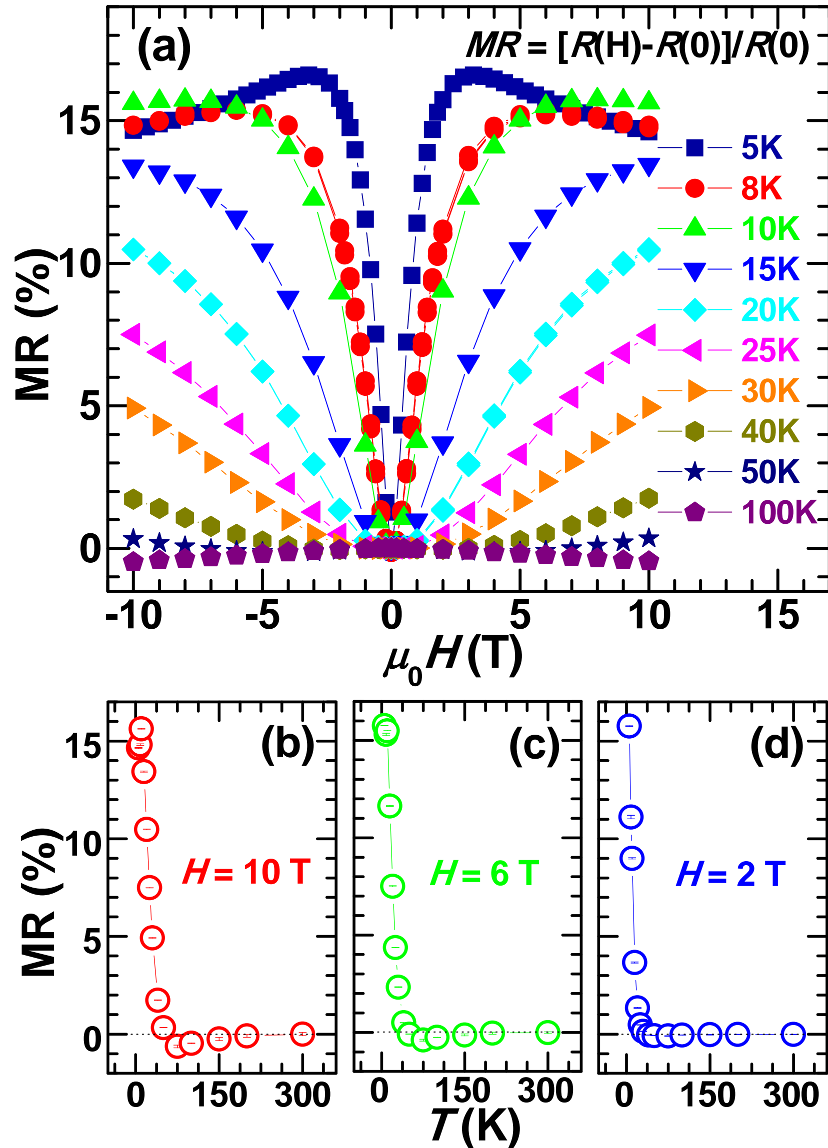


FIG. 6.11. (a) Magnetoresistance (MR) of the ZnO:Mn thin film at different temperatures. (b)-(d) The temperature dependence of the MR from the ZnO:Mn thin film with applied magnetic field of 10 T, 6 T, and 2 T. The vertical distance between the two thin lines in every circle symbol represents the error bar for that data point. The magnetic field is perpendicular to the film plane for these measurements.

At low temperatures down to 5 K, the MR is large and positive. Initially in weak

fields, it quickly increases, and for temperatures from 5 K to 10 K, the MR exceeds 15%. Eventually it decreases slightly at higher fields. The MR at 5 K with a field of 3.2 T, is 16.6%. As the temperature is increased, the magnitude of the positive MR decreases. A small negative MR component shows up at 50 K, though the MR turns positive at higher fields. For temperatures above this, the MR is small (several percent) and negative over the whole field range. The observed maximum negative MR is -0.63% at 75 K with a field of 10 T. The magnitude of the MR decreases to zero as the temperature further increases until it is insignificant at 300 K. These data indicate a competition between positive and negative contributions to the MR. The positive MR contribution is attributed to the destructive effects on transport of a *sp*-*d* exchange enhanced *s*-electron splitting in the weakly localized regime,[29-31] which is an indication of the intrinsic ferromagnetism in diluted magnetic semiconductors. We also found that the positive MR in the ZnO:Mn thin film is much stronger than in the ZnO:Co thin films we prepared with the same conditions.[32] This could be an indication that the *sp*-*d* exchange coupling in ZnO:Mn is stronger than in ZnO:Co thin films. The negative MR could be from either weak localization, where the magnetic field suppresses quantum constructive interference effect,[33-34] which was also observed in non-magnetic ZnO thin films,[35] or the field suppression of magnetization fluctuations, leading to the delocalization of bound magnetic polarons.[36]

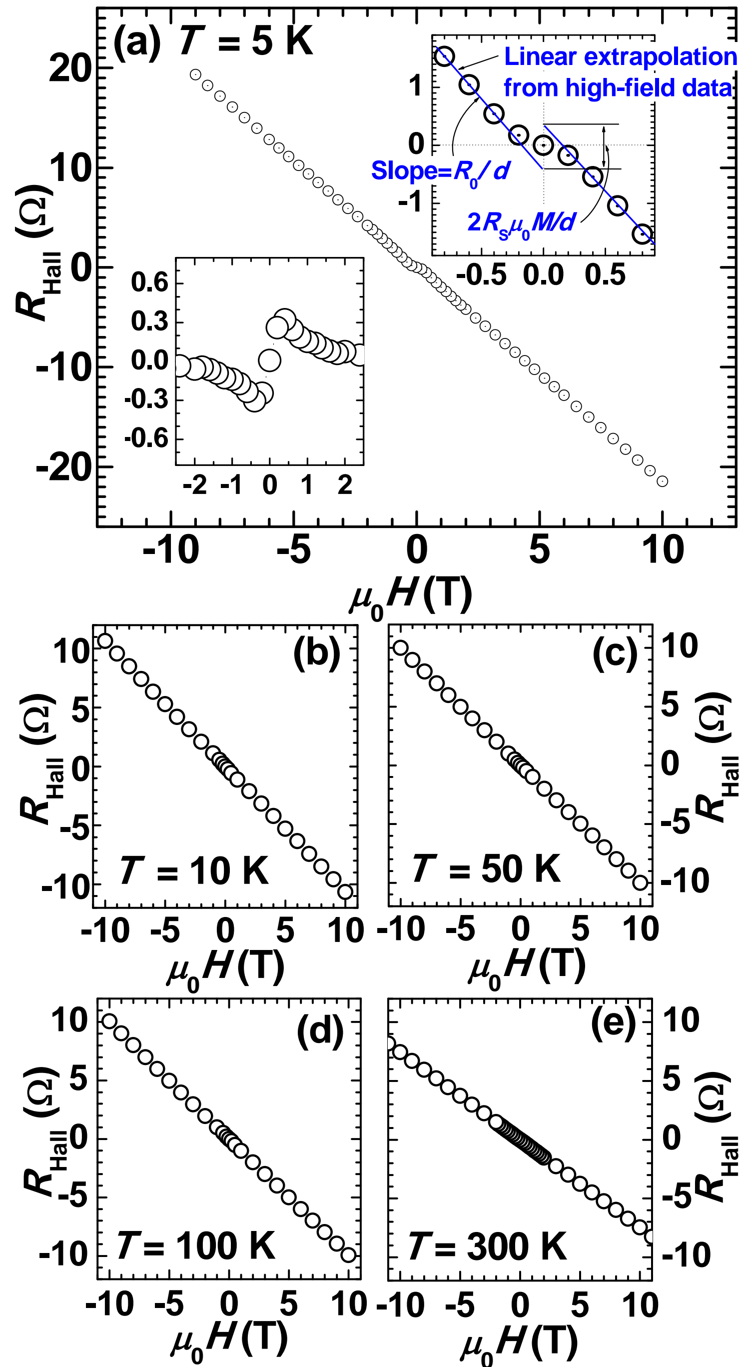


FIG. 6.12. (a) The field dependence of the Hall resistance $R_{Hall}$ measured at 5K. The lower inset shows the AHE after subtracting the linear background from the OHE. The upper inset shows the method employed to determine $R_0$ an $R_S$. (b)-(e) The field-dependence of the Hall resistance measured at 10 K, 50 K, 100 K, and 300 K on the same ZnO:Mn thin film sample.

Figure 6.12(a) shows the field-dependent Hall resistance for the ZnO:Mn thin film, measured at a temperature of 5 K. The vertical axis of the Hall resistance $R_{\mathrm{Hall}}$ is defined as the Hall voltage $V_{\mathrm{H}}$ divided by longitudinal current $I_{\mathrm{x}}$, i.e. $R_{\mathrm{Hall}} = V_{\mathrm{H}} / I_{\mathrm{x}}$. Figures 6.12(b)-(e) show the field-dependent Hall effect measurements performed at 10, 50, 100, and 300 K on the same piece of ZnO:Mn thin film sample.

In magnetic materials, the Hall resistance has two contributions: the ordinary Hall effect (OHE) arising from the classical Lorenz force, and the anomalous Hall effect (AHE) due to the asymmetric scattering from the spin-orbit interaction in the presence of a magnetization. So, $R_{\mathrm{Hall}}$ is expressed with the following equation,

$$R_{\mathrm{Hall}} = \frac{R_0}{d}(\mu_0 H) + \frac{R_s}{d}(\mu_0 M) \equiv R_{\mathrm{OHE}} + R_{\mathrm{AHE}} \qquad (7\text{-}1)$$

where $R_0$ and $R_{\mathrm{OHE}}$ are the ordinary Hall coefficient and resistance, $R_{\mathrm{S}}$ and $R_{\mathrm{AHE}}$ are the anomalous Hall coefficient and resistance, $d$ is the thickness of the ZnO:Mn thin film, which is = 470 nm $H$ and $M$ are the magnetic field and the magnetization perpendicular to the film plane, respectively, and $\mu_0$ is the free space permeability. In Fig. 6.12(a), the linear background with a negative slope is from the OHE. The sign and magnitude of the OHE give information on the carrier type and concentration, respectively. The non-linear component $R_{\mathrm{Hall}}$ is from the AHE. The lower inset shows the $R_{\mathrm{AHE}}$-$\mu_0 H$ spectra after subtracting the linear background (i.e. $R_{\mathrm{Hall}}$-$R_{\mathrm{OHE}}$), where the AHE is clearly visible. The upper inset shows the method employed to determine $R_{\mathrm{S}}$. A linear fitting was performed

on the high-field data (> 5 T and < -5 T), where the magnetization is completely saturated. From the slope of the linear fitting $R_0/d$ was found. The distance along the vertical axis between the two intercepts from the extrapolations of the positive and negative high-field fitting is $2R_S\mu_0M/d$.

Table 6.2 Ordinary Hall coefficient $R_0$, anomalous Hall coefficient $R_S$, electron carrier concentration $n$, and resistivity $\rho_x$ at different temperatures.

| $T$ (K) | $R_0$ ($10^{-9}$ Ω cm $G^{-1}$) | $n$ ($10^{19}$ $cm^{-3}$) | $R_S$ ($10^{-7}$ Ω cm $G^{-1}$) | $\rho_x$ ($10^{-2}$ Ω cm) |
|---|---|---|---|---|
| 5 | -10.14 ± 0.02 | 0.616 ± 0.001 | 3.4 ± 0.5 | 3.76 |
| 10 | -5.04 ± 0.01 | 1.24 | 2.8 ± 0.2 | 3.65 |
| 50 | -4.73 ± 0.01 | 1.32 | 1.9 ± 0.2 | 3.50 |
| 100 | -4.65 ± 0.01 | 1.34 | 1.4 ± 0.2 | 3.33 |
| 300 | -3.48 ± 0.05 | 1.80 ± 0.02 | 0.3 ± 0.3 | 2.91 |

Following the procedure discussed above, $R_0$ and $R_S$ at different temperatures are listed in Table 6.2. The error bars of $R_S$ are larger than those for $R_0$ because of the extrapolation of high-field data to zero field axis. Figure 6.13(a) shows the temperature dependence of $R_0$. The electron carrier concentration $n$, which is shown in the inset as

function of temperature, for the ZnO:Mn thin film was determined from $R_0$ using the relation $R_0$= -1/$ne$ , where $e$ is the charge of the electron. The vertical distance between the two thin lines in every circle ($R_0$) and pentagon ($n$) symbols represents the error bar of $R_0$ and $n$ at each temperature point. (The uncertainty is as small as can be comparable to the size of the symbols.) The electron carrier concentration of this ZnO:Mn thin film only changes by a factor of three in going from 300 K to 5 K, indicating a degenerate semiconductor, which is commonly observed in heavily doped $n$-type thin films.[24] The values of $n$ at different temperatures are also summarized in Table 6.1. Figure 6.13(b) shows the temperature dependence of $R_S$, which decreases with increasing temperature. The observation of an AHE in this ZnO:Mn thin film also provides evidence of instrinsic carrier-mediation ferromagnetism,[37] although the AHE observed here is very weak compared to other ferromagnetic semiconductors, such as GaAs:Mn[21] and InAs:Mn.[22] A very small AHE in ZnO-based DMS materials was also reported by others.[30, 37-40] The reason is not very clear so far. One of the possible reasons might be the relatively large $R_0$ in general ZnO thin films due to smaller carrier concentration comparing to the GaAs:Mn/InAs:Mn or ferromagnetic metals.

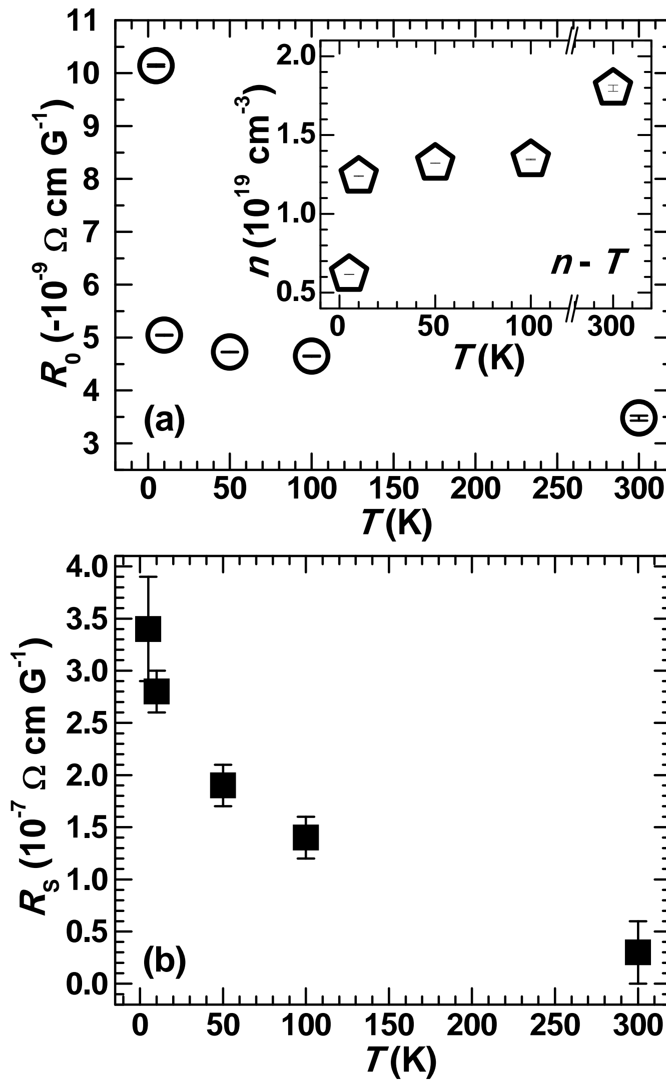


FIG. 6.13. (a) The temperature dependence of ordinary Hall coefficient $R_0$. The inset shows the temperature dependence of the electron carrier concentration $n$ derived from $R_0$. The vertical distance between the two thin lines in every symbols represents the error bar of the data point. (b) The temperature dependence of anomalous Hall coefficient $R_S$.

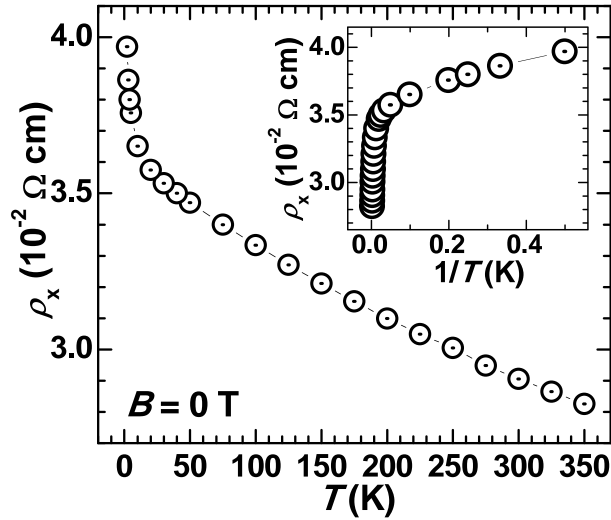


FIG. 6.14 The temperature dependence of the resistivity $\rho_x$ from 2 K to 350 K. The inset shows the same data with reciprocal temperature along the horizontal axis.

Figure 6.14 shows the temperature dependence of the resistivity $\rho_x$ of the ZnO:Mn thin film from 2 K to 350 K. The inset shows the same data, plotted as a function of reciprocal temperature. The resistivity does not show a strong temperature dependence because of the degenerate carrier statistics of this semiconducting ZnO:Mn thin film. This is consistent with the previous discussion on the temperature dependence of $n$. The values of $\rho_x$ at 5, 10, 50, 100, and 300 K are also summarized in Table 6.2.

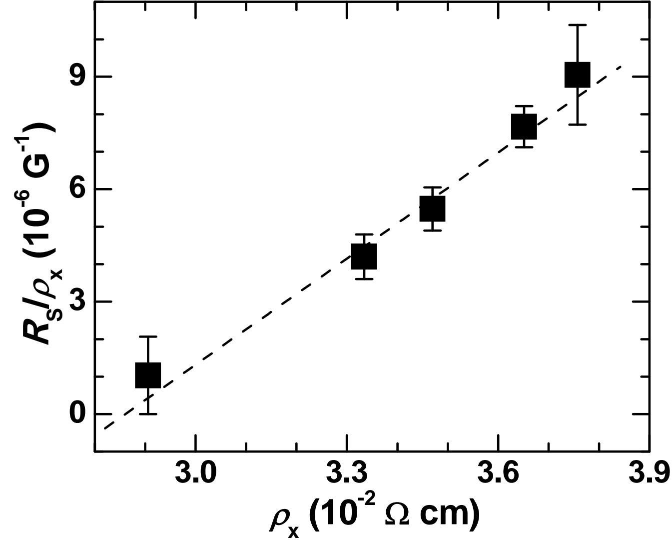


FIG. 6.15. The relation between $R_s/\rho_x$ and $\rho_x$. The solid square symbols with error bars are the experimental data. The dashed line shows a linear fit to the data, representing the linear and quadratic dependences of $\rho_x$ on $R_s$.

The origin of the AHE is attributed to spin-orbit coupling, and $R_S$ depends on $\rho_x$ as $R_S = a_{sk}\rho_x + b_{sj}\rho_x^2$.[41-43] The linear term is physically interpreted as the skew scattering where the angle $\phi_{sk} = a_{sk} \cdot \mu_0 M$ represents the average deflection of a charge carrier at a scattering center. The quadratic term is associated with a side-jump mechanism where the charge carrier's trajectory is displaced a fixed distance perpendicular to its original path at each scattering center. Figure 6.15 shows the relation between $R_S/\rho_x$ and $\rho_x$. The solid square symbols with error bar are the experimental data and the dashed line shows the fit. $\phi_{sk}$ is estimated to be ~-0.4 millirad and $b_{sj}$ is

approximately 9.4 × $10^{-4}$ $\Omega^{-1}$ $cm^{-1}$ $G^{-1}$ . The negative value of $\phi_{sk}$ is widely observed in ferromagnetic transition metals.[44]

## 6.4 Summary

In summary, ferromagnetism with a transition temperature well-above room temperature, electron-concentration dependent magnetization, and magnetic anisotropy was observed in *n*-type ZnO:Mn thin films, indicating long-range ferromagnetic order. The ferromagnetism persisted to temperatures well-above room temperature. The magnetic anisotropy was also observed in these ZnO:Mn films is another indication for intrinsic ferromagnetism. The dependence of the magnetization on electron concentration provides strong experimental evidence for an electron-mediated exchange mechanism for ferromagnetism in ZnO:Mn materials, contrary to the requirement of a hole-rich environment predicted by theory. Microstructural studies using transmission electron microscopy (TEM) were performed on a ZnO:Mn diluted magnetic semiconductor (DMS) thin film. The high-resolution imaging and electron diffraction reveal that the ZnO:Mn thin film has a high structural quality and is free of clustering/segregated phases. High-angle annular dark field Z-contrast imaging and XRD further corroborate the absence of phase segregation in the film, leading us to believe that the ferromagnetism in this material is intrinsic. Magnetotransport was studied on the ZnO:Mn samples, and

from these measurements, the temperature dependence of the resistivity and magnetoresistance, electron carrier concentration, and anomalous Hall coefficient of the sample is discussed. A large positive magnetoresistance is observed, indicating a strong *sp*-*d* exchange in ZnO:Mn DMS thin films. Both the ordinary and anomalous Hall coefficients were determined from the field dependence of Hall resistance. The anomalous Hall coefficient has a strong quadratic dependence on the resistivity, which implies a side-jump scattering mechanism in the AHE, further supporting an origin of the intrinsic spin-obital ferromagnetism in ZnO:Mn DMS thin films.

### 6.5 Acknowledgement

Most of the results in this chapter were published on *Applied Physics Letters* 92, 042111 (2008) and on *Journal of Applied Physics* 105, 053708 (2009). This work was supported by DOD/DMEA through the Center of Nanomateials and Nanodevices (CNN) under the award No. H94003-06-20604. The electron microscopy studies at the Electron Microbeam Analysis Laboratory at the University of Michigan were supported by the National Science Foundation under grant No. DMR-0315633 and DMR-9871177.

**References**

[1] S. J. Pearton, W. H. Heo, M. Ivill, D. P. Norton, and T. Steiner, Semicond. Sci. and Technol. **19**, R59 (2004).

[2] C. Liu, F. Yun, and H. Morkoç, J. of Mater. Sci: Mater. Electron. **16**, 555 (2005).

[3] T. Fukumura, Z. Jin, A. Ohtomo, H. Koinuma, and M. Kawasaki, Appl. Phys. Lett. **75**, 3366 (1999).

[4] T. Fukumura, Z. Jin, M. Kawasaki, T. Shono, T. Hasegawa, S. Koshihara, and H. Koinuma, Appl. Phys. Lett. **78**, 958 (2001).

[5] K. Ando, H. Saito, Z. Jin, T. Fukumura, M. Kawasaki, Y. Matsumoto, and H. Koinuma, Appl. Phys. Lett. **78**, 2700 (2001).

[6] K. Udea, H. Tabata, and T. Kawai, Appl. Phys. Lett. **79**, 988 (2001).

[7] Z. Jin, T. Fukumura, M. Kawasaki, K. Ando, H. Saito, T. Sekiguchi, Y. Z. Yoo, M. Murakami, Y. Matsumoto, T. Hasegawa, and H. Koinuma, Appl. Phys. Lett. **78**, 3824 (2001).

[8] H. J. Lee, S. Y. Jeong, C. R. Cho, and C. H. Park, Appl. Phys. Lett. **81**, 4020 (2002).

[9] D. P. Norton, M. E. Overberg. S. J. Pearton, K. Pruessner, J. D. Budai, L. A. Boatner, M. F. Chisholm, J. S. Lee, Z. G. Khim, Y. D. Park, and R. G. Wilson, Appl. Phys. Lett. **83**, 5488 (2003).

[10] P. Sharma, A. Gupta, K. V. Rao, Frank J. Owens, R. Sharma, R. Ahuja, J. M. Osorio

Guillen, B. Johansson, and G. A. Gehring, Nat. Mater. **2**, 673 (2003).

[11] D. A. Schwartz and D. R. Gamelin, Adv. Mater. **16**, 2115 (2004).

[12] M. Venkatesan, C. B. Fitzgerald, J. G. Lunnery, and J. M. D. Coey, Phys. Rev. Lett. **93**, 177206 (2004).

[13] J. M. D. Coey, M. Venkatesan, and C. B. Fitzgerald, Nat. Mater. **4**, 173 (2005).

[14] M. H. F. Sluiter, Y. Kawazoe, P. Sharma, A. Inoue, A. R. Raju, C. Rout, and U. V. Waghmare, Phys. Rev. Lett. **94**, 187204 (2005).

[15] K. R. Kittilstved, N. S. Norberg, and D. R. Gamelin, Phys. Rev. Lett. **94**, 147209 (2005).

[16] K. R. Kittilstved, D. A. Schwartz, A. C. Tuan, S. M. Heald, S. A. Chambers, and D. R. Gamelin, Phys. Rev. Lett. **97**, 037203 (2006).

[17] C. Song, K. W. Geng, F. Zeng, X. B. Wang, Y. X. Sheng, F. Pan, Y. N. Xie, T. Liu, T. T. Zhou, and Z. Fan, Phys. Rev. B **73**, 024405 (2006).

[18] H. Pan, J. B. Yi, L. Shen, R. Q. Wu, J. H. Yang, J. Y. Lin, Y. P. Feng, J. Ding, L. H. Van, and J. H. Yin, Phys. Rev. Lett. **99**, 127201 (2007).

[19] Z. Yang, J. L. Liu, M. Biasini, and W. P. Beyermann, Appl. Phys. Lett. **92**, 042111 (2008).

[20] T. Dietl, H. Ohno, F. Matsukura, J. Cibert, and D. Ferrand, Science **287**, 1019 (2000); T. Dietl, H. Ohno, and F. Matsukura, Phys. Rev. B **63**, 195205 (2001).

[21] H. Ohno, Science 281, 951 (1998).

[22] H. Ohno, D. Chiba, F. Matsukura, T. Omiya, E. Abe, T. Dietl, Y. Ohno, and K. Ohtani, Nature **408**, 944 (2000).

[23] K. Sato and H. Katayama-Yoshida, Semicond. Sci. and Technol. **17**, 367 (2002).

[24] Z. Yang, D. C. Look, J. L. Liu, Appl. Phys. Lett. **94**, 072101 (2009).

[25] M. Shiojiri and H. Saijo, J. Microscopy **223**, 172 (2006).

[26] S. Utsunomiya and R. C. Ewing, Environ. Sci. Tecnol. **37**, 786 (2003).

[27] T. Dietl, T. Andrearczyk, A. Lipińska, M. Kiecana, M. Tay, and Y. Wu, Phys. Rev. B **76**, 155312 (2007).

[28] S. Kuroda, N. Nishizawa, K. Takita, M. Mitome, Y. Bando, K. Osuch, and T. Dietl, Nature Mater. **6**, 440 (2007).

[29] J. Wang, Z. Gu, M. Lu, D. Wu, C. Yuan, S. Zhang, Y. Chen, S. Zhu, and Y. Zhu, Appl. Phys. Lett. **88**, 252110 (2006).

[30] Q. Xu, L. Hartmann, H. Schmidt, H. Hochmuth, M. Lorenz, R. Schmidt-Grund, d. Spemann, and M. Grundmann, J. Appl. Phys. **100**, 013904 (2006).

[31] M. Sawicki, T. Dietl, J. Kossut, J. Igalson, T. Wojtowicz, and W. Plesiewicz, Phys. Rev. Lett. **56**, 508 (1986).

[32] Z. Yang, M. Biasini, W. P. Beyermann, M. B. Katz, O. K. Ezekoye, X. Q. Pan, Y. Pu, J. Shi, Z. Zuo, and J. L. Liu, J. Appl. Phys. **104**, 113712 (2008).

[33] P. A. Lee and V. Vramakrishnan, Rev. Mod. Phys. **57**, 287 (1985).

[34] S. Hikami, A. I. Larkin, and Y. Nagaoka, Prog. Theor. Phys. **63**, 707 (1980).

[35] A. Goldenblum, V. Bogatu, T. Stoica, Y. Goldstein, and A. Many, Phys. Rev. B **60**, 5832 (1999).

[36] H. Ohno, H. Munekata, T. Penney, S. von. Molnar, and L. L. Chang, Phys. Rev. Lett. **68**, 2664 (1992).

[37] Y. Z. Peng, T. Liew, T. C. Chong, C. W. An, and W. D. Song, Appl. Phys. Lett. **88**, 192110 (2006).

[38] Q. Xu, L. Hartmann, H. Schmidt, H. Hochmuth, M. Lorenz, R. Schmidt-Grund, C. Sturm, D. Spemann, and M. Grundmann, Phys. Rev. B **73**, 205342 (2006).

[39] Q. Xu, L. Hartmann, H. Schmidt, H. Hochmuth, M. Lorenz, R. Schmidt-Grund, C. Sturm, D. Spemann, M. Grundmann, and Y. Liu, J. Appl. Phys. **101**, 063918 (2007).

[40] S. J. Pearton, D. P. Norton, M. P. Ivill, A. F. Hebard, J. M. Zavada, W. M. Chen, and I. A. Buyanova, IEEE Trans. Elect. Device **54**, 1040 (2007).

[41] R. C. O'Handley, *Modern Magnetic Materials: Principles and Applications* (John Wiley & Sons, Inc, 2000), p570-573.

[42] C. M. Hurd, *The Hall Effect in Metals and Alloys* (Plenum, New York, 1972), Ch. 5.

[43] C. L. Chien and C. W. Westgate, *The Hall Effect and Its Applications* (Plenum, New York, 1980).

[44] E. P. Wohlfarth, *Ferromagnetic Materials* Vol. 3, Ch. 9, Transport Properties of Ferromagnets (by I. A. Campbell and A. Fert).

# 7. Chapter 7 Conclusions

(1) ZnO materials have potential applications in optoelectronics, such as light emitting diodes and laser diodes, due to its large exciton binding energy (~60 meV). ZnO materials have potential spintronics, because it is both theoretically predicted and experimental proved that ZnO-based diluted magnetic semiconductors can be ferromagnetic above room temperature.

(2) ZnO thin films were grown on *r*-plane sapphire substrates using ECR plasma-assisted MBE. ECR plasma power plays an important role to the growth rate and crystallinity of ZnO thin films. The effect of the oxygen ECR plasma power on the growth rate, structural, electrical, and optical properties of the ZnO thin films were studied. The growth rate increases with the increase of plasma power because of the increased atomic oxygen density. The enhanced plasma power improves ZnO film crystallinity, decreases the density of Zn interstitial defect formation, and improves optical properties due to smaller density of non-radiative luminescence centers because of decreased ionic oxygen density.

(3) We have carried out photoluminescence (PL) and Hall-effect measurements for a series of Ga-doped ZnO thin films grown by molecular-beam epitaxy. For high Ga

doping, the PL spectra are dominated by the neutral-Ga donor-bound exciton $I_8$ at 3.359 eV, and for low Ga doping, the ionized-Ga donor bound exciton $I_1$ at 3.371 eV. The low-Ga spectra in this study demonstrate one of the first ever observations of higher $I_1$ intensity than that of $I_8$, and this phenomenon is explained by the T-Hall result that $[Ga^+] >> [Ga^0]$ in these low-Ga samples. For intermediate Ga doping, a line that ranges from 3.31 – 3.32 eV, designated as $I_{DA}$, is dominant. We have shown that $I_{DA}$ has characteristics of a donor-acceptor-pair transition, and have used a detailed, quantitative analysis to argue that it arises from $Ga_{Zn}$ donors paired with Zn-vacancy ($V_{Zn}$) acceptors. The success of our analysis depends upon, and lends credence to, a recent theoretical calculation of the $V_{Zn}^{0/-}$ acceptor transition energy. The excitation power-dependent and temperature-dependent PL results support the DAP assignment well. A Haynes factor of 0.3 is derived based on low-temperature and temperature-dependent PL studies on heavily Ga-doped ZnO samples.

(4) Structural, optical properties, and doping mechanism of Sb doped *p*-type ZnO on Si (100) and Si (111) were comprehensively studied. Crystallinity and strain in both *c* and *a* plane were studied by XRD $\theta$-$2\theta$ scan and in-plane GI XRD. XPS measurements show that Sb dopants were incorporated into the *p*-type ZnO films with a positive charge, implying that Sb substitutes for Zn and bonds with O.

Various-temperature PL measurements reveal that heavy Sb doping can trigger the formation of Zn vacancies, raising a broad emission around ~3.0 eV. Combing with the theoretical calculation, which suggest that the $Sb_{Zn}$-$2V_{Zn}$ is a shallow acceptor and with low formation energy under oxygen rich condition, although $Sb_{Zn}$ itself is a donor in ZnO, the formation of a $Sb_{Zn}$ and $V_{Zn}$ complex is believed to be the origin of shallow acceptors in this system. It is found that the possibility of achieving *p*-type ZnO:Sb is also closely related to the thin film morphology. ZnO:Sb grown on Si substrates with closely-packed nano-columnar structures facilitates the achievement of reliable *p*-type doing, because $V_{Zn}$-related acceptor complex is more easily forming interfacially at grain boundaries in ZnO and the morphology with large grain boundary surface areas, such as the side walls of the nano-columns, facilitates the *p*-type doping in ZnO samples.

(5) Diluted magnetic semiconducting ZnO:Co thin films with above room-temperature $T_C$ were prepared. The structural, magnetic, and electrical transport properties of ZnO:Co thin films were comprehensively characterized. No secondary phases were observed by TEM and XRD. Ferromagnetism was observed in ZnO:Co thin films with a Curie temperature far above room-temperature. The saturated magnetization of the ZnO:Co thin films increases dramatically when the free electron carrier

concentration exceeds ~$10^{19}$ $cm^{-3}$, indicating a carrier-mediated mechanism for ferromagnetism. The ZnO:Co thin films show magnetic anisotropy with the easy magnetization axis parallel to the film plane. A strong temperature dependence and competition between positive and negative contributions were observed in magnetoresistance of the ZnO:Co thin films. Finally, an anomalous Hall effect was observed and analyzed in the ZnO:Co thin films, consistent with long-range ferromagnetism. The anomalous Hall coefficient and its dependence on longitudinal resistivity were analyzed. The presence of a side-jump contribution further supports an intrinsic origin for ferromagnetism in ZnO:Co thin films. These observations together with the magnetic anisotropy and magnetoresistance results, lend supports to an intrinsic carrier-mediated mechanism for the ferromagnetic exchange in ZnO:Co DMS materials.

(6) Ferromagnetism with a transition temperature well-above room temperature, electron-concentration dependent magnetization, and magnetic anisotropy was observed in *n*-type ZnO:Mn thin films, indicating long-range ferromagnetic order. The ferromagnetism persisted to temperatures well-above room temperature. The magnetic anisotropy was also observed in these ZnO:Mn films is another indication for intrinsic ferromagnetism. The dependence of the magnetization on electron

concentration provides strong experimental evidence for an electron-mediated exchange mechanism for ferromagnetism in ZnO:Mn materials, contrary to the requirement of a hole-rich environment predicted by theory. Microstructural studies using transmission electron microscopy (TEM) were performed on a ZnO:Mn diluted magnetic semiconductor (DMS) thin film. The high-resolution imaging and electron diffraction reveal that the ZnO:Mn thin film has a high structural quality and is free of clustering/segregated phases. High-angle annular dark field Z-contrast imaging and XRD further corroborate the absence of phase segregation in the film, leading us to believe that the ferromagnetism in this material is intrinsic. Magnetotransport was studied on the ZnO:Mn samples, and from these measurements, the temperature dependence of the resistivity and magnetoresistance, electron carrier concentration, and anomalous Hall coefficient of the sample is discussed. A large positive magnetoresistance is observed, indicating a strong *sp-d* exchange in ZnO:Mn DMS thin films. Both the ordinary and anomalous Hall coefficients were determined from the field dependence of Hall resistance. The anomalous Hall coefficient has a strong quadratic dependence on the resistivity, which implies a side-jump scattering mechanism in the AHE, further supporting an origin of the intrinsic spin-obital ferromagnetism in ZnO:Mn DMS thin films.